AMMRC TR 78-11

DEVELOPMENT OF NONDESTRUCTIVE TESTING TECHNIQUES FOR HIGH PERFORMANCE CERAMICS

JANUARY 1978

H. R. BAUMGARTNER
NORTON COMPANY
WORCESTER, MA

R. H. BROCKELMAN
AMMRC
WATERTOWN, MA

P. M. HANSON
NORTON COMPANY
WORCESTER, MA

FINAL REPORT - CONTRACT DAAG46-76-C-0022

Approved for public release; distribution unlimited

OFFICIAL FILE COPY

Prepared for

ARMY MATERIALS AND MECHANICS RESEARCH CENTER
Watertown, Massachusetts 02172

The findings in this report are not to be construed as an official Department of the Army position, unless so designated by other authorized documents.

Mention of any trade names or manufacturers in this report shall not be construed as advertising nor as an official indorsement or approval of such products or companies by the United States Government.

DISPOSITION INSTRUCTIONS

Destroy this report when it is no longer needed.
Do not return it to the originator.

UNCLASSIFIED

SECURITY CLASSIFICATION OF THIS PAGE *(When Data Entered)*

REPORT DOCUMENTATION PAGE

READ INSTRUCTIONS BEFORE COMPLETING FORM

1. REPORT NUMBER: AMMRC TR 78-11	2. GOVT ACCESSION NO.
3. RECIPIENT'S CATALOG NUMBER	
4. TITLE *(and Subtitle)*: DEVELOPMENT OF NONDESTRUCTIVE TESTING TECHNIQUES FOR HIGH PERFORMANCE CERAMICS	5. TYPE OF REPORT & PERIOD COVERED: Final Report
	6. PERFORMING ORG. REPORT NUMBER
7. AUTHOR(s): H. R. Baumgartner, R. H. Brockelman, P. M. Hanson	8. CONTRACT OR GRANT NUMBER(s): DAAG46-76-C-0022
9. PERFORMING ORGANIZATION NAME AND ADDRESS	10. PROGRAM ELEMENT, PROJECT, TASK AREA & WORK UNIT NUMBERS: D/A Project: M756350; AMCMS Code: 53970M6350; Agency Accession:
11. CONTROLLING OFFICE NAME AND ADDRESS: Army Materials and Mechanics Research Center, Watertown, Massachusetts 02172	12. REPORT DATE: January 1978
	13. NUMBER OF PAGES: 98
14. MONITORING AGENCY NAME & ADDRESS*(if different from Controlling Office)*	15. SECURITY CLASS. *(of this report)*: Unclassified
	15a. DECLASSIFICATION/DOWNGRADING SCHEDULE: -

16. DISTRIBUTION STATEMENT *(of this Report)*

Approved for public release; distribution unlimited.

17. DISTRIBUTION STATEMENT *(of the abstract entered in Block 20, if different from Report)*

18. SUPPLEMENTARY NOTES

This project has been accomplished as part of the U.S. Army Materials Testing Technology Program, which has for its objective the timely establishment of testing techniques, procedures or prototype equipment (in mechanical, chemical, or nondestructive testing) to insure efficient inspection methods for materiel/material procured or maintained by DARCOM.

19. KEY WORDS *(Continue on reverse side if necessary and identify by block number)*

Silicon nitride
Silicon carbide
Nondestructive testing
Mechanical strength
Inclusions
Ceramics

20. ABSTRACT *(Continue on reverse side if necessary and identify by block number)*

Two ceramic materials, a hot-pressed silicon nitride and a siliconized silicon carbide, were manufactured with seeded particulates to evaluate the effectiveness of existing nondestructive test practices for defect detection in ceramics and to evaluate the effect of inclusions upon material strength. The types of seeded defects were of greater and lower density relative to the matrix materials and ranged in size from approximately 0.1 mm to

DD FORM 1 JAN 73 1473 EDITION OF 1 NOV 65 IS OBSOLETE

UNCLASSIFIED

SECURITY CLASSIFICATION OF THIS PAGE *(When Data Entered)*

Block No. 20

ABSTRACT

0.6 mm. The nondestructive methods used in the investigation were ultrasonics, radiography, eddy current and penetrant. Bend bar specimens were cut from the seeded regions of the billets and tested at 25°C, 1093°C and 1371°C. Fracture origins were examined by optical and electron microscopy and by microprobe to correlate the nature of the fracture initiating defects with the nondestructively detected defects. This permitted a ranking of defect detection sensitivity and defect effect upon strength.

SUMMARY

Particulate defects were incorporated into NC-132 silicon nitride and NC-435 silicon carbide billets to produce materials containing characterized inclusions for subsequent nondestructive examination. Particles of tungsten carbide, iron, silicon and graphite, in three nominal sizes of 0.13, 0.25 and 0.64 mm (0.005, 0.010 and 0.25 inch), were introduced into the hot-pressed silicon nitride (HPSN) billets according to a rectangular placement plan. Similarly, iron, silicon and graphite particles were seeded into the silicon carbide (SiC) billets. With the exception of the defect seeding procedures, standard production material mixes and processing procedures were used to manufacture two 15 x x 15 cm billets of each material. Billet thicknesses were 8.2 and 5.7 mm for the silicon carbide and silicon nitride billets, respectively.

The billets were examined by existing nondestructive evaluation (NDE) methods to evaluate the effectiveness of the methods in measuring billet inclusion content and general overall billet quality. The billets were examined by radiographic, eddy current, penetrant, and a variety of ultrasonic inspection techniques. A pulse-echo ultrasonic method and radiography were used to detect inclusions in the materials. While examining the newer, and therefore less characterized, SiC material, broad area ultrasonic reflections, which hampered inclusion detection, were discovered unexpectedly. These areas were studied further by ultrasonic attenuation measurements and eddy current variations. The reflections were later traced to planar microstructural phase inhomogeneities in the SiC material.

Sonic velocity measurements, potentially useful in detecting material density variations, were used to establish average longitudinal wave velocities of 1.12 cm/micro sec and 1.21 cm/micro sec in the HPSN and SiC materials, respectively. The variation between velocity measurements were less than 1 percent and 3 percent, respectively, for the two materials, which indicates the absence of large volume density variations in the billets. Fluorescent penetrants revealed the presence of several laminations and cracks along the edges of the SiC billets.

With regard to inclusions, broadband high resolution ultrasonic test equipment was used to detect discontinuities by pulse-echo examination. A 25 MHz frequency was used and defects were depicted by immersion C-scan techniques. The use of machined surfaces was necessary to separate defect indications from surface roughness signals in the as-pressed billet condition. The coarse and medium size contaminants were readily visible in the scans of the HPSN billets. The fine size seeded defects were not detected as readily except for iron particles in one and silicon

particles in the other HPSN billet. Although ultrasonic indications were recorded in areas where the fine particles should have been, they did not conform to the seeding plan in position or number. The disparity between seeding plan and defect indication was due in large part to the detection of many defects which were not intentionally seeded but which were incorporated into the billets as a result of the seeding operation procedures. As mentioned, large areas of unexpected reflections masked the flaw detection capabilities of the pulse-echo method for much of the SiC billets. Some seeded defects were evident in regions clear of these reflections.

Standard radiographic techniques, with a tube voltage of 60 KVP, were used to inspect the billets for contaminants. All sizes of the tungsten carbide and iron contaminants in the HPSN billets were radiographically visible. The fine and medium size silicon and graphite particles were not visible in the HPSN billets, even with a machined surface. In addition to the ordered seeded particles, approximately 30 high density particles about 0.13 mm in size were found in a dispersed cloud in one HPSN billet.

Following the characterization of the billet plates, the seeded regions of the billet were rough cut into rectangular blanks of sizes of 7.4 x 11.1 x 32 mm and 5.5 x 7.9 x 32 mm for the carbide and nitride materials, respectively. The individual blanks were examined by ultrasonic C-scans and radiography to locate closely the three-dimensional coordinates of the indicated contaminants. One of the contaminants within a given blank was selected as a "target" defect and the thickness of the bar was additionally machined in order to locate the defect close to the surface of the bar. The machined bars were used as bend test specimens to evaluate the effect of inclusions upon material strength.

Over 70 HPSN bars and 23 SiC bars from seeded regions of the billets were broken in four-point bending at room temperature in order to study the effect of inclusions on material strength. Optical microscopy was used to identify the nature of the fracture origin as an inclusion particle or a surface microcrack and to measure the cross-sectional orthogonal dimensions of fracture initiating inclusions. With very few exceptions, the fractures were initiated by inclusions. The smallest inclusions observed to initiate failure were approximately 25 x 25 microns (0.001 x 0.001 inch) in cross-section and it was apparent that unintentional defects were competing with seeded defects as fracture origins. By comparing the location of a fracture exposed inclusion with the defect locations indicated by NDE methods, it was possible to ascertain whether a fracture initiating defect had been detected by nondestructive means.

A limited program of bend testing was conducted at 1093°C and 1370°C on seeded and unseeded specimens of the HPSN and SiC materials. The effect of temperature upon material strength is summarized in Table S1. (The room temperature strengths from the unseeded portions of the NC-132 HPSN billets are somewhat below normal for this material. The mean strength of 380 samples taken from the last 40 NC-132 HPSN billets was 834 MN/m^2 with a standard deviation of 129 MN/m^2. The lower strength of the program's billets is attributed to the greater handling of the powder and the concomitant introduction of unintentional defects.) In HPSN at 1093°C, fractures are still largely of a brittle nature and the strength of unseeded specimens are similar to 25°C values. Three of the five seeded HPSN specimens that were broken at this temperature failed at inclusions and the remaining two failed at edge flaws. Material strength of unseeded SiC specimens at 1093°C exceeds that at 25°C due to the increased plasticity of the silicon phase. Three of the five seeded SiC specimens that were broken at this temperature failed at inclusions and the remaining two failed at surface flaws. At 1371°C, the inherent strength of both materials is substantially less because of thermal activation of new failure mechanisms. At the higher temperature, grain boundary sliding in the HPSN causes slow crack growth and in the SiC material the silicon phase approaches melting, which decreases the material's rigidity and modulus. With the onset of these new failure mechanisms, inclusions become less important in initiating fracture. However, instances of inclusion assisted fracture were still observed at 1371°C in each material.

Approximately 40 fracture origins in bend bars were examined by means of scanning electron microscopy (SEM) and an energy dispersive microprobe to clarify the chemical nature of the inclusions. All four types of seeded particles in the HPSN were identified plus carbon and silicon particles in the SiC. This procedure permitted the identification of some seeded defects whose natures were not clear from the NDE inspections because of the large number of defects detected.

Stresses at the fracture initiating inclusions were computed from the depth of the defect within the bend bar, the outer fiber stress and the assumption of a linear bend stress gradient. For each defect type, breaking stress at the defect was plotted as a function of the thickness dimension (in the direction of the applied bend load) of the inclusion. (See Figures 29A, B and C in text.) The fracture stress at a particular type of defect decreases as the defect size increases in the size range studied. An exception to this stress-size relationship was tungsten carbide particles in HPSN, for which the fracture stress was invarient with size.

A comparison of the abilities of the ultrasonic and radiographic methods to detect defects of different types is shown in

TABLE S1

	25°C[1]	1093°C[2]	1371°C[2]
NC-132 HPSN			
Billet T, Unseeded	732;604-894;12	725;684-738;5	339;329-348;5
Billet B, Unseeded	650;517-812;12	678;590-776;5	377;364-388;5
Billet T, Seeded	403*†;117-675;39	593, 660*	311
Billet B, Seeded	460*†;238-639;29	346*,572*,762	319*,343, 354, 359
NC-435 SiC			
Billet #1 Unseeded	388;316-519;8	476;438-494;5	335;325-344;5
Billet #2 Unseeded	305;264-361;8	455;402-518;5	328;301-366;4
Billet #1 Seeded	272*†;134-342;11	312*,332*,372*, 445, 455	-
Billet #2 Seeded	267*†;184-426;5	-	200*,246,272, 301

[1]Four-point bend fixture

[2]Three-point bend fixture

*Inclusion assisted fracture

†Average for all types of inclusions

Influence of Test Temperature on Strength (MN/m^2) of Seeded and Unseeded Ceramic Materials. Mean strength, strength range, and number of tests, respectively, are given for each condition except for seeded high temperature strengths where individual bar strengths are given.

Table S2. The listing was constructed by combining the results of the C-scans and radiographs, from which many defect sizes and types could be determined by inspection, with the results of the SEM and microprobe examination. The three size classification, fine, medium and coarse, relate to the three sizes of seeded defects. However, because of changes in seeded defect geometry during material manufacture, final inclusion dimensions may not be equated with as-seeded dimensions. It is seen that ultrasonics is capable of detecting a wider range of defect sizes than radiography, which is more successful in detecting higher density inclusions than low density ones.

TABLE S2

	Nominal Defect Size		
Matrix Material;Defect Type	Fine	Medium	Coarse
NC-132 HPSN;Fe	X, U	X, U	X, U
" " ;WC	X, U	X, U	X, U
" " ;Si	U	U	X, U
" " ;C	-	U	X, U
NC-435 SiC;C	U	U	X, U
" " ;Si	-	U	U

Relative effectiveness of detection of seeded defect inclusions by ultrasonics and radiography.

X = radiographic detection
U = ultrasonic detection

FOREWORD

This report was prepared by the Industrial Ceramics Division, Norton Company, under Army Materials and Mechanics Research Center (AMMRC) Contract DAAG46-76-C-0022. The development program was a joint effort with the Nondestructive Testing Industrial Applications Branch, Materials Testing Technology Division, of AMMRC and Norton Company. The AMMRC Technical Monitor for the Contract was Mr. C. H. Hastings, to whom appreciation is expressed for his technical assistance and guidance.

The nondestructive evaluation of the ceramic materials was performed at AMMRC under the direction of Mr. C. H. Hastings and with the able assistance of Mr. R. H. Brockelman, and Mr. S. DerBoghosian. Special thanks and appreciation are expressed to Mr. Brockelman for writing the report section covering NDE Procedures.

The Project Manager at Norton was H. R. Baumgartner; billet preparation and seeding was performed by P. M. Hanson and F. J. Kudarauskas provided the very helpful electron microscopy.

TABLE OF CONTENTS

LIST OF FIGURES

LIST OF FIGURES
(continued)

LIST OF FIGURES
(continued)

LIST OF FIGURES
(continued)

LIST OF TABLES

LIST OF TABLES
(continued)

I INTRODUCTION

The use of ceramics as structural components, such as in gas turbine applications, has produced the need to inspect and evaluate the quality of these components. Nondestructive inspection methods have long been used to evaluate the structural soundness of metal components and a large body of technology regarding metal inspection has evolved.

Although it is expected that many of these methods are also applicable to ceramics, the different physical properties of ceramics, such as the generally higher elastic modulii, finer grain size and greater sensitivity to smaller flaws, and different methods of fabrication require that the methods be evaluated for their appropriateness for ceramic materials. In particular, the nondestructive inspection methods must be evaluated with respect to suitability for detecting relevant defect types and defining the size-sensitivity limitations in specific materials. This approach requires a knowledge of the inspection techniques and the defects and materials being evaluated.

In the current program, existing nondestructive test methods at AMMRC, including ultrasonics, radiography, eddy current and penetrant, were evaluated for their effectiveness in inspecting ceramic materials. The two commercial materials, a hot pressed silicon nitride and a siliconized silicon carbide, are manufactured by different fabrication techniques and both are candidates for high temperature structural applications.

II EXPERIMENTAL PROCEDURE

A. SEEDED BILLET PREPARATION

The hot matrix ceramic materials selected for seeding with inclusion defects were NC-132 silicon nitride and NC-435 silicon carbide. The former material is a dense, high strength form of silicon nitride prepared by hot pressing silicon nitride powder. The latter material is a densified silicon carbide of approximately 85 weight percent silicon carbide and 15 weight percent free silicon plus one to two volume percent of porosity. Representative micrographs of the two matrix materials are shown in Figures 1 and 2.

The inclusion defects selected for incorporation into the hot pressed silicon nitride (HPSN) were graphite, iron, silicon and tungsten carbide (WC) particles. The same types of particles, with the exception of the tungsten carbide, were seeded into the silicon carbide billets. This group of seeded materials contains

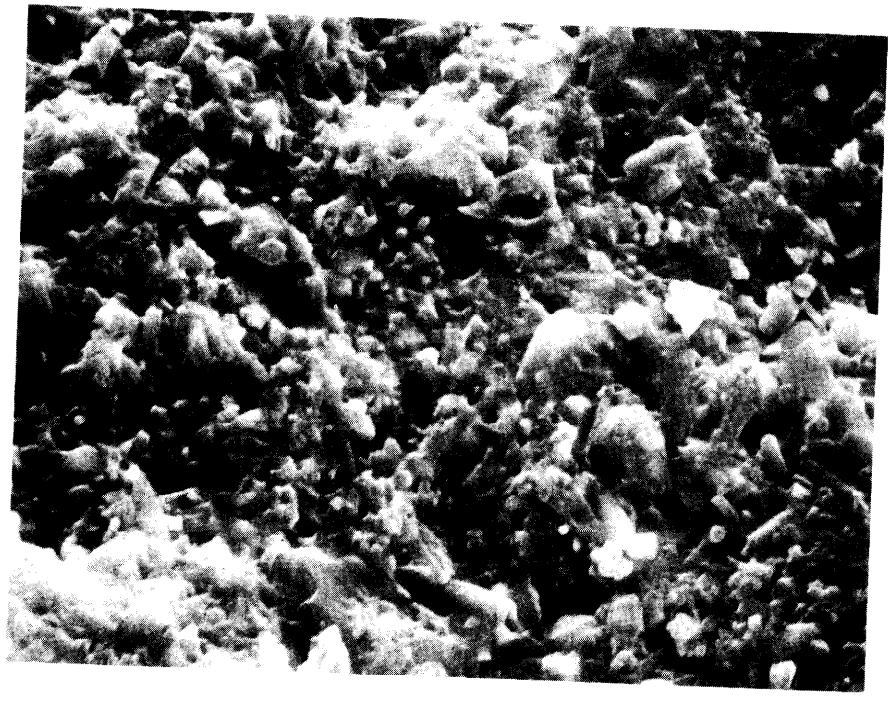

Figure 1. Typical NC-132 HPSN microstructure, SEM,5000X.

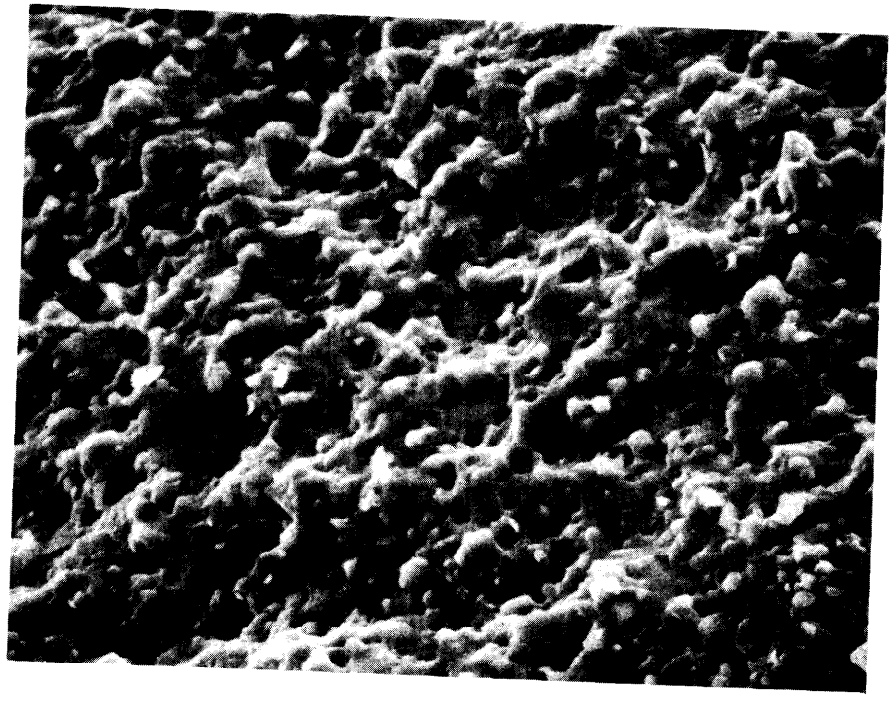

Figure 2. Typical NC-435 microstructure, SEM, 2000X.

members which are higher or lower in physical density than the matrix materials. In addition, particles of similar composition are frequently found in the matrix materials as normal processing defects.

The particles were sized into three nominal size fractions, coarse, medium and fine, by Tyler Screen sieving. The minimum, mean, and maximum particle diameter for each size distribution was determined by optical microscopy and this information is presented in Table 1. The nominal sizes of fine, medium, and coarse correspond to mean particle diameters of approximately 125, 250 and 635 microns, respectively.

TABLE 1. SIZING OF SEEDED PARTICLES
Diameters given in micrometers.

Nominal Size Name	Nominal Particle Diameter	Particle Diameter Ranges					
		WC			Fe		
		Min.	Mean	Max.	Min.	Mean	Max.
Fine	125	51	127	178	51	127	152
Medium	250	127	254	356	254	305	356
Coarse	635	508	660	762	508	635	762
		Si			C		
		Min.	Mean	Max.	Min.	Mean	Max.
Fine	125	51	152	254	102	127	203
Medium	250	254	381	508	203	254	406
Coarse	635	508	660	1016	508	762	1270

Two billets of each matrix material were prepared with seeded inclusion particles from standard production powder mixes. For the HPSN billets, two halves of the final billet were cold pressed in 15.9 centimeter square steel dies. A template to aid defect placement was constructed of a manila paper frame with a rectangular lattice of thread. The lattice divided the central portion of the billet preform into 0.8 x 3.2 cm rectangles, as shown in Figure 3. The particles to be seeded as inclusion defects were placed in the center of the rectangles, in the manner indicated, onto the top face of the preform still within the die. The seeding of the contaminant particles was accomplished by various methods. The larger particles were readily transferred with a curved forcep or vacuum tweezers. Because of their smaller size, the finer particles were considerably more difficult to manipulate

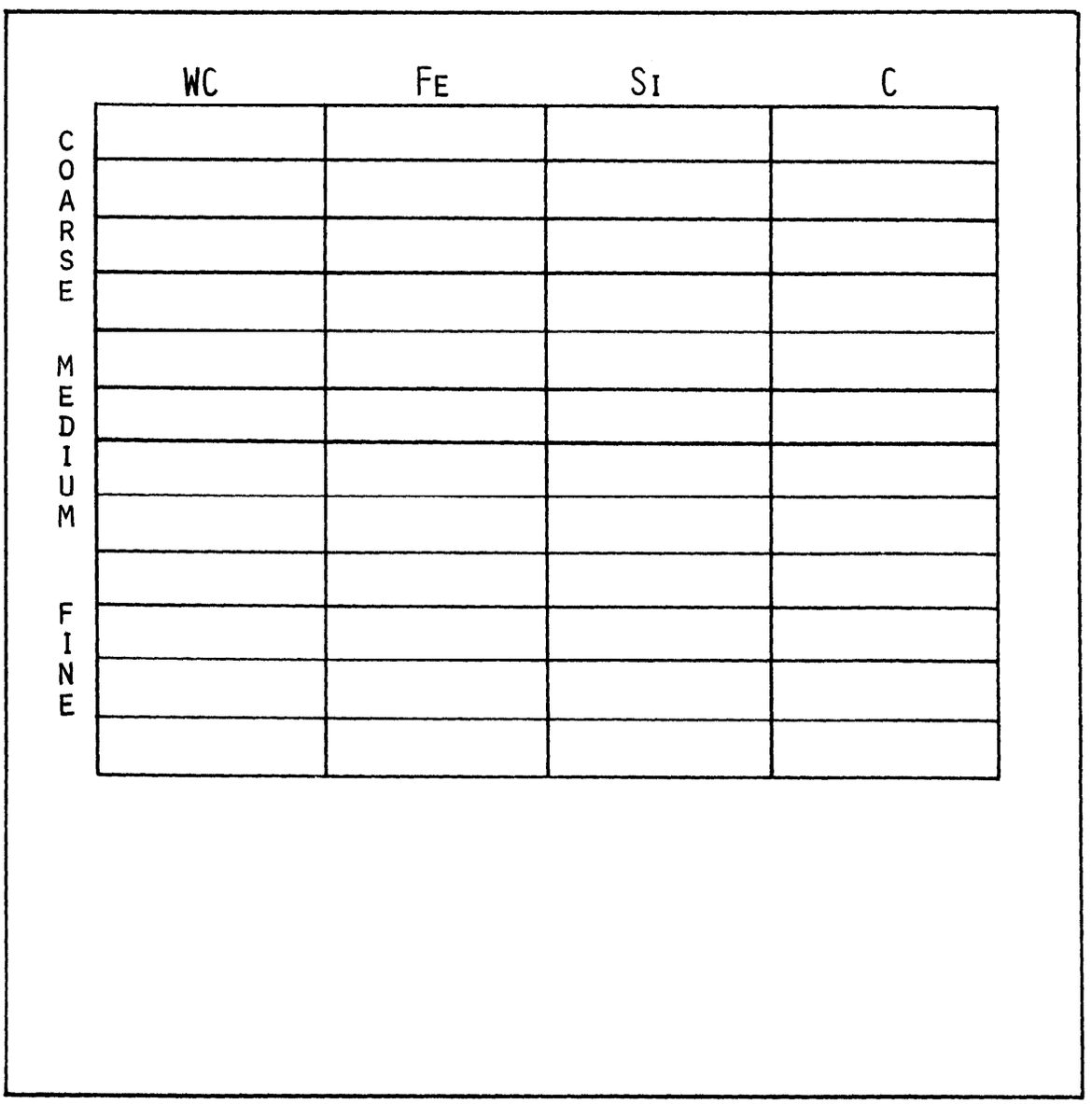

Figure 3. Defect seeding plan for NC-132 HPSN billets.

and more than one fine particle was sometimes placed within a given rectangle. A satisfactory method of single fine particle transfer was to attach a particle to a hair with static electricity and locate the defect in position with the aid of a five power loupe. After particle seeding, the second half of the preform was inserted into the steel mold and the two halves were pressed together prior to stripping from the steel mold and insertion into the graphite mold for hot pressing.

A somewhat similar procedure was followed for the production of the seeded NC-435 silicon carbide billets. One half of the weight of the raw material mix for a billet was poured into a 15.2 cm square graphite firing mold and leveled. The positioning template in this case consisted of 1.1 x 3.2 cm rectangles and the particles were placed in the arrangement shown in Figure 4. Following particle placement, the remaining material mix was added to the mold cavity and the total mass was pressed prior to the silicon carbide sintering step.

The areas outside the seeded regions of Figures 3 and 4 were used to supply specimens for baseline property determinations. This included room and high temperature bend strengths and chemical analysis.

Before high temperature firing, all billets were scribed to create a permanent orientation reference. Standard firing procedures were used for each material type.

The fired billets were given a light sand blasting to remove the thin surface reaction layer from firing. Billet bulk densities were measured by the Archimedean water displacement method and are reported in Table 2. All billets exceeded the minimum density requirements for their respective specifications.

TABLE 2. BULK DENSITIES OF SEEDED BILLETS

Billet Specification	Bulk Density (g/cc)
NC-132 HPSN, Top	3.22
NC-132 HPSN, Bottom	3.21
NC-435 SiC, #1	3.00
NC-435 SiC, #2	3.00

Samples were taken from unseeded areas of one of the silicon nitride and one of the silicon carbide billets for chemical analysis. The majority of the analyses were obtained by emission spectroscopy. The oxygen and carbon contents of the HPSN were

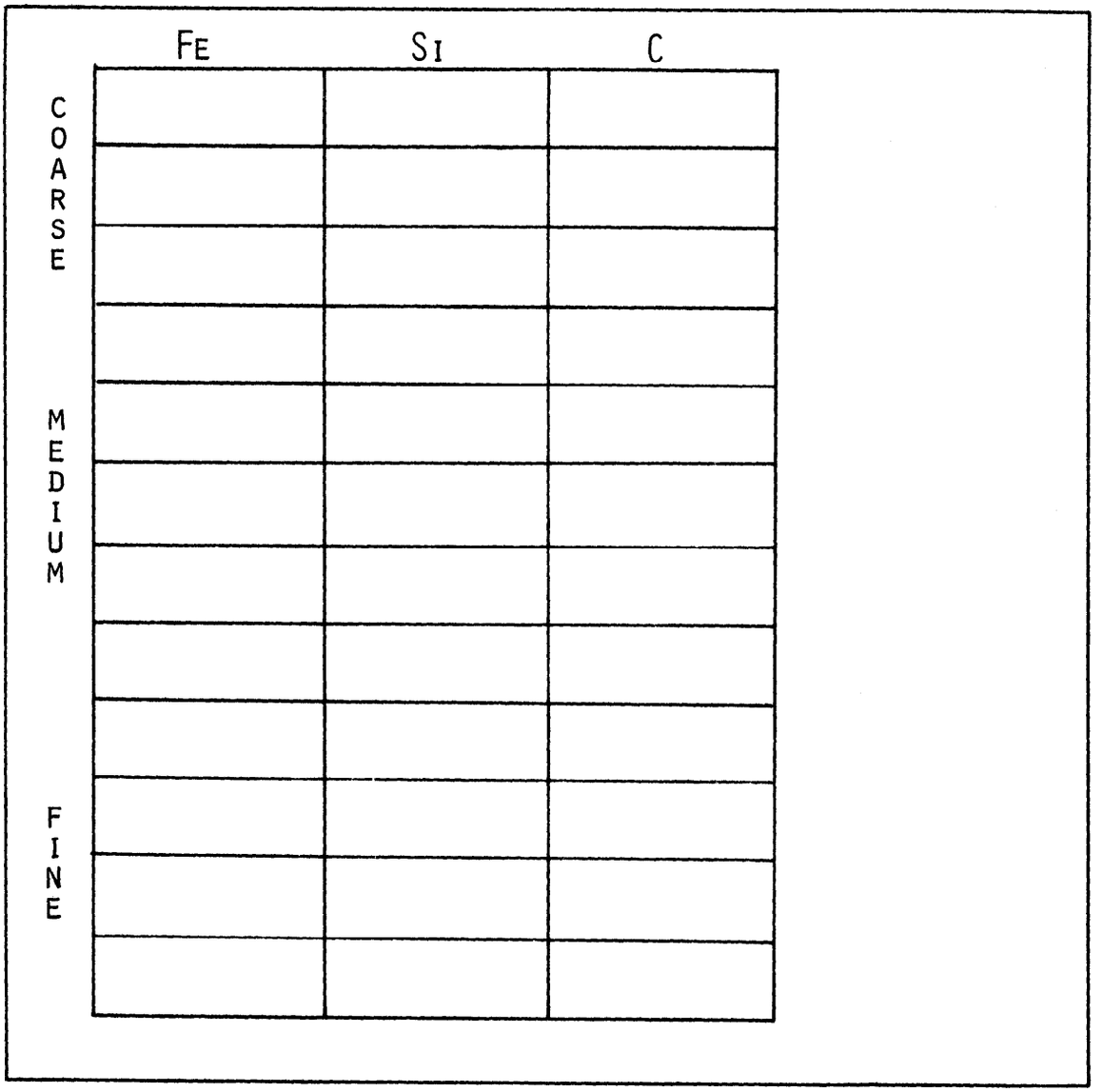

Figure 4. Defect seeding plan for NC-435 SiC billets.

obtained by an inert gas fusion technique. The chemical analyses are reported in Table 3 and are representative of these materials.

TABLE 3. CHEMICAL COMPOSITION (weight percent) of NC-132 HPSN and NC-435 SiC BILLETS

NC-132 HPSN Analyses (w/o)		NC-435 SiC Analyses (w/o)	
Al	0.14	Al	0.26
Fe	0.22	Fe	0.34
Ca	0.06	Ca	0.04
Mg	0.53	MG	0.02
W	1.8	W	0.01
Co	0.01	Co	0.01
Mn	0.01	Mn	0.01
O	1.53		
C	0.46		

Maps of the seeded inclusion locations (i.e. Figures 3 and 4) were prepared to assist in the nondestructive evaluation (NDE) of the billets. The maps and the billets, in the as-sand blasted surface condition, were forwarded to AMMRC where the nondestructive testing was performed.

B. NONDESTRUCTIVE TESTING

1. Introduction

The objective of the nondestructive testing portion of this program was to evaluate the effectiveness of existing nondestructive test practices at AMMRC for inspectin the ceramic samples. The methods utilized had to be optimized by suitable parameter control to obtain significant results on the ceramic materials. Nondestructive test methods included in the evaluation were ultrasonics, radiography, eddy current and penetrant.

2. Ultrasonics

a) Pulse-Echo Flaw Detection - Broadband high resolution ultrasonic test equipment was required to successfully detect discontinuities in the ceramic samples. This was not unexpected since the total transit time of an ultrasonic pulse in the sample plate thickness was less than one microsecond. The transducer which alternately acts as a transmitter and receiver in a pulse-echo test does not have enough time to stop ringing in this short interval with a narrow-band test system. Therefore, any received

signal from discontinuities is blocked by the remaining vibration of the transmitted pulse in a contact test or the front surface reflection in immersion testing. The high resolution system available for this work still produced a blind area equivalent to almost half the thickness of the sample plates. The billets had to be turned over and reinspected from the opposite side to cover this blind area.

Discontinuities detected by ultrasonic pulse-echo inspection were depicted by immersion C-scan techniques. The instrumentation used to inspect the ceramic specimens and produce C-scan records of the results was manufactured by Automation Industries, Inc. A Model US-454 laboratory ultrasonic scanning-recording system was utilized with a Type UM 771 Reflectoscope, Type 50S wide band Pulser/Receiver module operating in the 15 MHz to 50 MHz frequency range, and Type H Transigate. Several ultrasonic frequencies were evaluated from 10 MHz to 25 MHz. A 25 MHz lithium sulfate transducer, 0.79 cm diameter with a medium focus lens (5.1 cm focal distance in water and 1.27 mm beam diameter at the focal distance), was found to produce the best results for detecting the seeded defects and was therefore used to inspect all four billets as well as the rough cut bars machined from these billets. The operating sensitivity of the 50S Pulser/Receiver was set at a maximum limited only by the electronic noise generated by the instrument itself. Structural or grain boundary scattering in this material at 25 MHz frequency was not a factor in setting sensitivity. The electronic signal gate of the H Transigate was adjusted in position and width to occur (in time) between the reflected top and bottom interface echoes of the ultrasonic pulse propagating through the thickness of the samples. Ultrasonic signals reflected from discontinuities within the material appear in the gate and are recorded as intensity marks on the C-scan recording. The recording scanner has a direct drive for accurate 1:1 full scale C-scan recording. The index increment was set at 0.127 mm per stroke for this work.

An attempt was made to inspect the billets in the as-processed condition without machining the surfaces. Figure 5 shows a resultant C-scan recording. An analysis of the cause of the indications in this recording revealed that a majority are interference effects from surface roughness. This result shows the necessity of surface machining prior to ultrasonic testing.

Figures 6 through 13 show pulse-echo C-scan recordings at 25 MHz frequency of the NC-132 and NC-435 billets following surface machining. The ultrasonic test reveals the presence of many defects in the billets that are not listed on the seed location maps. Ultrasonic indications from the coarse and medium seeded contaminants are obvious on the recordings. Identification of the fine contaminant indications on the C-scans is not quite as simple except in a few instances such as the Fe in NC-132 bottom billet and the Si in NC-132 top. Generally, ultrasonic indications

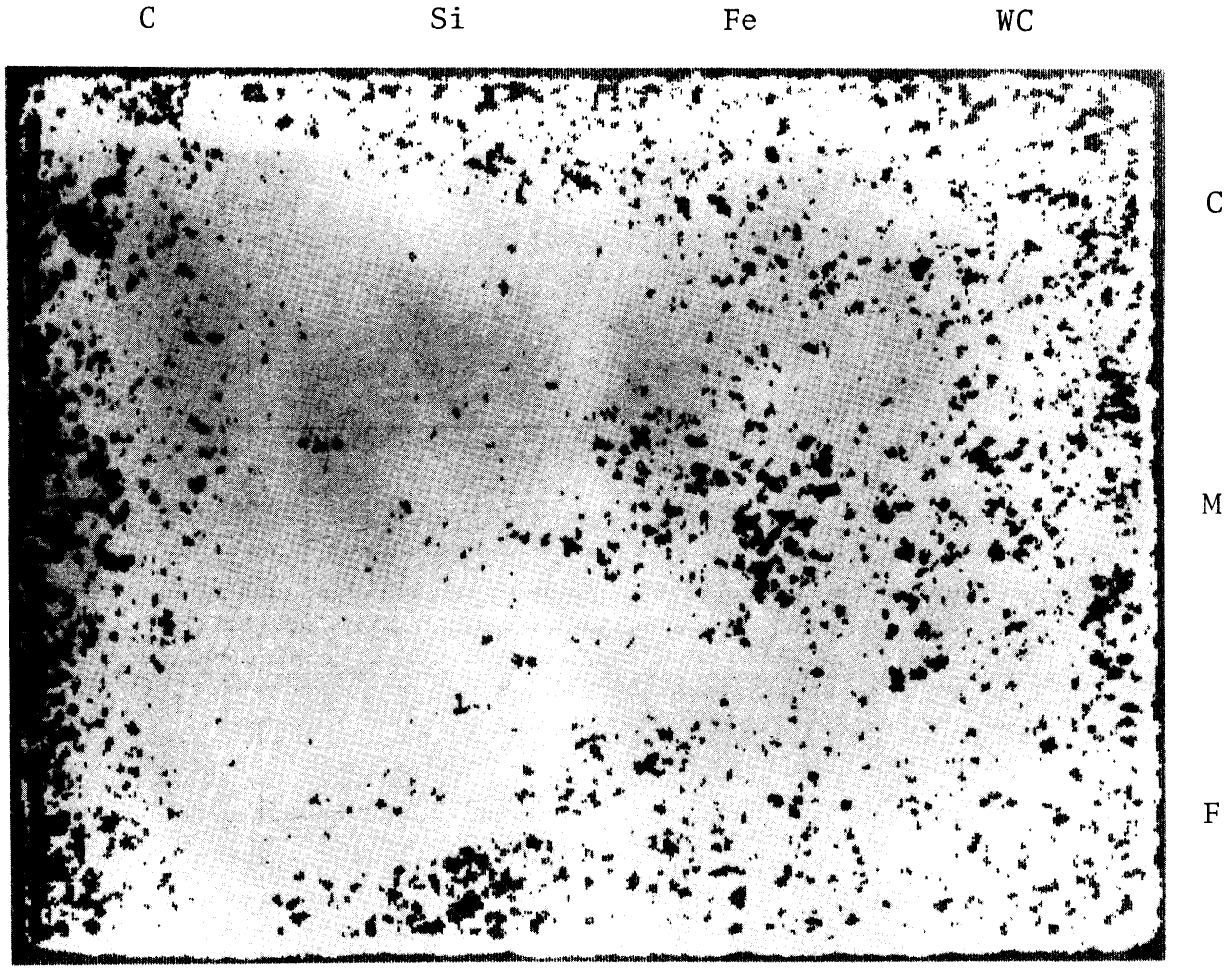

Figure 5. C-scan recording of NC-132 bottom billet in the as-pressed condition.

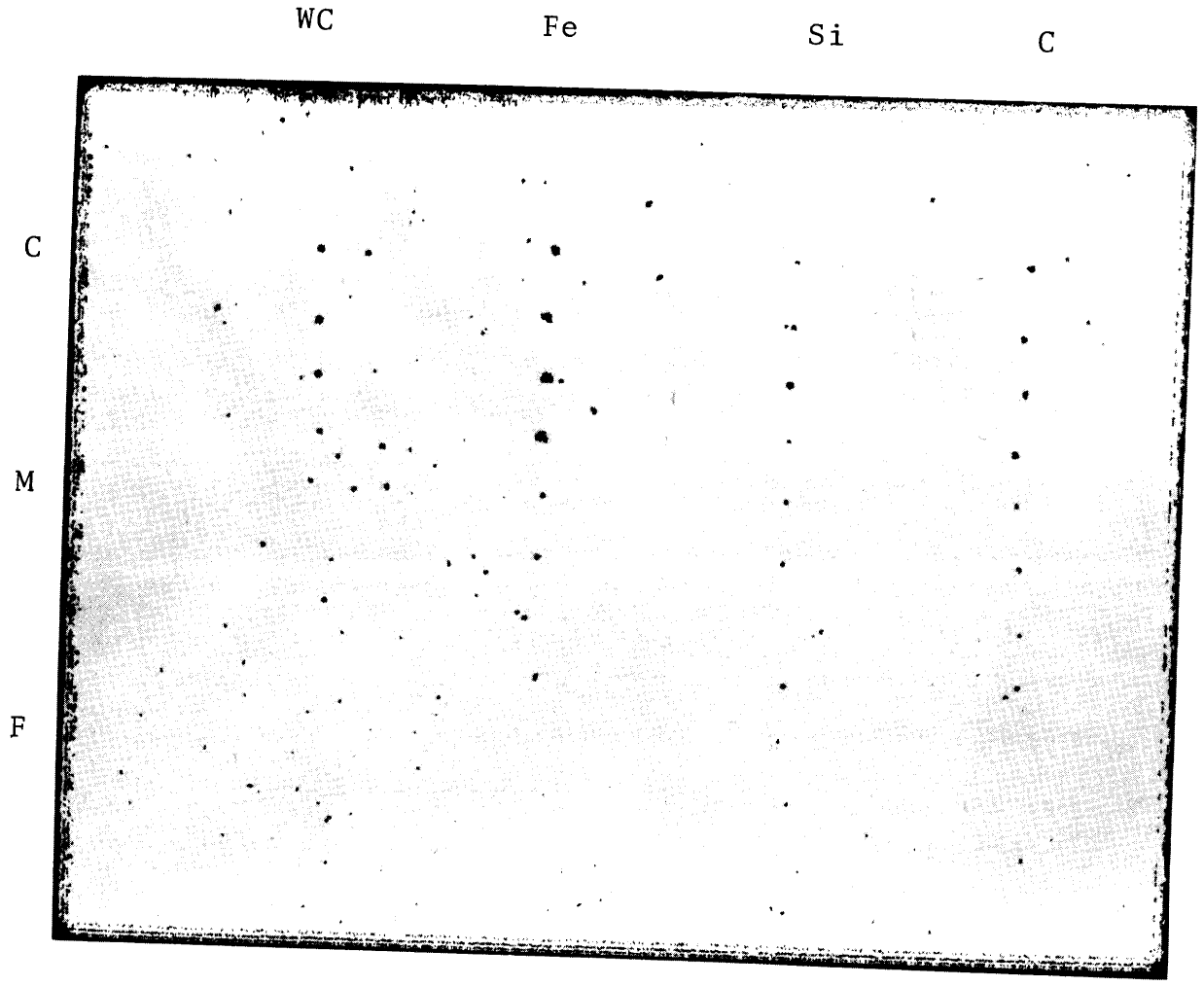

Figure 6. C-scan recording of NC-132 HPSN top billet in machined condition.

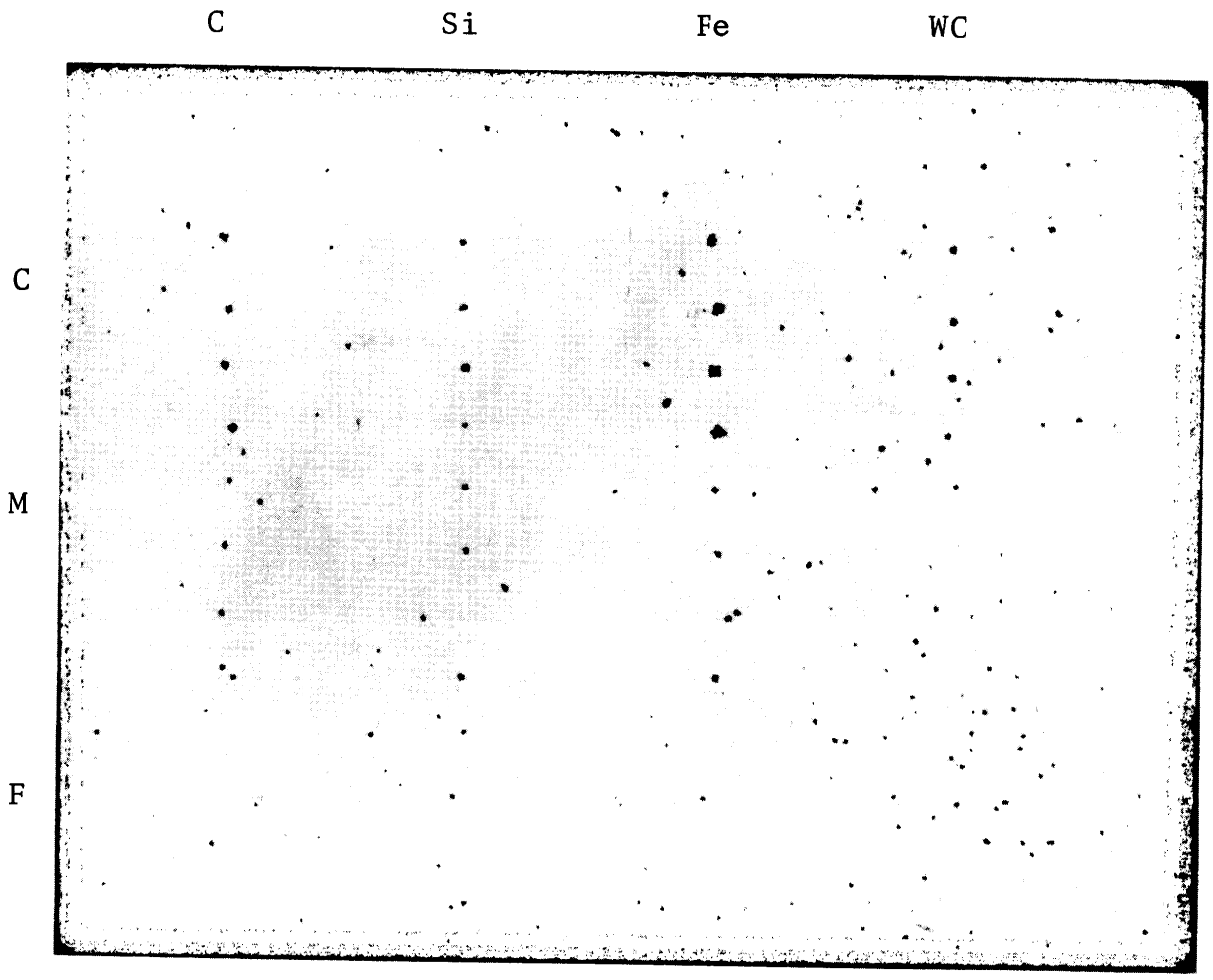

Figure 7. C-scan recording of NC-132 HPSN top billet, turned over, in machined condition

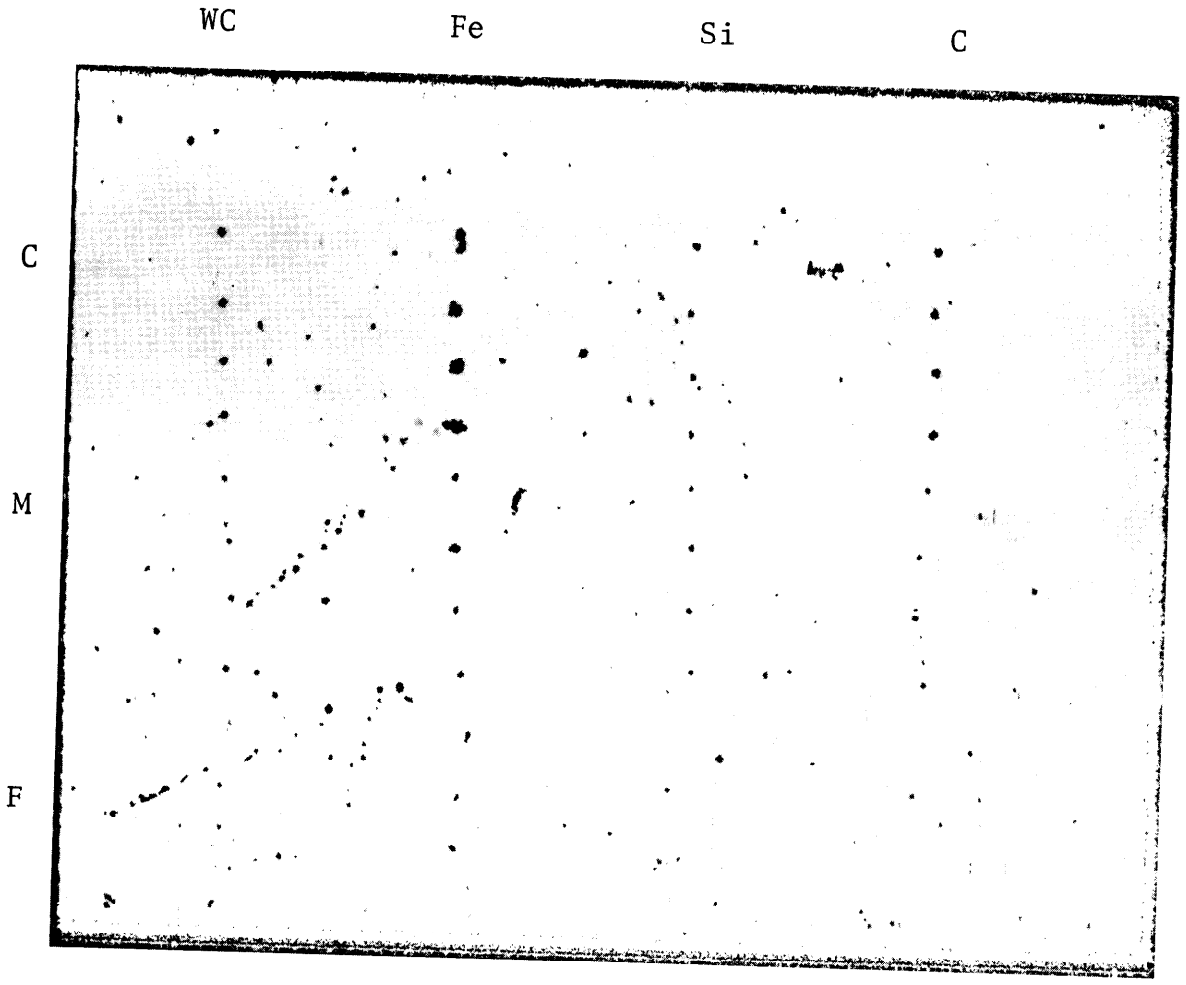

Figure 8. C-scan recording of NC-132 HPSN bottom billet in machined condition.

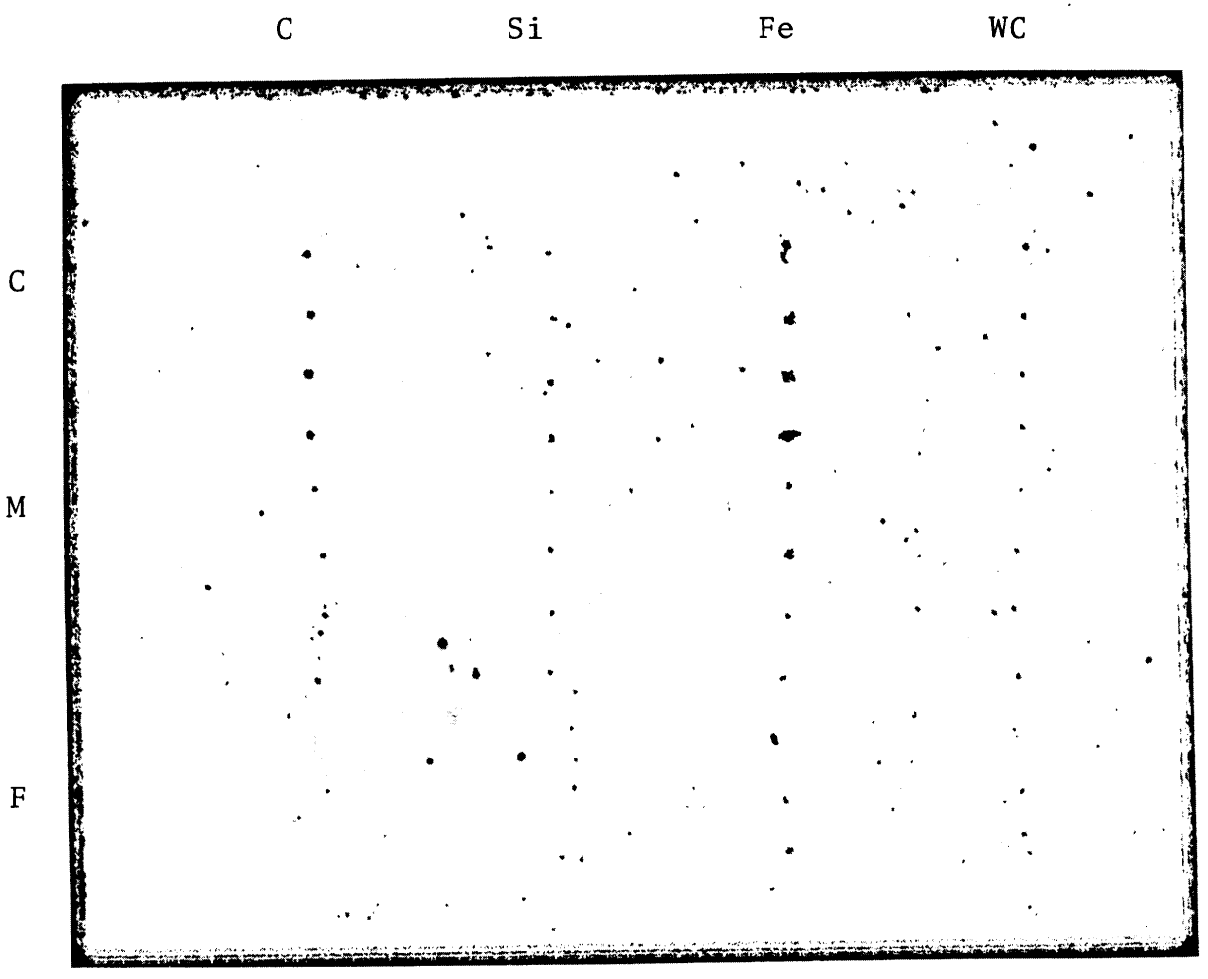

Figure 9. C-scan recording of NC-132 HPSN bottom billet, turned over, in machined condition

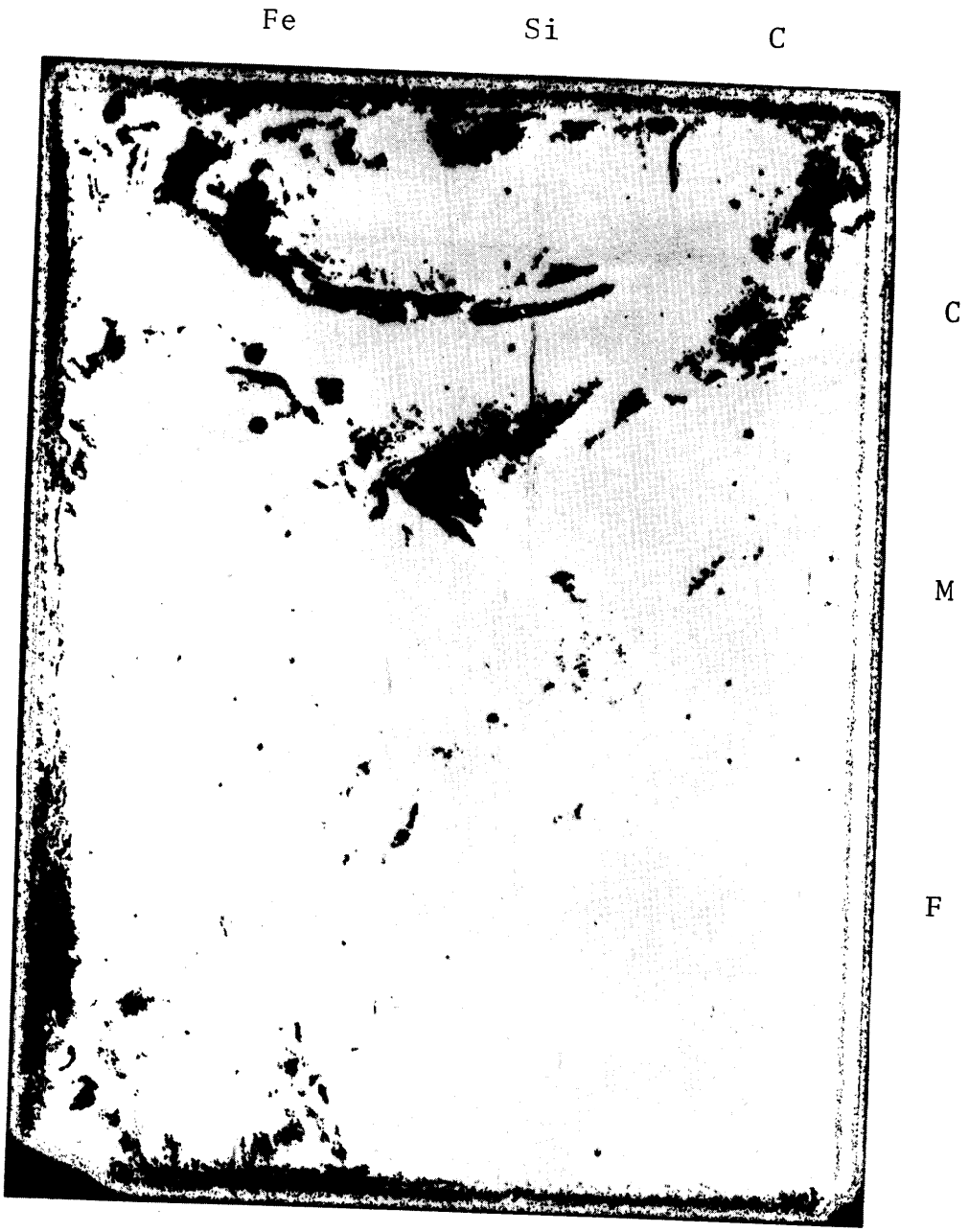

Figure 10. C-scan recording of NC-435 SiC #1 billet in machined condition.

Figure 11. C-scan recording of NC-435 SiC #1 billet, turned over, in machined condition.

Figure 12. C-scan recording of NC-435 SiC #2 billet in machined condition.

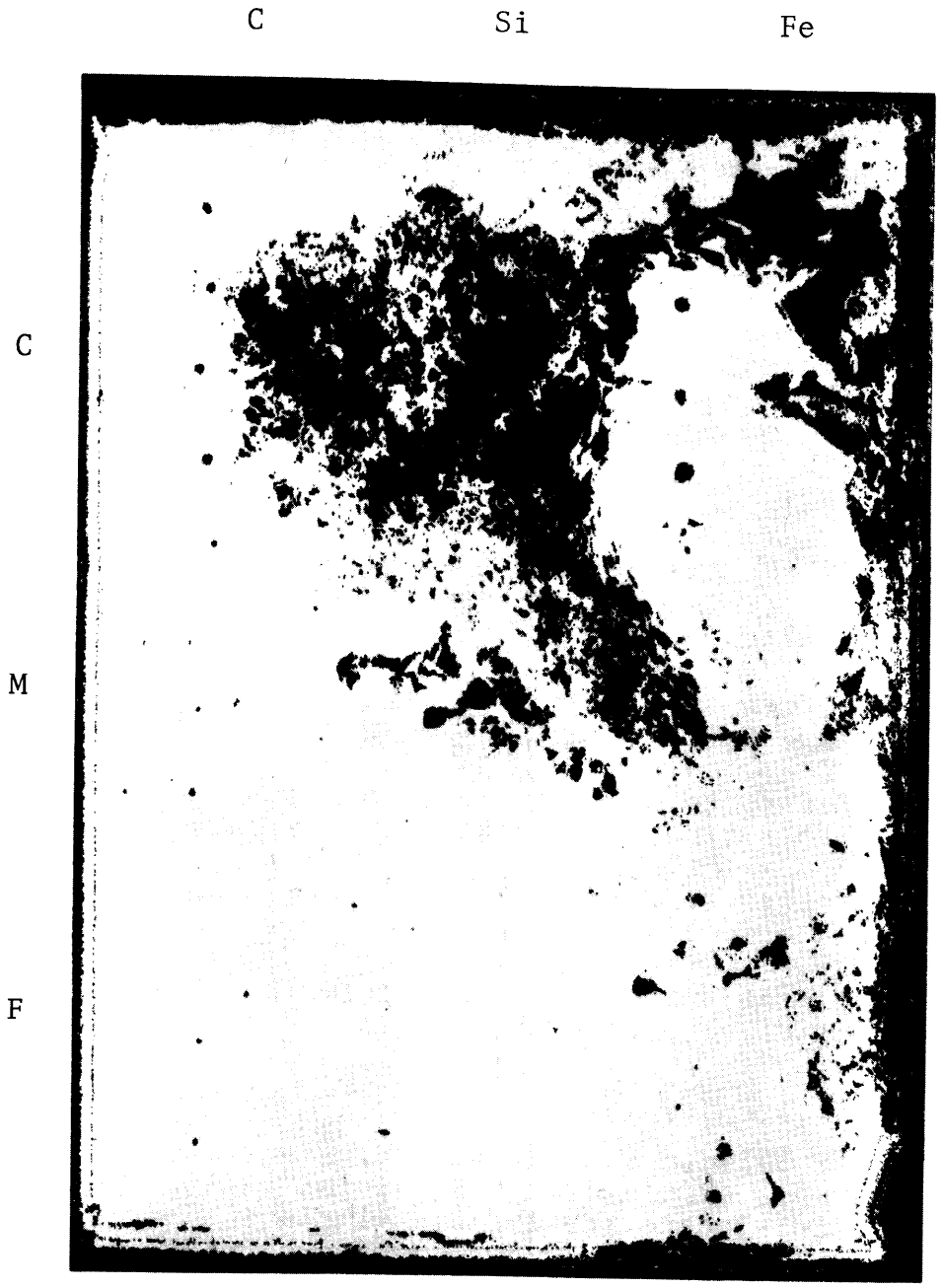

Figure 13. C-scan recording of NC-435 SiC #2 billet, turned over, in machined condition.

appear in the areas where the fine contaminants should be; however, they do not conform to the plan in position or number. Large areas of unplanned ultrasonic reflections effectively masked the flaw detection capabilities of the pulse-echo technique for the NC-435 billets. Some of the seeded contaminants are evident in areas free from these reflections.

After characterization of the billets by the other NDE methods, rectangular bars were sliced from the seeded areas of the billet plates. The cutting instructions for excising the bars were obtained from billet radiographs (see Section III and Figures 20-23). With the exception of minor alignment corrections, the slicing patterns were similar to the seeding grid patterns of Figures 3 and 4. In order to maintain bar identity and orientation with respect to the mother billet, the bars were marked with an indelible four place code immediately after slicing. The key to the four place code is given in Table 4.

TABLE 4 - EXPLANATION OF FOUR PLACE, W-X-Y-Z, SAMPLE BAR IDENTIFICATION CODE

W Place - Refers to billet identity: T = Top HPSN; B = Bottom HPSN; 1 = #1 SiC; 2 = #2 SiC

X Place - Refers to type of seeded particle: C = carbon; Fe - iron; Si = silicon; WC = tungsten carbide

Y Place - Refers to relative size of particle: F = fine; M = medium; C = coarse

Z Place - Iteration factor to distinguish between similar particles: numerals 1 through 4

Ninety-six silicon nitride and seventy-two silicon carbide bar specimens were examined by C-scans and radiography to characterize and better locate the defects within the bars. These bars were material blanks for bend bar specimens. The Appendix shows ultrasonic C-scans for a number of the rough-cut bend bars. The defect displays selected for illustration span the types and sizes of seeded particles and show variations in the number of defects detected per bar.

Also presented with these C-scans is a tabulation of the ultrasonic and radiographic defect indications according to their depth below the surface. The depth of each discrete ultrasonic reflection was measured using a scale mounted horizontally on the

oscilloscope screen. The accuracy of this method was approximately ±0.25 mm. The same information was measured from side-view radiographs of the bend bars. The depth of the defects was determined to about ±0.025 mm radiographically. The defect indications that coincided in location and depth were listed adjacent to each other to show apparent correlation between the two NDT methods.

b) Pulse-Echo Attenuation Measurements - Figures 14 and 15 are C-scan recordings of the variation in ultrasonic energy loss through the surface machined NC-435 billets. The recordings were made at 15 MHz frequency by monitoring the amplitude of the second back surface reflection. An Automation Industries Graphigate was used to produce tone shaded C-scans where the white areas represent a 3 db or 2 times loss of energy compared to the dark areas. Only NC-435 billets were scanned for ultrasonic attenuation in an attempt to explain the unplanned defect indications seen in Figures 10-13. The light areas on the attenuation scans correspond to the dark regions seen in the defect scans. The attenuation change is most notable at the boundaries of these regions. The circular indication at the right center of the C-scan of NC-435-1 billet is a scab that is only partially visible on the machined surface.

c) Velocity Measurements - Variation in chemical composition, porosity and microstructure that lead to a modulus change will show up as a change in the material's ultrasonic velocity. Ultrasonic velocity measurement then presents a means for assessing certain material properties of ceramics.

Point by point velocity measurements to determine property variations in the sample billets were made with a Panametrics 0.64 cm diameter 15 MHz broadband contact transducer centered on each of the rectangular areas shown on the seed location maps. The technique consists of measuring the transit time of the ultrasonic pulse as it is reflected back and forth through the thickness of the sample billet. Transit time was measured by the pulse-echo overlap-method where pairs of echoes are electronically superimposed by driving the x-axis of a viewing oscilloscope with a CW sinusoidal signal properly adjusted to a frequency equal to the reciprocal of the travel time between echos. Measurement of this frequency can be made to a high precision by an electronic counter, and if the correct cyclic overlap for the rf within the echoes is chosen, very accurate measurement of ultrasonic velocity is possible.

The average longitudinal wave velocity for the NC-132 billets was 1.12 cm/μsec with a variation of less than 1 percent between measurements. The NC-435 billets had variations up to 3 percent with an average velocity of 1.21 cm/μsec.

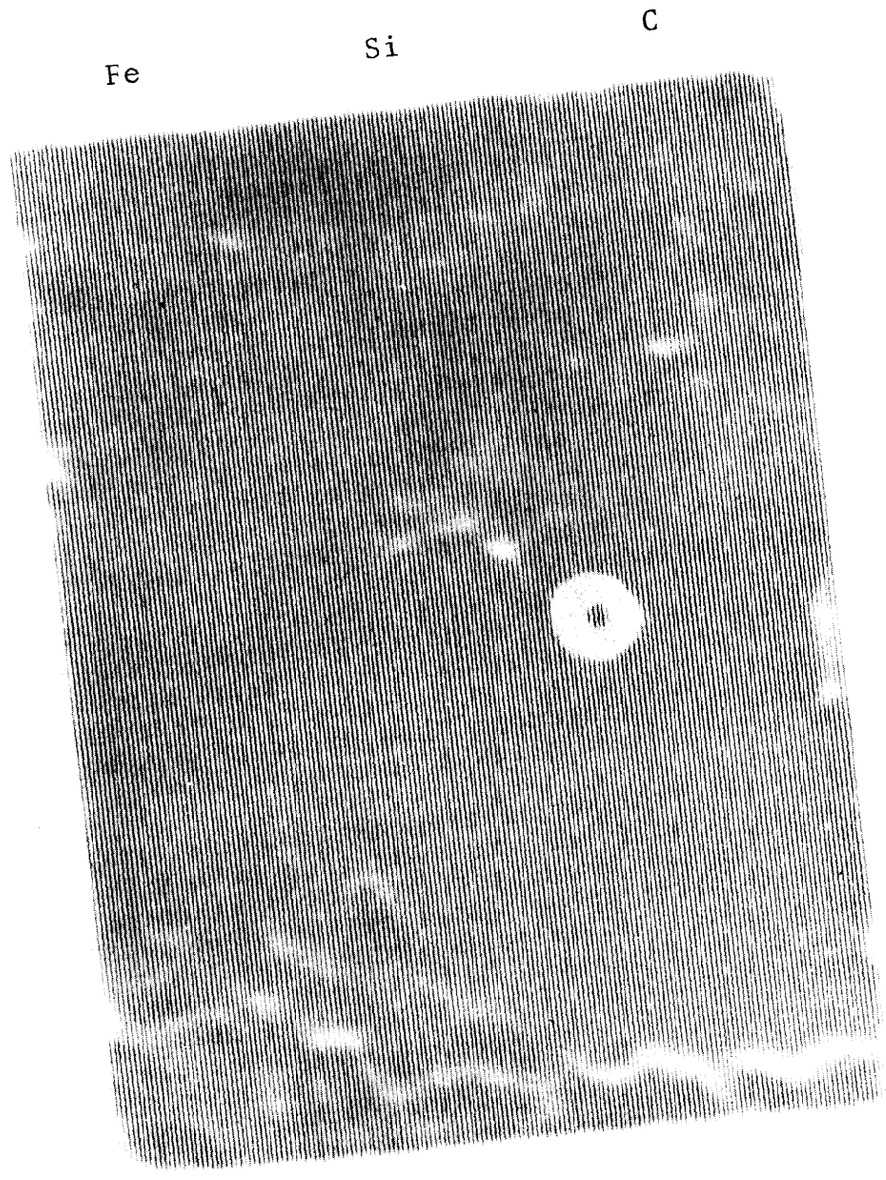

Figure 14. C-scan recording of attenuation changes in NC-435 SiC #1 billet.

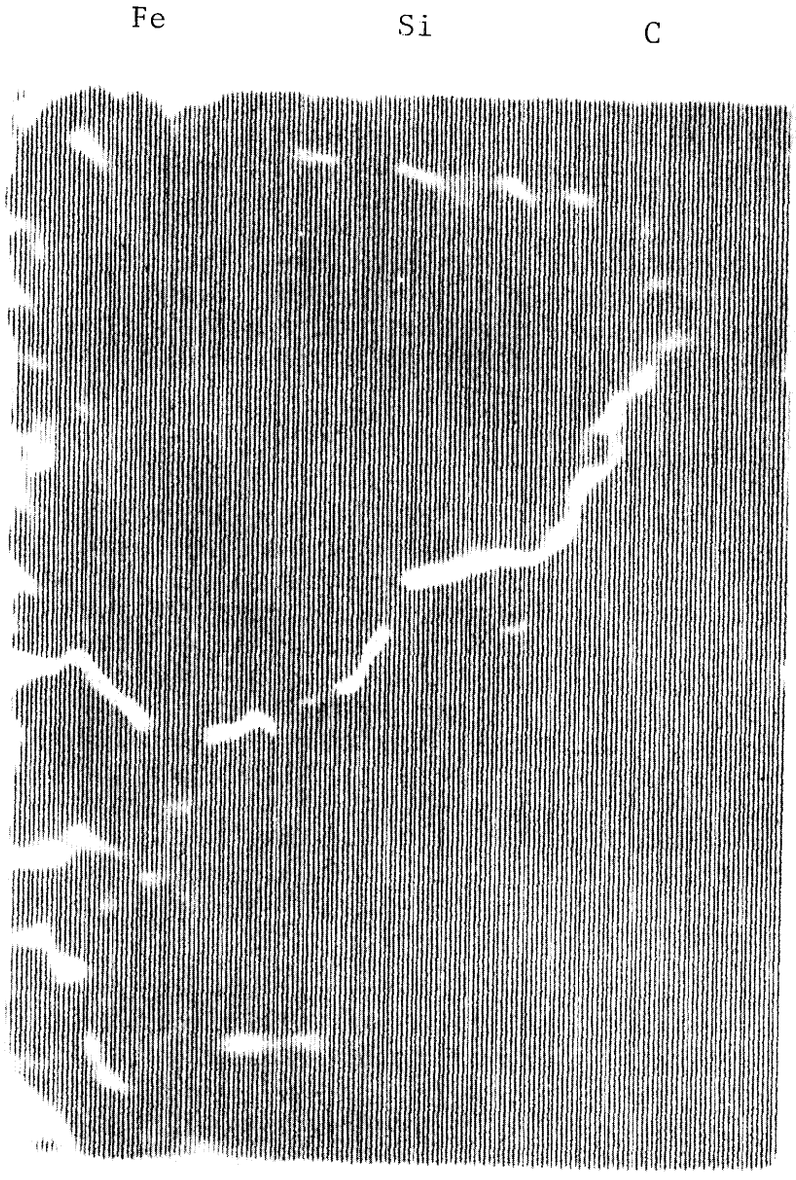

Figure 15. C-scan recording of attenuation changes in NC-435 SiC #2 billet.

3. Eddy Current

Changes in a materials properties or characteristics that affect the materials electrical conductivity can be evaluated by eddy current tests. Figures 16 and 17 show variations in eddy current NDT response as measured by the Automation Industries EM-3300 eddy current instrument on the NC-435 billets. Measurements were made at 1 MHz frequency with a 0.64 cm diameter probe coil centered on each of the rectangualr areas. The numbers represent deflection in centimeters on a cathode ray tube screen with the spot moving from o to 10 cm. The numerical values are only relative, showing variation in resistivity within a single billet. Some correlation is evident when the ultrasonic C-scans of Figures 10-15 are compared to the eddy current results. Since the silicon nitride is an excellent dielectric (non-conductor), eddy current readings could not be produced for the NC-132 material.

4. Liquid Penetrant

Each billet was examined by the liquid penetrant method for surface cracks, porosity and edge laminations. A Magnaflux post-emulsifiable fluorescent penetrant ZL-22 was used on the sample billets with a ZE-3 emulsifying agent and a ZP-4 dry developer. Several laminations and cracks were detected on the edges of both of the NC-435 billets and surface indications were noted on NC-435-1 billet. These results are illustrated in Figures 18 and 19. The cracks are mostly visible using a hand glass. The depth of these cracks is indicated in ultrasonic C-scans, Figures 10-13 as shaded areas at top, bottom, and left sides of the C-scans. The NC-132 billets were free of liquid penetrant indications.

5. Radiography

A radiographic inspection was conducted of the billets both in the as-pressed condition and after machining using a Norelco 300 x-ray unit. Other radiographic parameters were as follows:

KVP: 60
MA: 15
Exposure Time: 2 minutes, 30 seconds
Penetrameter: Aluminum step wedge
Target Film Distance: 76.2 cm
Screens: None
Focal Spot: 0.4 mm
Film Type: Kodak M

The radiographs of the as-pressed NC-132 billets showed all sizes of the tungsten carbide and iron contaminants. The large low density graphite particles were seen with some difficulty as

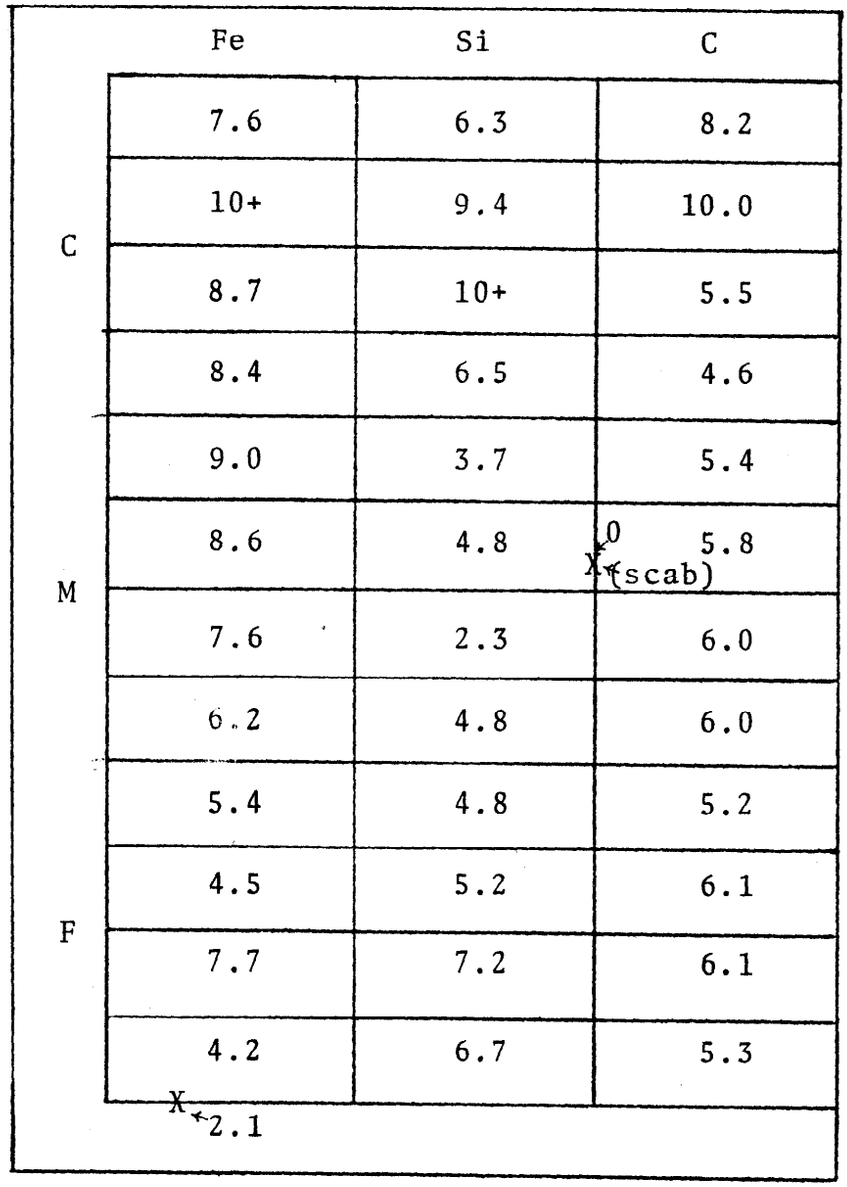

Figure 16, Variations in eddy current response of NC-435 SiC #1 billet

	Fe	Si	C
C	2.8	5.0	7.0
	3.0	6.0	7.6
0 X	0.2 X 3.5	2.8	8.5
	2.3	2.9	10.0 X 8.4
M	1.4	9.5	7.0
	2.0	7.5	6.4
	2.8	6.2	6.2
	5.0	6.0	5.6
F	6.2	5.4	5.4
	4.9	4.9	4.6
	3.0	3.6	4.0
	3.1	2.4	2.0

Figure 17. Variations in eddy current response of NC-435 SiC #2 billet

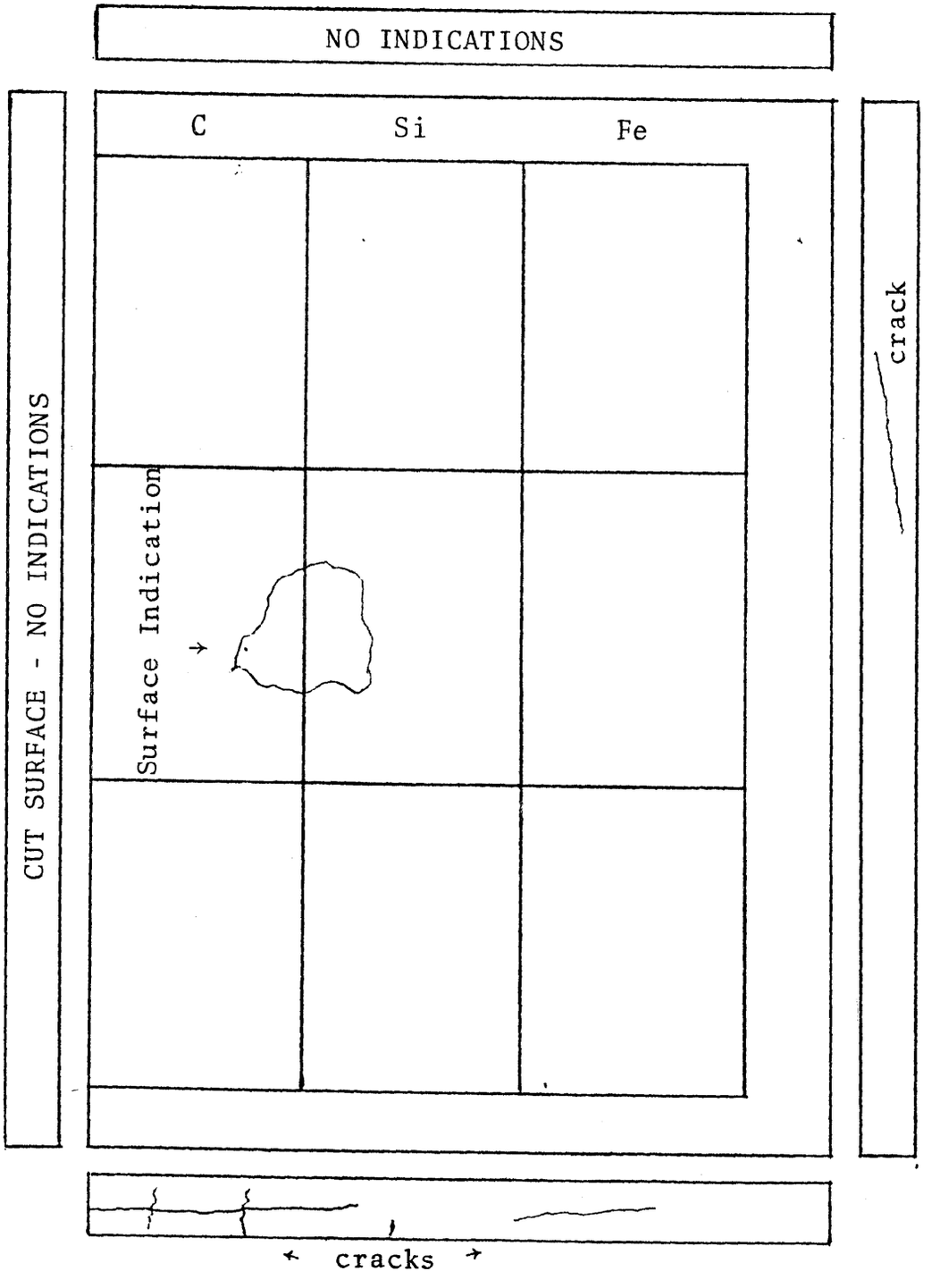

Figure 18. Map of liquid penetrant indications on NC-435 SiC #1 billet

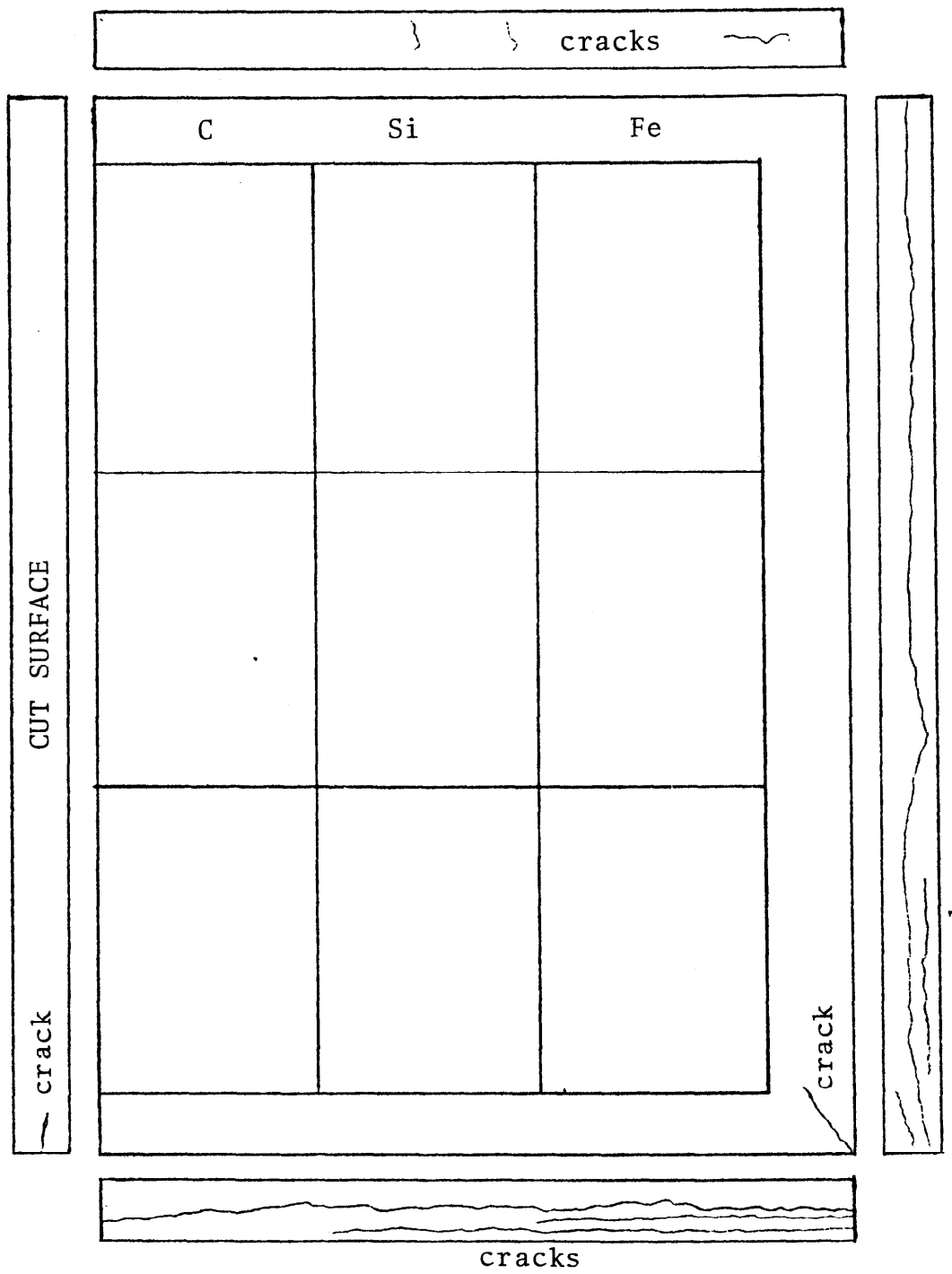

Figure 19. Map of liquid penetrant indications in NC-435 SiC #2 billet

they blend in with the surface roughness. A cloud of dense particles about 0.13 mm diameter was seen in the radiograph of NC-132 top billet. They are scattered both around and below the tungsten carbide row and are about thirty in number. The iron particles are shaped like a crude X. No seeded contaminants were visible in the as-pressed NC-435 billets.

The maps that appear in Figures 20-23 were prepared manually from the radiographs taken of the billets after surface machining. Although the location of the defect images are accurate, sizes are not. Tungsten carbide and iron contaminants show as more dense relative to the matrix and silicon and graphite as less dense in the original radiographs. The visibility of the high density seeded and unintentional defects in the NC-132 billets is about the same as in the radiographs taken in the as-pressed condition. The large, low density seeded defects can be seen more easily after surface machining. The map for NC-132 bottom outlines areas that show up as light, irregular markings on the radiographs. Only the large graphite particles, a surface scab, and an isolated large, high density inclusion are visible in the radiographs of the NC-435 billets.

The rough cut bend bars machined from the billets are radiographed on their side to determine the depth of defects. The results of the radiographic inspection of each bar are tabulated and compared with ultrasonic inspection in the Appendix. A feature of the radiographs of the NC-132 bars that does not appear in the listings is the distinct high density (radiographically) bondline that was visible in each bar. Although only a few discreet defects were detected in the NC-435 bars, high and low density striations were found running axially in virtually every bar.

C. STRENGTH TESTING

Bend bar specimens for a baseline strength characterization of the billets were cut from unseeded regions of the billets. These samples were 3.18 x 3.18 x 38.1 mm in size and were finish ground in a direction parallel to the bar axis with a 320 diamond grit wheel. Bar edges were ground to a bevel to suppress fracture initiation from edge cracks.

Bend bars containing seeded defects were prepared from the rough-cut material blanks. The C-scans of the individual blanks were used to select a defect which was intended to be the fracture origin when the bar was broken. In order to be selected as a target defect, the defect had to be in the central half of the length of the bar so as to be located within the inner load span during the four-point bend testing. An amount of stock removal, intended to place the defect close to a newly machined surface, was computed from the NDE depth indications and the thickness of the blank. The stock removal positioned the defect approximately 0.1 - 0.3 mm from the new surface so that the defect would be

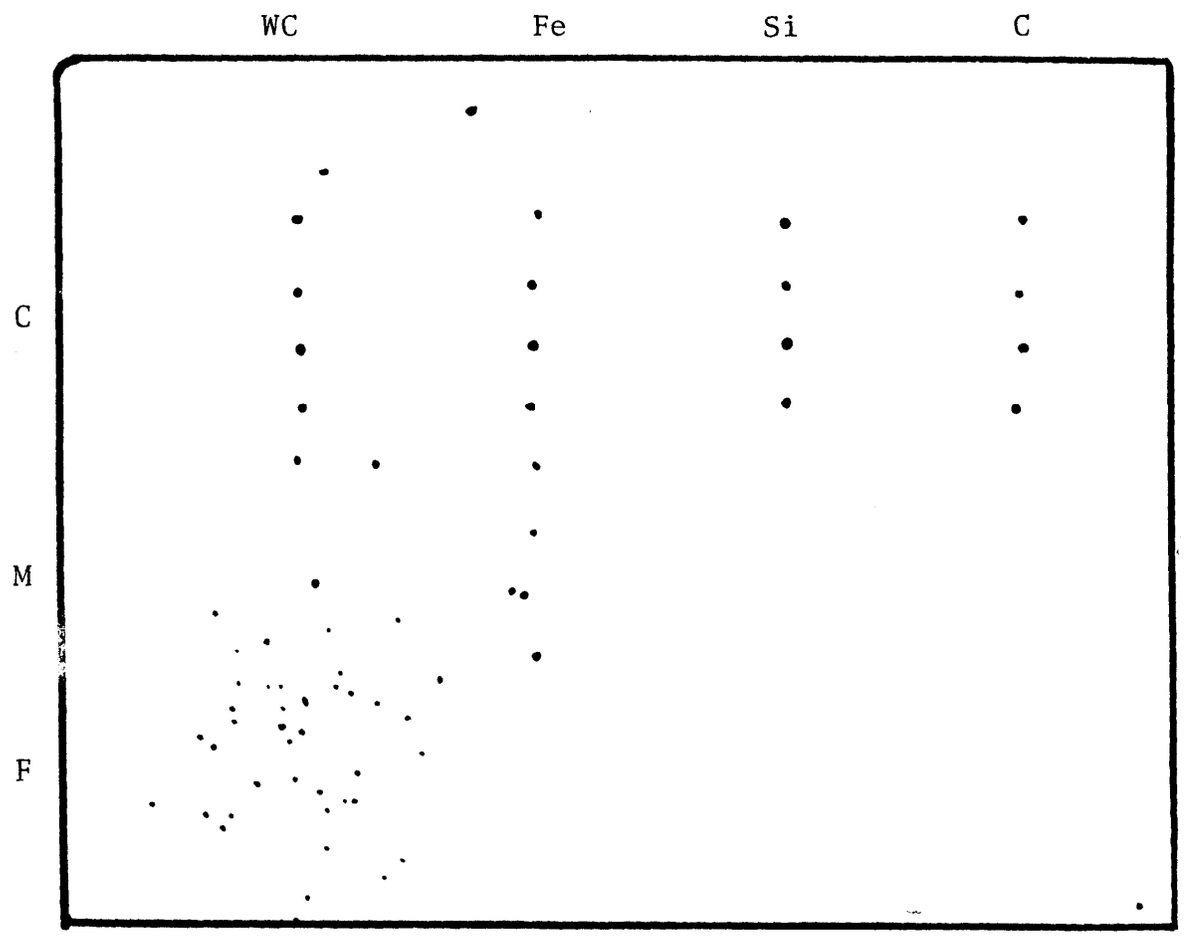

Figure 20. Map of radiograph of NC-132 HPSN top billet

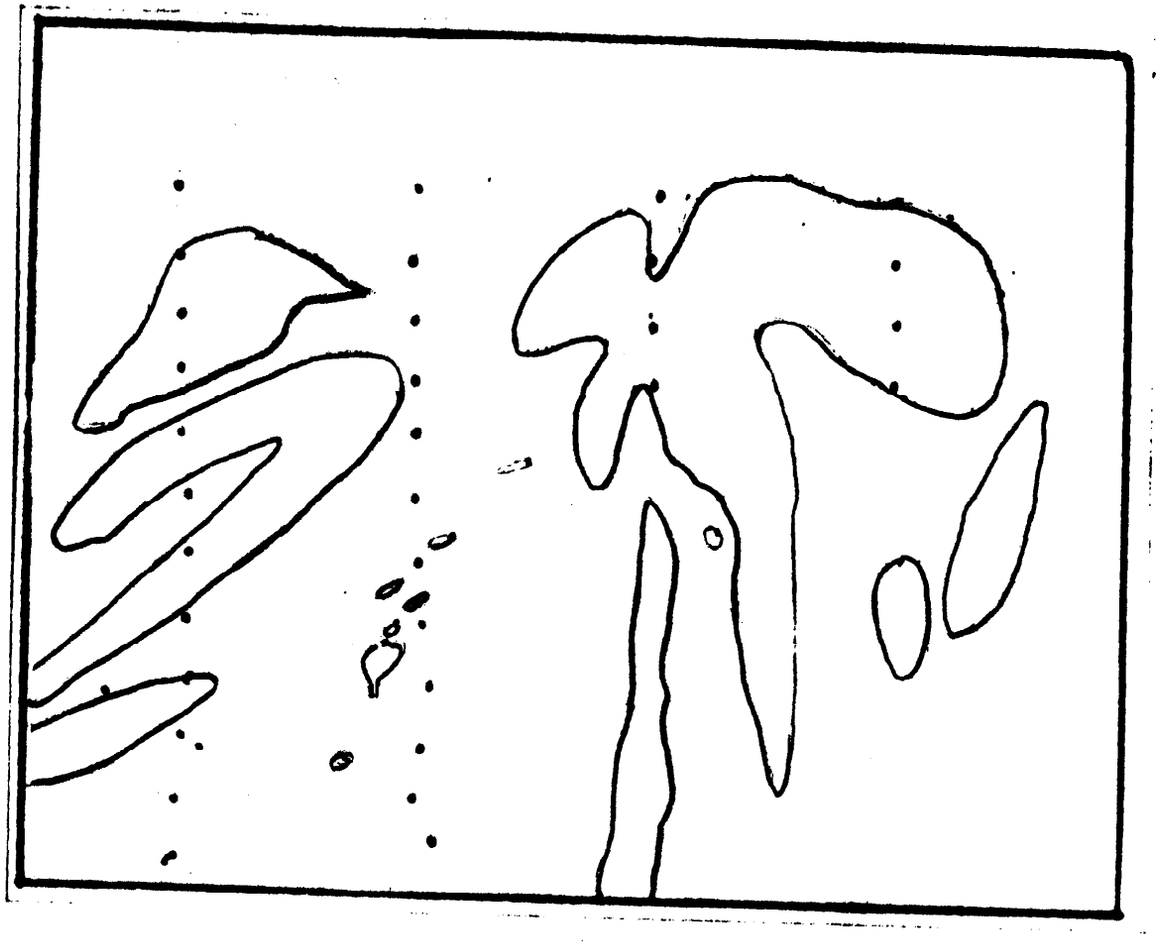

Figure 21. Map of radiograph of NC-132 HPSN bottom billet.

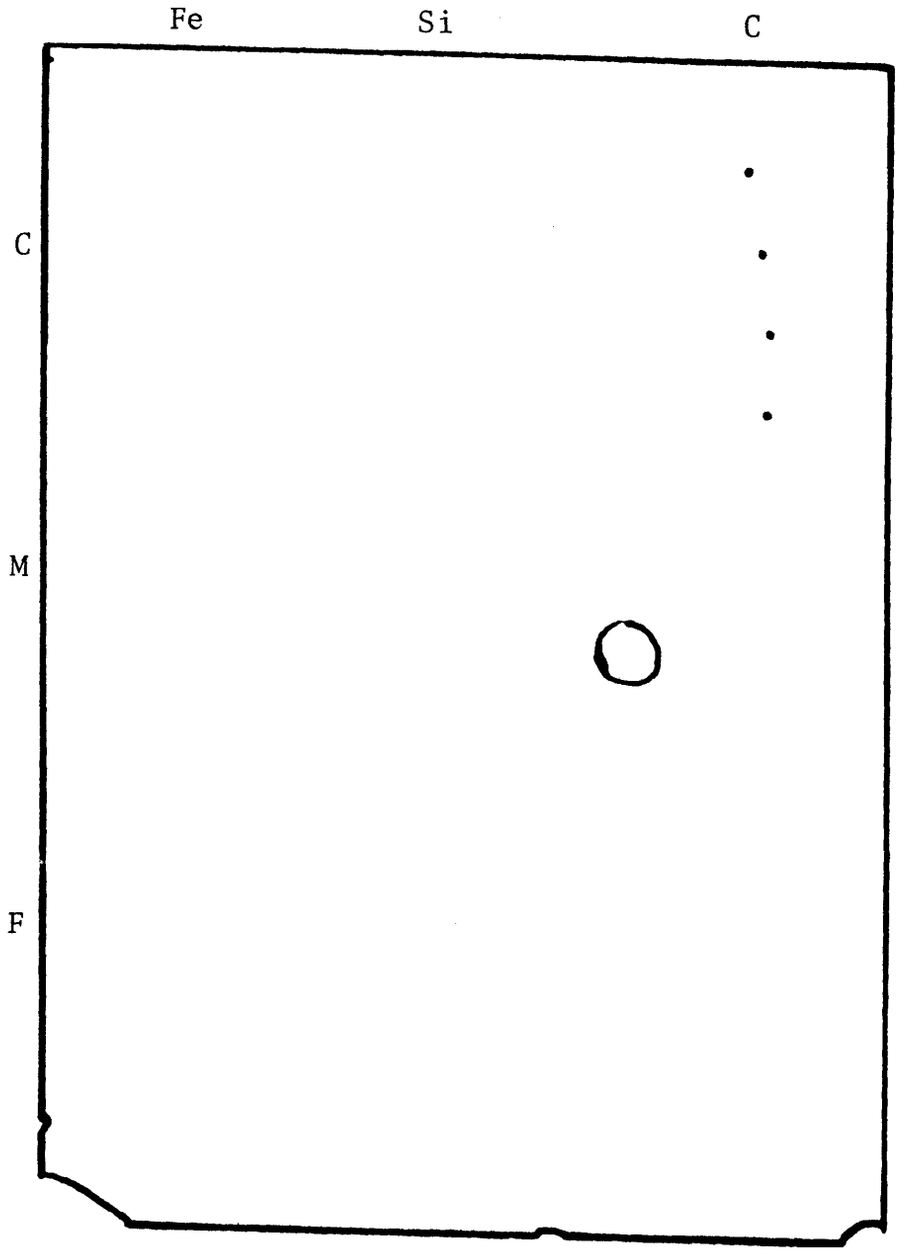

Figure 22. Map of radiograph of NC-435 SiC #1 billet

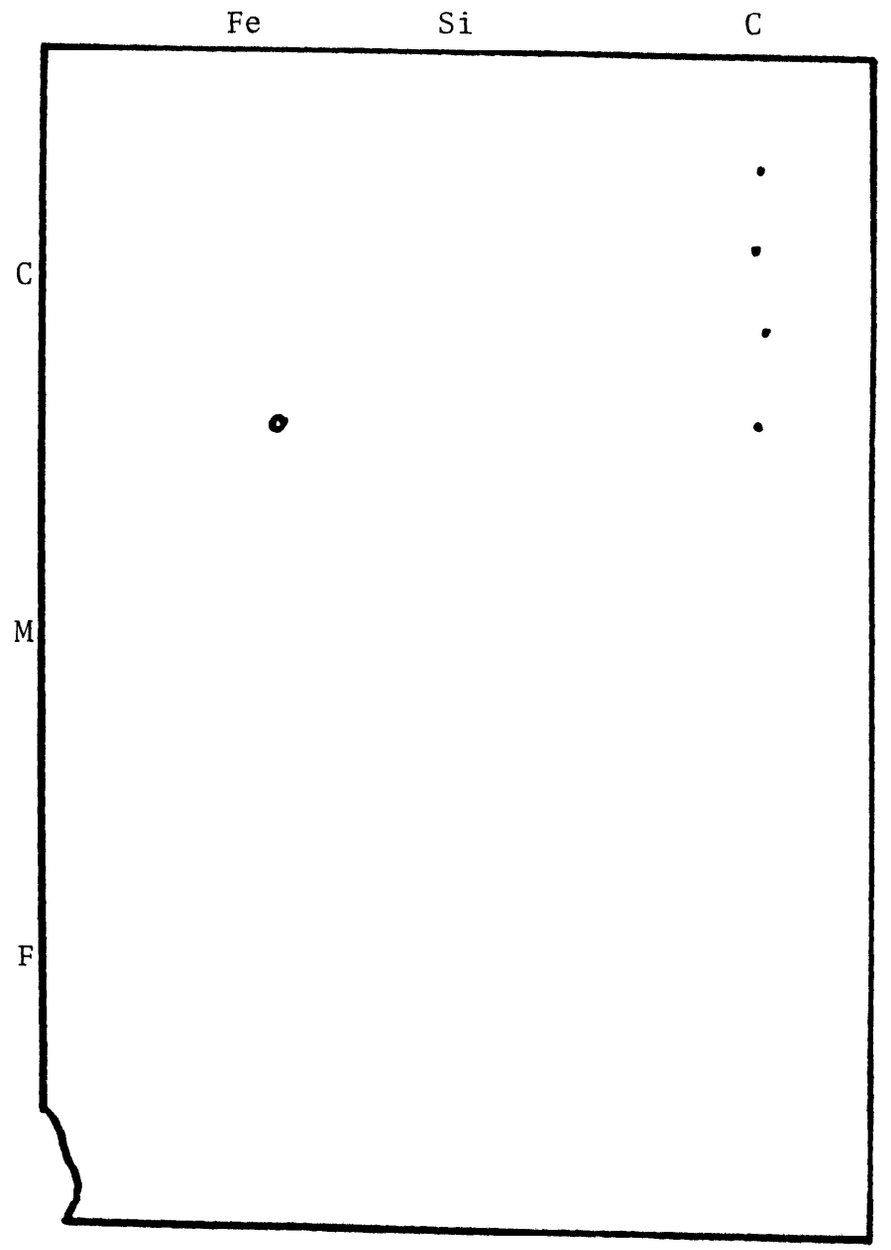

Figure 23. Map of radiograph of NC-435 SiC #2 billet

highly stressed in the bend test, thereby increasing the probability that it would initiate the bend test fracture. If the depth of the targeted defect was determined by both ultrasonics and radiography, the radiographic distance was used to compute the amount of stock removal because of its greater accuracy.

Stock removal was accomplished with a 320 grit diamond, resinoid bonded wheel by grinding in the direction of the bar axis. The side faces of the bars were lightly ground to remove slicing scratches and edge chips. The bar edges were not beveled as preliminary bend testing showed that the defect stress concentrations and the quality of the finishing operation were sufficient to cause fracture initiation at an inclusion with a high degree of probability. The finished size of seeded HPSN bend bars was length = 38 mm, width = 6 mm and thickness = 2.7-3.7 mm. The finished size of the silicon carbide bars was similar, except the nominal width was 9.5 mm.

Room temperature bend testing was conducted with a four-point bend fixture of steel construction. The jig was articulated to minimize errors from specimen misalignment or nonparallel faces. Fixture spans were 12.7 mm over 25.4 mm. Loading was done in a mechanical testing machine with a crosshead rate of 0.51 mm/min. The specimen Modulus of Rupture (MOR) stress was calculated from the four-point flexure formula:

Eq. 1

$$\sigma \text{ MOR} = \frac{3 \text{ L a}}{\text{w t}^2}$$

where,

σ MOR = fracture stress
L = fracture load
a = moment arm
w = specimen width
t = specimen thickness

Room temperature four-point bend strengths for specimens cut from unseeded portions of the HPSN and the SiC billets are given in Tables 5 and 6, respectively. The unseeded strengths for the NC-132 HPSN billets (Table 5) are somewhat below normal for this material. The mean strength of 380 samples derived from the last 40 NC-132 HPSN billets was 834 MN/m^2 with a standard deviation of 129 MN/m^2. The lower strength of the program's billets is attributed to the greater handling of the powder and the concomitant introduction of unintentional defects. Room temperature strengths for the seeded HPSN and SiC specimens are given in Tables 7 and 8, respectively.

Elevated temperature strength testing was conducted in a three-point bending fixture with alumina loading supports and a

TABLE 5

Room Temperature Bend Strength of NC-132 HPSN Specimens Cut From Unseeded Area of Billets

Break Number	MOR Stress (MN/m^2)	
	Billet T	Billet B
1	644	613
2	473	517
3	676	745
4	727	739
5	604	666
6	751	429
7	826	645
8	829	812
9	817	628
10	841	679
11	698	543
12	894	778
Average	732	650
Standard Deviation	121	113

TABLE 6

Room Temperature Bend Strength of NC-435 SIC Specimens Cut From Unseeded Area of Billets

Break Number	MOR Stress (MN/m^2)	
	Billet 1	Billet 2
1	316	292
2	325	264
3	392	269
4	519	301
5	304	361
6	515	303
7	337	325
8	398	321
Average	388	305
Standard Deviation	86	32

TABLE 7

Modulus of Rupture, optical fractographic and inclusion detectibility data for HPSN bend bars broken at room temperature.

Specimen	σ MOR (MN/m^2)	Fracture Origin Location[1]	Inclusion Dimensions[2] (0.001") X	Y	Z	Inclusion Detection[3] US	XR
B-C-F-2	509	I	8	3	10	X	
B-C-F-4	502	I	15	2	14	X	
B-C-M-1	572	S		NA[4]			NA
B-C-M-2	639	I	2	1	4		
B-C-M-3	487	I	17	5	10	X	
B-C-M-4	574	I	5	2	3	X	
B-C-C-1	510	I	4	6	6		
B-C-C-2	555	E		NA			NA
B-C-C-3	548	I	0	2	2		
B-C-C-4a	772(?)	I	6	7	11	X	X
B-C-C-4b	772(?)	I	4	1	1		
B-Fe-F-2	444	I	6	6	8	X	X
B-Fe-M-1	372	I	8	12	12	X	X
B-Fe-M-2	450	I	9	5	13	X	X
B-Fe-M-3	401	I	10	8	17	X	X
B-Fe-M-4	417	I	9	16	17	X	X
B-Fe-C-2	238	I	8	35	44	X	X
B-Fe-C-3	258	I	10	32	44	X	X
B-Fe-C-4	291	I	5	34	22	X	X
B-Si-F-3	453	I	7	2	11	X	
B-Si-M-1	568	I	22	4	19	X	
B-Si-M-2	559	I	20	3	17	X	
B-Si-C-1	311	I	9	5	25	X	X
B-Si-C-2	304	I	12	10	35	X	X
B-Si-C-3	378	I	15	5	35	X	X
B-Si-C-4	337	I	11	10	27	X	X
B-WC-F-1	525	I	0	2	3	X	X
B-WC-F-2	553	I	9	3	7	X	X
B-WC-F-3	598	I	8	5	6	X	X
B-WC-F-4	633	S		NA			NA
B-WC-M-1	576	I	18	3	12	X	X
B-WC-M-2	520	I	5	5	10	X	X
B-WC-M-4	414	I	6	3	6	X	
B-WC-C-3	625	I	10	18	26	X	X
T-C-F-4	556	I	2	1	1		
T-C-M-1	373	I	10	6	16	X	
T-C-M-2	352	I	10	7	15	X	
T-C-M-3	427	I	3	3	4		
T-C-M-4	305	I	8	5	11	X	

Continued

TABLE 7 (continued)

Specimen	σ MOR (MN/m^2)	Fracture Origin Location[1]	Inclusion Dimensions[2] (0.001") X	Y	Z	Inclusion Detection[3] US	XR
T-C-C-1	306	I	10	14	22	X	X
T-C-C-2	341	I	12	15	22	X	X
T-C-C-3	307	I	9	14	25	X	X
T-C-C-4	272	I	10	15	28	X	X
T-Fe-F-2	424	I	3	1	6	uncertain	
T-Fe-F-3a	661(?)	I	2	1	3		
T-Fe-F-3b	661(?)	I	3	3	5		
T-Fe-M-1	296	I	8	17	21	X	X
T-Fe-M-2	353	I	10	8	16	X	X
T-Fe-M-3	389	I	9	11	14	X	X
T-Fe-M-4	337	I	10	15	13	X	X
T-Fe-C-1	205	I	11	20	40	X	X
T-Fe-C-2	319	I	8	34	20	X	X
T-Fe-C-3	242	I	10	33	30	X	X
T-Fe-C-4	212	I	7	34	29	X	X
T-Si-F-1	522	I	13	3	8	X	
T-Si-F-2	550	I	13	3	11	X	
T-Si-F-4	379	I	15	7	17	X	
T-Si-M-1	363	I	1	4	4		
T-Si-M-2	550	I	14	3	10	X	
T-Si-M-3	521	I	11	2	4	X	
T-Si-M-4a	331(?)	I	1	2	7	uncertain	
T-Si-M-4b	331(?)	I	0	7	4		
T-Si-C-1	305	I	8	7	30	X	X
T-Si-C-2	117	I	7	7	25	X	X
T-Si-C-3	296	I	9	5	25	X	X
T-Si-C-4	343	I	10	6	24	X	X
T-WC-F-1	547	I	6	1	6	uncertain	
T-WC-F-2	675	I	1	1	1		
T-WC-F-3	461	I	0	3	4		
T-WC-F-4	619	I	17	4	12	uncertain	
T-WC-M-1	426	I	18	8	10	X	
T-WC-M-2	585	I	0	2	12	X	
T-WC-M-3	466	I	6	8	13	X	X
T-WC-M-4	380	I	0	3	15	X	
T-WC-C-1	478	I	0	5	12	X	
T-WC-C-2	621	I	14	3	8	X	
T-WC-C-3	494	I	10	20	19	X	X

[1] I-inclusion, S-tensile surface microcrack, E-edge microcrack
[2] Dimensions X, Y, and Z defined in Figure 25
[3] An X indicates the inclusion was detected by ultrasonics (US) or radiography (XR)
[4] NA - not applicable

TABLE 8

Modulus of Rupture, optical fractographic and inclusion detectibility data for SiC bend bars broken at room temperature.

Specimen	σ MOR (MN/m^2)	Fracture Origin Location[1]	Inclusion Dimensions[2] (0.001")			Inclusion Detection[3]	
			X	Y	Z	US	XR
1-C-M-1	246	I	0	5	10	X	
1-C-M-2	486	S		NA[4]		NA	
1-C-M-3	283	I	6	10	11	X	
1-C-C-1	134	I	11	14	27	X	X
1-C-C-2	248	I	16	12	21	X	X
1-C-C-4	250	I	0	5	10	X	
1-Fe-F-2	332	I	0	2	6	X	
1-Fe-M-3	283	I	4	7	12	X	
1-Fe-C-1	243	I	0	15	36	X	
1-Fe-C-2	384	S		NA		NA	
1-Fe-C-3	360	E		NA		NA	
1-Si-M-1	342	I	0	6	8		
1-Si-M-3	490	S		NA		NA	
1-Si-M-4	497	E		NA		NA	
1-Si-C-1	323	I	5	18	18	X	
1-Si-C-2	308	I	6	14	18	X	
2-C-F-2	426	I	20	4	6	X	
2-C-M-3	185	I	0	5	8	X	
2-C-M-4	423	S		NA		NA	
2-C-C-1	184	I	27	14	26	X	X
2-C-C-2	209	I	28	14	32	X	X
2-C-C-3	332	I	29	15	23	X	X
2-Fe-C-3	330	S		NA		NA	

[1] I-inclusion, S-tensile surface microcrack, E-edge microcrack
[2] Dimensions X, Y and Z defined in Figure 25
[3] An X indicates the inclusion was detected by ultrasonics (US) or radiography (XR)
[4] NA - not applicable

span of 23 mm. Specimens were allowed to equilibrate thermally for about fifteen minutes after their insertion into the furnace and were broken at a crosshead loading rate of 0.51 mm/min. Fracture strengths were calculated from the formula:

Eq. 2

$$\sigma_f = \frac{1.5\ L\ell}{wt^2}$$

where,

σ_f = fracture stress

ℓ = bend span

and the other symbols retain their previous definitions.

Three-point bend test results at 1093°C and 1371°C for the baseline and defect seeded HPSN specimens are given in Tables 9 and 10, respectively. Similarly, high temperature strength data for the baseline and seeded SiC specimens are given in Tables 11 and 12, respectively. Because of the longitudinal stress field gradient in a three-point bend specimen, the seeded specimens for high temperature testing were selected with centrally located inclusions so as to place the inclusion directly beneath the central loading pin of the test fixture.

TABLE 9. THREE-POINT BEND STRENGTH OF UNSEEDED NC-132 HPSN SPECIMENS AT 1093°C and 1371°C.

	Sample #	1093°C MOR (MN/m^2)	1371°C MOR (MN/m^2)
HPSN Billet T			
	1	738	348
	2	723	329
	3	684	334
	4	747	334
	5	735	348
	Average	725	339
	Standard Deviation	25	9
HPSN Billet B			
	1	590	378
	2	715	383
	3	674	388
	4	636	373
	5	776	364
	Average	678	377
	Standard Deviation	71	9

TABLE 10. THREE-POINT BEND STRENGTH OF SEEDED NC-132 HPSN SPECIMENS AT 1093°C and 1371°C

Test Temperature	Sample	MOR (MN/m^2)	Fracture Origin[1]	Inclusion Dimensions[2] (0.001") X	Y	Z
1093°C						
	B-Si-F-1	762	E		NA[3]	
	B-Fe-F-1	346	I	12	10	30
	B-Fe-F-4	572	I	12	2	8
	T-C-F-1	593	E		NA	
	T-C-F-3	660	I	15	3	7
1371°C						
	B-Si-F-4	343	S		NA	
	B-Si-M-3	354	SS		NA	
	B-Fe-F-3	319	I	11	8	11
	B-C-F-3	359	S		NA	
	T-Fe-F-4	311	S		NA	

[1] E - Edge; I - Inclusion; S- Tensile Surface; SS - Side Surface
[2] Dimensions defined in Figure 25
[3] NA - Not Applicable

TABLE 11. THREE-POINT BEND STRENGTH OF UNSEEDED NC-435 SiC SPECIMENS AT 1093°C and 1371°C

	Sample #	1093°C MOR (MN/m^2)	1371°C MOR (MN/m^2)
SiC Billet 1			
	1	494	344
	2	491	342
	3	491	328
	4	438	325
	5	467	335
	Average	476	335
	Standard Deviation	24	9
SiC Billet 2			
	1	434	335
	2	518	301
	3	414	366
	4	402	308
	5	506	---
	Average	455	328
	Standard Deviation	53	29

TABLE 12. THREE-POINT BEND STRENGTH OF SEEDED NC-435 SiC SPECIMENS AT 1093°C and 1371°C.

Test Temperature	Sample	MOR (MN/m^2)	Fracture Origin[1]	Inclusion Dimensions[2] (0.001") X	Y	Z
1093°C						
	1-Si-M-2	455	S		NA[3]	
	1-C-M-4	332	I	5	5	5
	1-C-F-2	445	S		NA	
	1-Fe-M-4	372	I	13	7	12
	1-Fe-F-4	312	I	0	6	6
1371°C						
	2-Fe-F-3	272	S		NA	
	2-C-M-1	200	I	7	7	6
	2-C-F-4	246	S		NA	
	2-Fe-M-1	301	S		NA	

[1] I - Inclusion; S - Surface
[2] Dimension defined in Figure 25
[3] NA - Not Applicable

A few of the fracture strengths in the tables are followed by a question mark. These values are of somewhat questionable validity since the corresponding bend specimens broke into three large fragments, as exemplified by sample T-Fe-F-3 in Figure 24. The length of the central fragment corresponds closely to the inner span spacing and, therefore, suggests that "wedging" stresses beneath the loading points contributed to the selection of the fracture initiation site. Examination of the end fragments revealed the existance of small, internal inclusions on each piece.

D. MICROSCOPY

1. Optical Microscopy

All of the broken seeded specimens were examined by optical microscopy to characterize the fracture surface with respect to the nature and location of the fracture origins. Origins were classified as either inclusion or surface microcrack initiated types of failures. Locations were classified as either internal (always of the inclusion type), tensile surface (of either type) or bar edge (always of the microcrack type). Although both

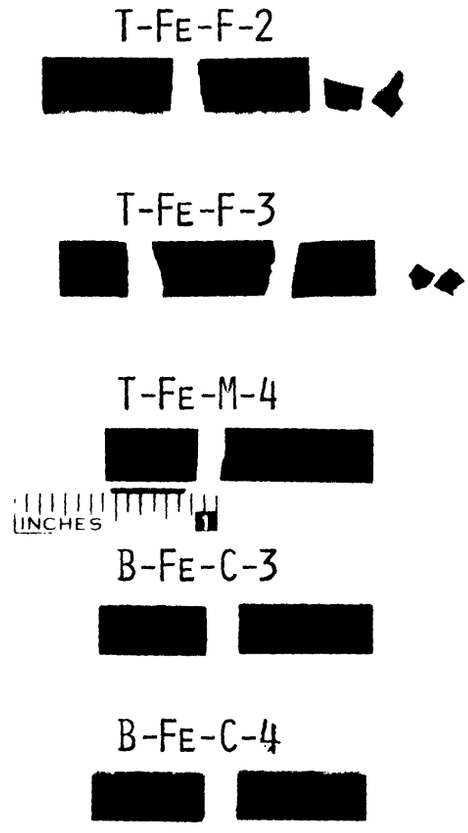

Figure 24. Bend bar fragments after strength testing.

types of surface microcracks result from finishing operations, the severity of edge microcracks is usually greater, which causes edge initiated failures to occur at a relatively lower stress. For a small number of the fractures, optical microscopy was insufficient to determine whether the initiation side was a small inclusion near the face or a surface microcrack. A scanning electron microscope was used to resolve these uncertain cases.

A reticle was used to measure the dimensions of the fracture initiating inclusions on the fracture face. These measurements were made at 30X magnification to the nearest 0.001 inch. As illustrated in Figure 25, the dimensions consisted of the distance, x, from the bar face to the inclusion and the thickness, y, and width, z, of the exposed defect. The nature of the fracture origin and, if the origin was an inclusion, the inclusion dimensions are given in the appropriate table (Table 7, 8, 10 or 12) for each seeded bend bar.

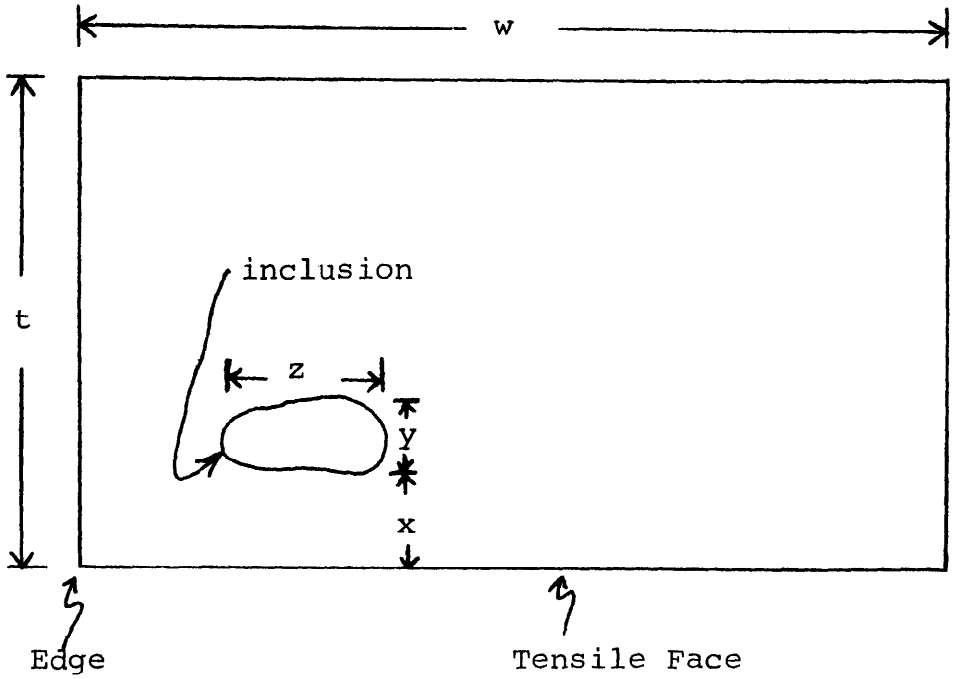

t = bar thickness

w = bar width

x = inclusion depth from tensile face

y = inclusion thickness

z = inclusion width

Figure 25. Schematic of inclusion geometry on fracture face.

The three dimensional position of the inclusions exposed during room temperature bend testing was compared with the three dimensional coordinates (C-scan map plus depth indication) of the defects previously detected by nondestructive means in the bar blanks. The congruencies are noted in Tables 7 and 8. A substantial number of the smaller defects were not detected by either inspection method.

The distance of the inclusion from the tensile face, x, was used to compute the applied bend stress at the bottom of the defect, σ_d, at the time of fracture. Assuming a linear bend stress gradient,

$$\sigma_d = \sigma_{MOR} (1 - 2x/t) \qquad \text{Eq. 3}$$

where,

σ_{MOR} = outer fiber stress at fracture from Eq. 1

t = specimen thickness

The use of this information, listed in Tables 13 and 14, will be discussed in a future section.

During the C-scan examination of the silicon carbide material, ultrasonic reflections over relatively large areas frequently obscured the detection of seeded defects. The cause of these ultrasonic signals was sought in the microstructure of the material. A mounted and polished cross section of a sample which produced widespread reflections is shown in Figure 26. The roughly horizontal dark bands, which extend across the width of the sample, represent a microstructural inhomogeneity resulting from a non-uniform infiltration and reaction of silicon during material manufacture. The root cause of this inhomogeneity is believed to have been material cracking prior to or during the silicon infiltration. Although the crack becomes filled during processing, the material property discontinuity is sufficient to provide radiographic contrast and function as a reflector of elastic waves.

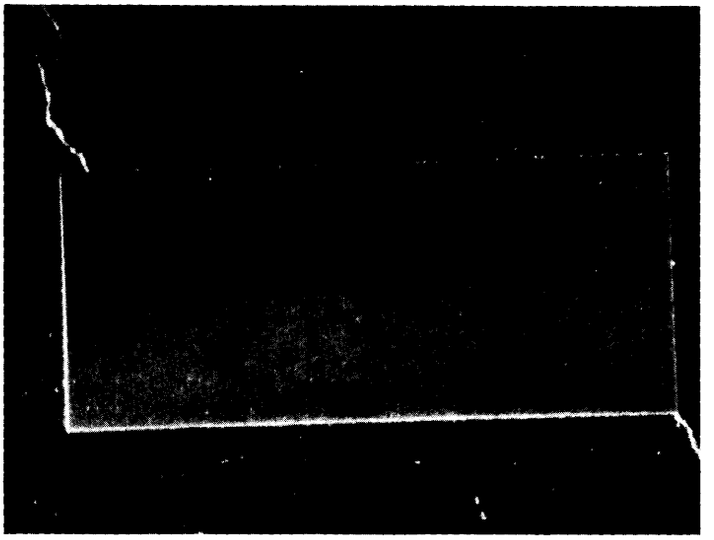

Figure 26. Microstructural inhomogeneity bands in the silicon carbide material responsible for radiographic striations and wide area ultrasonic reflections, 10X.

2. Scanning Electron Microscopy and Electron Probe

Since the nondestructively detected defects did not perfectly match the seeding plans and because some of the fracture initiating inclusions were not detected, the identities of most of the target inclusions were not known prior to strength testing. Therefore, broken specimens were examined with a scanning electron microscope (SEM) and an energy dispersive microprobe in order to characterize better the fracture origins. To this end, approximately forty origins were so examined, with the emphasis on the smaller inclusions, the more unusual fractures, and the room temperature fractures. The ultimate results of this characterization was to permit the compilation of Tables 13 and 14 in which the fracture initiating inclusions are correlated with the seeded inclusions. Only the basic technique and conclusions of this characterization are covered in this section. Additional details and photographs are given in the Appendix.

An example of an inclusion initiated fracture in HPSN is shown in Figure 27. The electron microprobe detected the presence of relatively large quantities of tungsten and cobalt within the inclusion, thereby permitting positive identification of a seeded tungsten carbide particle. As seen in Tables 7 and 8, microcrack initiated failures were rare. An example of this type of failure is shown in Figure 28. With the aid of stereo photomicrographs of the fracture origin, the depth of the initial defect could be determined from the fractographic markings at its arrest position.

Although finding the inclusion in the SEM presented no serious difficulty, the identification of the chemical identity of the defect was not always straightforward. The problem was more acute with the smaller inclusions, especially the silicon and carbon type inclusions, because of limitations of the microprobe. All seeded inclusion types tend to chemically react with the matrix materials during material processing, for example, carbon particles tend to convert to silicon carbide, iron particles tend to form iron silicide, tungsten carbide particles tend to convert to tungsten silicide and silicon-silicon nitride interactions are seen. As a result, silicon is always detected by the microprobe within inclusions. No characteristic elements are detected by the probe from carbon inclusions, since the energy dispersive probe is insensitive to elements of atomic number less than eleven, or small silicon inclusions, since it is uncertain whether the silicon signal arises from the inclusion or the matrix material. Fortunately, the morphology of the defect assists in its chemical identification. For example, the characteristic visual appearance of the graphite lamella and the formation of a dense silicon carbide shell around carbon particles permit a positive identification. Familiarity with known larger inclusions thus assisted the identification of smaller inclusions for which the probe was of minor assistance. Of course, the presence in substantial amounts, of elements not

TABLE 13

Applied bend stress at position of fracture initiating inclusion and inclusion identity for room temperature fractures in HPSN

Specimen	σ_d[1] (MN/m^2)	Microprobe Analysis	Type of Inclusion[2]
B-C-F-2	447	Si	U
B-C-F-4	395	--	U
B-C-M-2	618	Si	C(?)
B-C-M-3	349	Si	C
B-C-M-4	526	--	U
B-C-C-1	477	Si	U
B-C-C-3	548	Si	U
B-C-C-4a	697(?)	--	C
B-C-C-4b	697(?)	Si,Fe,K,Cl	O
B-Fe-F-2	398	--	Fe(?)
B-Fe-M-1	323	Si, Fe	Fe
B-Fe-M-2	383	--	Fe
B-Fe-M-3	334	--	Fe
B-Fe-M-4	355	--	Fe
B-Fe-C-2	210	--	Fe
B-Fe-C-3	217	--	Fe
B-Fe-C-4	268	Si, Fe	Fe
B-Si-F-3	401	Si	Si(?)
B-Si-M-1	362	Si	Si
B-Si-M-2	375	--	Si
B-Si-C-1	264	--	Si
B-Si-C-2	243	--	Si
B-Si-C-3	283	--	Si
B-Si-C-4	272	--	Si
B-WC-F-1	525	--	WC(?)
B-WC-F-2	466	Si,W,Co	WC
B-WC-F-3	515	--	WC(?)
B-WC-M-1	416	--	WC
B-WC-M-2	475	Si,W,Co,Al	WC
B-WC-M-4	371	Si,Mg,W,Sn	O
B-WC-C-2	Invalid Break	Si,W,Sn	O
B-WC-C-3	529	--	WC
B-WC-C-4	Invalid Break	Si,Mg,Sn,K	O
T-C-F-4	537	Si, Fe	Fe
T-C-M-1	311	--	C
T-C-M-2	293	--	C
T-C-M-3	406	Si, Fe	Fe
T-C-M-4	264	--	C
T-C-C-1	257	--	C
T-C-C-2	276	--	C
T-C-C-3	263	--	C
T-C-C-4	228	--	C

Continued

TABLE 13 (continued)

Specimen	σ_d[1] (MN/m^2)	Microprobe Analysis	Type of Inclusion[2]
T-Fe-F-2	404	Si, Mg	O
T-Fe-F-3a	629(?)	Si, Fe	Fe
T-Fe-F-3b	629(?)	Si, Fe	Fe
T-Fe-M-1	258	--	Fe
T-Fe-M-2	296	--	Fe
T-Fe-M-3	333	--	Fe
T-Fe-M-4	283	Si, Fe	Fe
T-Fe-C-1	173	--	Fe
T-Fe-C-2	281	--	Fe
T-Fe-C-3	206	--	Fe
T-Fe-C-4	190	--	Fe
T-Si-F-1	410	--	U
T-Si-F-2	432	--	U
T-Si-F-4	284	--	U
T-Si-M-1	357	Si	Si
T-Si-M-2	424	--	Si
T-Si-M-3	434	--	Si
T-Si-M-4a	326(?)	Si	Si
T-Si-M-4b	326(?)	Si, Mg	O
T-Si-C-1	265	--	Si
T-Si-C-2	103	--	Si
T-Si-C-3	252	--	Si
T-Si-C-4	288	--	Si
T-WC-F-1	490	--	U
T-WC-F-2	675	Si,P,Fe	O
T-WC-F-3	457	Si,W,Sn	O
T-WC-F-4	444	Si, Mg	O
T-WC-M-1	326	Si, Al	O
T-WC-M-2	585	--	U
T-WC-M-3	419	--	WC
T-WC-M-4	380	--	U
T-WC-C-1	478	Si, W	O
T-WC-C-2	487	--	U
T-WC-C-3	418	--	WC

[1] From Eq. 3
[2] Identity in terms of seeded particles
U means identity of inclusion is Uncertain
O means inclusion was not intentionally seeded

TABLE 14. APPLIED BEND STRESS AT POSITION OF FRACTURE INITIATING INCLUSION AND INCLUSION IDENTITY FOR ROOM TEMPERATURE FRACTURES IN SiC

Specimen	σ_d[1] (MN/m^2)	Microprobe Analysis	Type of Inclusion[2]
1-C-M-1	246	---	C
1-C-M-3	259	Si	C
1-C-C-1	113	---	C
1-C-C-2	192	---	C
1-C-C-4	250	---	C
1-Fe-F-2	332	Si, Sn	Si
1-Fe-M-3	267	Si	Si
1-Fe-C-1	243	Si	Si
1-Si-M-1	342	Si	Si
1-Si-C-1	300	Si, P	Si
1-Si-C-2	282	---	Si
2-C-F-2	306	Si, Fe	C
2-C-M-3	185	Si	SiC
2-C-C-1	114	---	C
2-C-C-2	126	---	C
2-C-C-3	196	---	C

[1] From Eq. 3
[2] Identity in terms of seeded inclusion type

normally associated with the seeded silicon or carbon particles signified that the inclusions containing these elements did not originate from seeded silicon or carbon particles. Many contaminant inclusions, not intentionally seeded, were thus identified by the microprobe.

Aside from direct defect identification by the SEM/probe, many of the larger inclusions that were not so intensively examined were indirectly identified by a combination of methods including optical appearance, size and seeded defect location. The direct and indirect methods enabled most of the defects to be chemically identified with the unidentified particles concentrated in the smaller sizes. Five fracture initiating inclusions in HPSN were tentatively identified by either incompletely conclusive fractography or by a self-consistent agreement between seeded defect type and nondestructive evaluation. Examples of the latter method are samples B-WC-F-1 and B-WC-F-3 whose inclusions were assumed to be WC particles because the small inclusions were located in bars intended to contain small WC particles and the inclusions were detected by radiography, as is possible for small inclusions only if the x-ray absorption coefficient is sufficiently large.

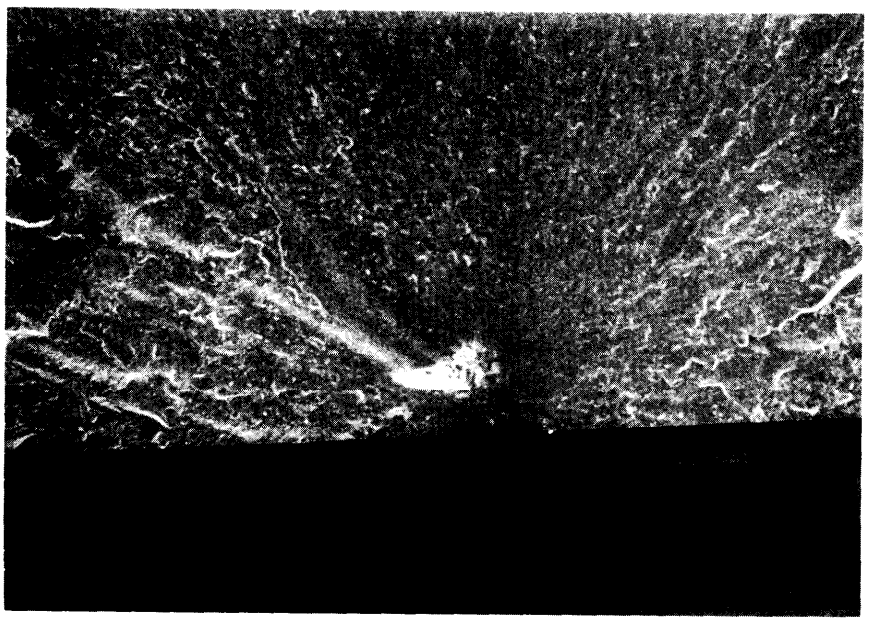

(A) View of inclusion at fracture origin, 50X, SEM

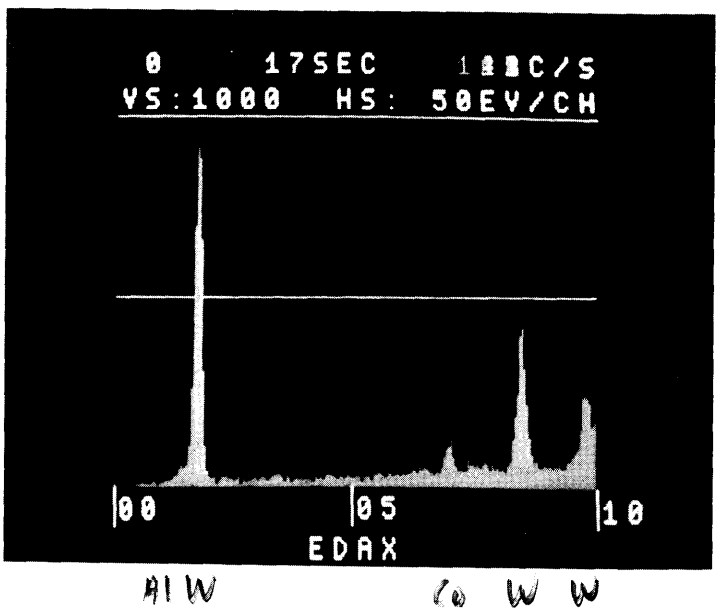

(B) Photograph of microprobe display monitor, indicating presence of W, Co and Al.

Figure 27. Results of SEM (A) and probe examination (B) of inclusion in sample B-WC-M-2, which identify it as a seeded WC particle.

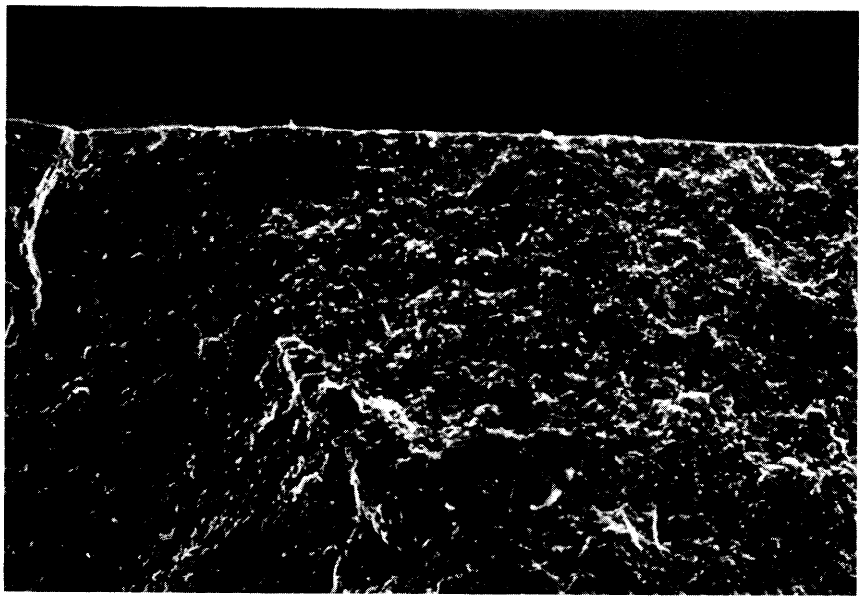

(A) SEM, 200X

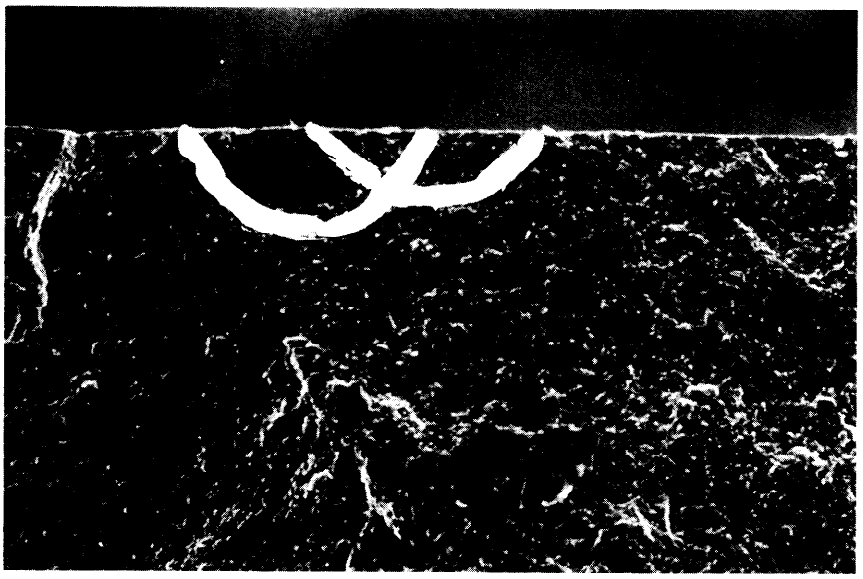

(B) SEM, 200X, with crack arrest points outlined

Figure 28. Surface microcrack initiated failure origin in sample 1-Fe-C-2

The chemical characterizations of the inclusions are listed in Tables 13 and 14 for the HPSN and SiC material fractures, respectively. Elements that were detected by the probe are given on a qualitative basis only and many of the elements, e.g. Al, Mg, Sn, K, are frequently present only in small amounts. Noteworthy is the existence of unintentionally seeded defects which function as fracture origins, especially in the tungsten carbide series of samples in the bottom HPSN billet. A "cloud" of these defects had been nondestructively detected in this region of the billet. Also, iron inclusions are not present in the SiC #1 billet, and it is concluded that a seeding error was made.

III RESULTS AND DISCUSSION

An inspection of Tables 7 and 8 shows that inclusions initiated most of the fractures in the seeded room-temperature bend test specimens of NC-132 HPSN and NC-435 SiC. A comparison of the unseeded bar strengths with seeded bar strengths (Tables 5 and 7 for HPSN, Tables 6 and 8 for the SiC) shows that the bend strengths of the defect seeded bars are, in general, less than the unseeded bar strengths. This information is reflected in the ranges of bend strengths for the corresponding seeded and unseeded materials, as shown in Table 15.

The effect of temperature on bend strength for the two ceramic materials is summarized in Table 15. The strength data were drawn from Tables 5 through 12. It is noted that the 25°C strengths are not exactly comparable to the higher temperature strengths as the former were measured in four-point bending and the latter in three-point bending. Although this difference is not critical to the current discussion, the change in bend fixture use may be compensated for by increasing the four-point values by about 15%, the approximate difference in strength when a given material is tested in both bending modes at room temperature.

For the unseeded HPSN material, strength is little changed between 25°C and 1093°C, which indicates that material failure is of a brittle nature at 1093°C. Of the five seeded HPSN specimens tested at 1093°C, three failed at inclusions and two from edge cracks.

The strength of the unseeded NC-435 SiC material at 1093°C is greater than its 25°C strength. The difference appears to be larger than one can expect from a change in bend test fixture alone. The increase in strength is believed to be due to the increased dislocational plasticity of the silicon phase above 600°C which permits stress concentrations to be partially relieved and increases the fracture energy. Of the five seeded SiC specimens tested at 1093°C, three broke at inclusions and two from surface origins.

TABLE 15

	25°C[1]	1093°C[2]	1371°C[2]
NC-132 HPSN			
Billet T, Unseeded	732;604-894;12	725;684-738;5	339;329-348;5
Billet B, Unseeded	650;517-812;12	678;590-776;5	377;364-388;5
Billet T, Seeded	403*†;117-675;39	593, 660*	311
Billet B, Seeded	460*†;238-639;29	346*,572*,762	319*,343, 354, 359
NC-435 SiC			
Billet #1 Unseeded	388;316-519;8	476;438-494;5	335;325-344;5
Billet #2 Unseeded	305;264-361;8	455;402-518;5	328;301-366;4
Billet #1 Seeded	272;134-342;11	312*,332*,372*, 445, 455	-
Billet #2 Seeded	267;184-426;5	-	200*,246,272, 301

[1]Four-point bend fixture

[2]Three-point bend fixture

*Inclusion assisted fracture

†Average for all types of inclusions

Influence of Test Temperature on Strength (MN/m^2) of Seeded and Unseeded Ceramic Materials. Mean strength, strength range, and number of tests, respectively, are given for each condition except for seeded high temperature strengths where individual bar strengths are given.

Both materials significantly decrease in strength between 1093°C and 1371°C. This decrease is accompanied by a decrease in inclusion initiated failure and an increase in surface initiated failure. Only one instance per material of inclusion related initiation was found at 1371°C. The lessened importance of inclusions for generating failures in HPSN is due to the onset of a high temperature failure mechanism involving grain boundary softening and sliding. This mechanism causes slow crack growth during the time of the bend test. An example of the slow crack growth mechanism, operating in concert with the stress field around an inclusion, is shown in Figure A-9B of the Appendix. The decrease in strength of the NC-435 SiC material at 1371°C is due to the inability of the almost molten silicon (melting point = 1415°C) to support a load. In contrast to the rapidly weakening HPSN material, the NC-435 SiC material has a strength at 1371°C which is approximately its room temperature value.

Many of the fracture initiating defects, especially in the larger sizes, were detected by either radiography or ultrasonic C-scans. As evident in the C-scans and radiographs for the billets and also in the defect tabulations for the rough-cut bars (see Appendix) more internal defects were detected by ultrasonics than by radiography. In addition, more of the defects which precipitated fractures were detected by ultrasonics than by radiography, as may be seen from Tables 7 and 8. Although not apparent in the listings of Tables 7 and 8, radiography occasionally would indicate a defect which was not detected by the ultrasonic method. Since the sensitivity of various NDE methods depend upon different physical principles and give different types of information, a prudent approach to evaluating the quality of ceramic materials would be to use multiple NDE methods. Under this philosophy, the different NDE methods complement each other.

Table 16 shows the relative ability of the NDE methods to detect seeded defects as a function of defect type and size. The table was constructed by combining the results of C-scans and radiographs for the billets, from which many defect sizes and types could be determined by inspection, with the results of the scanning electron microscope and microprobe examination. Defect sizes are expressed in terms of the as-seeded size classifications of fine, medium and coarse. Defect shapes frequently changed significantly during billet manufacture from roughly equiaxed initial particle shapes to flattened geometries, as evidenced by the measured dimensions of fracture exposed inclusions. It is seen that ultrasonics was more successful in detecting smaller low density particles (Si and C) in both NC-132 HPSN and NC-435 SiC. In addition to the intentionally seeded defects, the ultrasonic method detected the unintentional semi-porous type of defect in HPSN. On the other hand, it is known that radiography is capable of resolving dense inclusions down to at least 0.025 mm in size if magnification is used to read the radiographs. Strongly

TABLE 16

Matrix Material;Defect Type	Nominal Defect Size		
	Fine	Medium	Coarse
NC-132 HPSN;Fe	X, U	X, U	X, U
" " ;WC	X, U	X, U	X, U
" " ;Si	U	U	X, U
" " ;C	-	U	X, U
NC-435 SiC;C	U	U	X, U
" " ;Si	-	U	U

Relative effectiveness of detection of seeded defect inclusions by ultrasonics and radiography.

X = radiographic detection
U = ultrasonic detection

x-ray absorbing particles on the order of 0.08 mm in size were observed on the HPSN radiographs and these particles are believed to be tungsten carbide inclusions.

Of the NC-132 HPSN fracture origins which were investigated with the SEM and microprobe, twelve fracture initiating inclusions were found which were not detected by either nondestructive test method. Four of the twelve were iron inclusions, four were of the semi-porous type, one was a silicon inclusion and three were of uncertain identification. The four iron inclusions were the four smallest iron inclusions exposed on the fracture surfaces and the four semi-porous inclusions were among the smallest of this type that were found. The exposed dimensions (thickness by width, in micrometers) of the iron inclusions were 25 x 25, 25 x 75, 75 x 100 and 75 x 125. The dimensions of the semi-porous inclusions were 25 x 25, 25 x 25, 75 x 100 and 175 x 100 micrometers. Although defect shape and orientation strongly influence defect detectability and although iron and semi-porous defects of a similar size may have been among the detected defects which did not function as fracture origins, the above results show that the nondestructive methods that were used did not always detect iron and semi-porous inclusions in the smaller size range indicated.

In Figures 29A, B and C, the fracture stress (from Tables 13 and 14) at the defect is plotted versus the thickness dimension (from Tables 7 and 8) of the exposed defect. The solid lines represent a least squares fit to the data. Despite the obvious scatter, it is seen that the larger the size of a given type of inclusion, the lower the stress required to initiate fracture. An exception to this size-strength relationship are tungsten carbide inclusions in HPSN, for which the strength is invariant with size. The fracture stress at the inclusion is the modulus of rupture value which would have been observed had the inclusion been located at the most highly stressed region of the bend specimen, that is at the tensile surface. As previously noted, inclusion initiated fracture stresses are significantly lower than the unseeded modulus of rupture values, especially for the HPSN material.

For a spherical cavity within a matrix, the stress concentration factor associated with the cavity is almost exactly two and is independent of the size of the cavity. The observed size-strength relationship shows that most real inclusions do not behave mechanically like a spherical cavity. Among the possible explanations for the observed size effect of real inclusions are size related changes in the extent or magnitude of a) microcrack formation at inclusions b) interfacial stress and c) inclusion-matrix chemical interactions which affect matrix properties plus the effects of particle shape and orientation with respect to the applied stress field. Regarding particle shape, many of the inclusions have a longer width than thickness such that the major plane of the inclusion is perpendicular to the specimen thickness, which was the pressing direction during billet manufacture. This orientation is favored by both

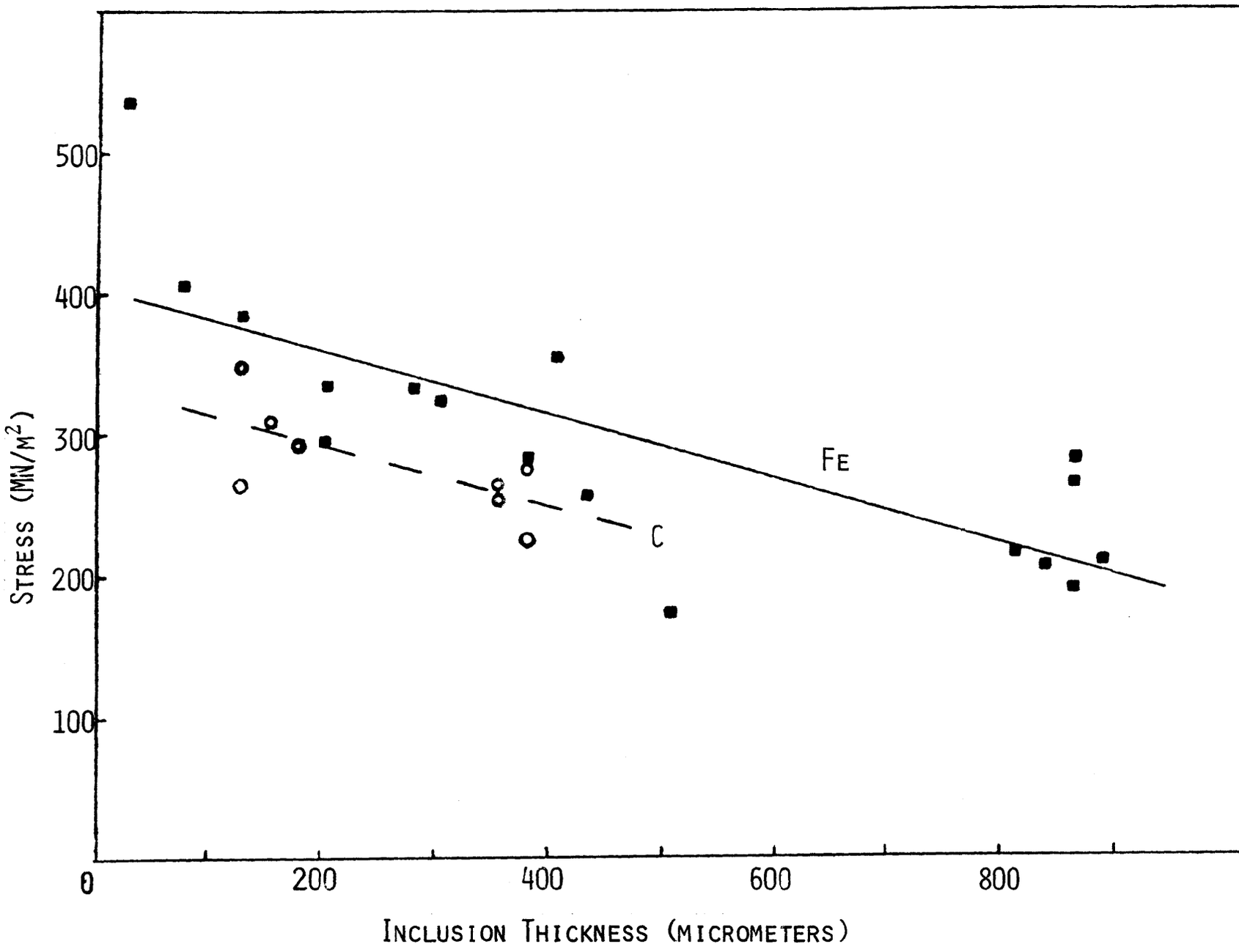

Figure 29A - Effect of inclusion size on fracture stress at inclusion. Iron and carbon inclusions in NC-132 HPSN.

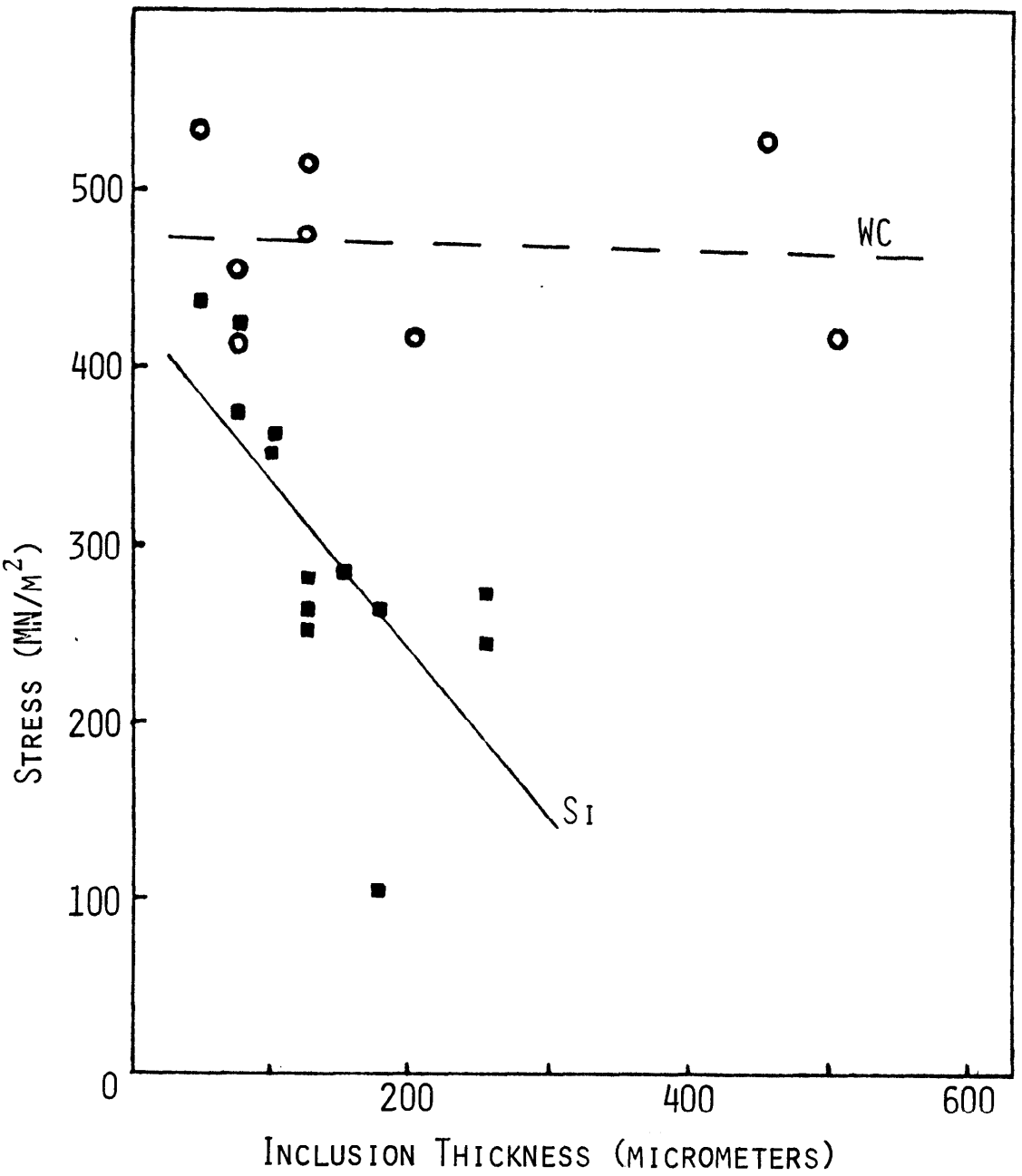

Figure 29B - Effect of inclusion size on fracture stress at inclusion. Tungsten carbide and silicon inclusions in NC-132 HPSN.

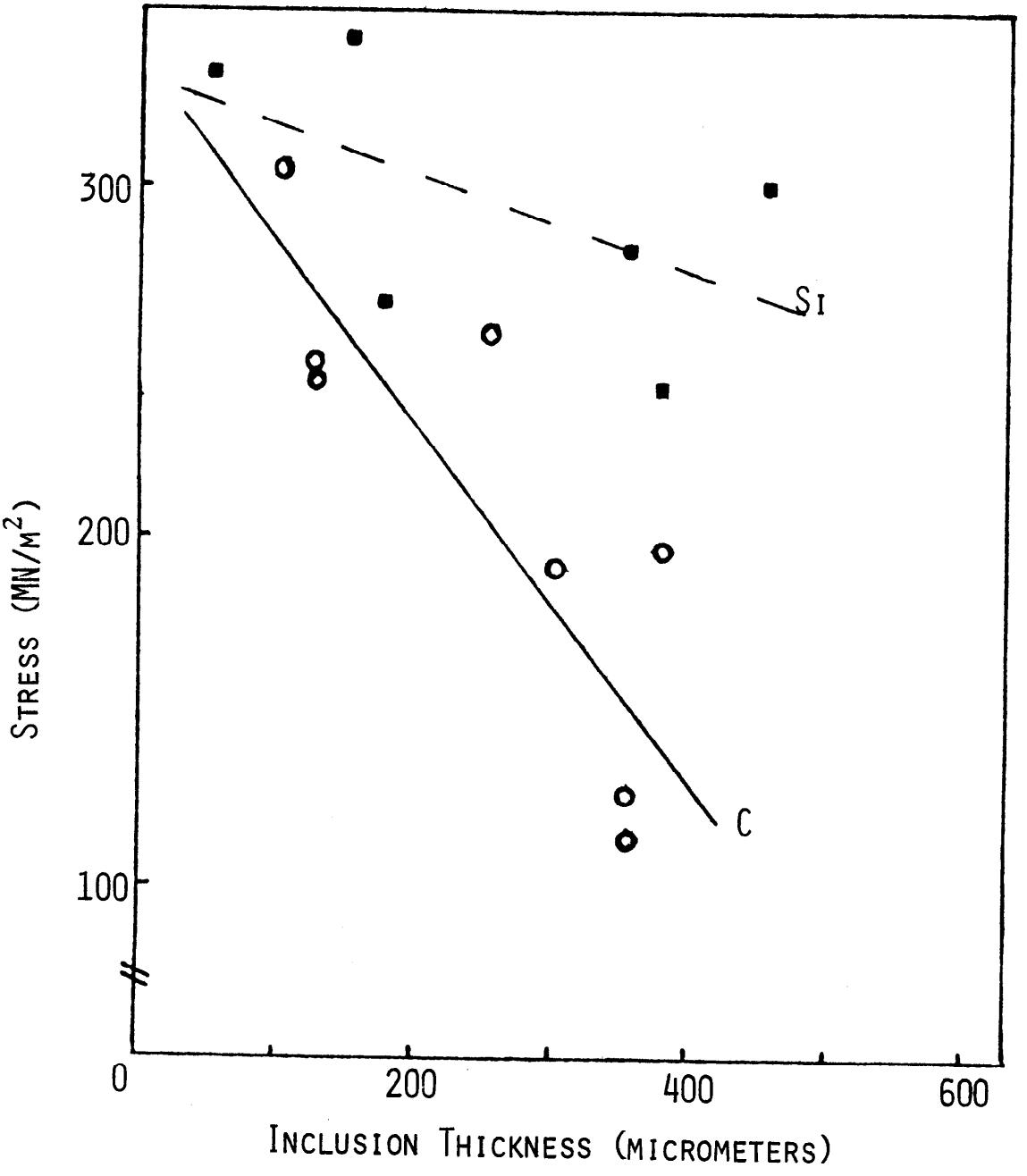

Figure 29C - Effect of inclusion size on fracture stress at inclusion. Silicon and carbon inclusions in NC-435 SiC.

rigid body particle rotation and particle deformation under the pressing stresses of billet manufacture. The flattened orientation is most pronounced for the silicon inclusions in HPSN, which are molten at the hot-pressing temperature. At the other extreme of particle shape are the largest tungsten carbide inclusions, only two of which were observed to initiate fracture. The larger particles of this type are almost perfectly spherical, in contrast to some of the smaller carbide particles, such as the one shown in Figure A-4. Other bend bars that contained large spherical tungsten carbide particles failed at origins other than the carbide inclusions. Thus a contributing reason for the near zero slope of the size-strength relationship for the tungsten carbide particles may be a smaller stress concentration associated with the larger particles. With regard to inclusion-matrix chemical interactions, most defect types exhibit interaction as discussed in the Appendix. Examples are silicon diffusion into inclusions in HPSN and silicon carbide shell formation about carbon inclusions in NC-435 SiC.

When comparing the relative effects of particular inclusion types upon material strength, consideration must be given to inclusion size, shape and orientation. An extensive characterization of inclusion shapes and orientations is beyond the scope of this report. However, the inclusion shapes do have some commonality in that many exposed cross-sections approximate ellipses and, as has been discussed, the particles tend to orient themselves to the pressing direction. Although Figures 29A, B and C explicity refer to only the size of the defects, a degree of commonality with respect to particle shape and orientation is implicity contained in the data. The different slopes and levels of the trendlines for inclusions of different types strongly suggest that different strength levels may be expected for different types of inclusions which are otherwise identical with respect to size, shape, and orientation. This statement in no way implies that defect shape and orientation do not affect fracture strength.

The NDE methods that were used in the study, and especially the ultrasonic method, are capable of detecting with high reliability the type of large defect contamination which can accidently occur during material processing. By its nature, this type of contamination is less common, occurs randomly and cannot be predicted by a distribution function. Inspection of ceramic materials for this type of defect is an important function of NDE and one which the currently used methods are capable of handling.

Since particles in the size range of 100 micrometers and less do adversely affect material strength, and the lower limit of reliable nondestructive detection was not clearly established during this investigation, further work is needed. Additional effort should be devoted to destructive evaluation of the smallest particles currently detectable by NDE and also to the development of improved small particle detection. One approach to obtain greater size-sensitivity is to use higher ultrasonic frequencies.

APPENDIX

Individual C-Scans of Rough-Cut Bars and Electron Microscopy of Defects in Corresponding Bars

This section contains examples of C-scans of rough-cut bars and the subsequent microscopic analyses of defects contained within the corresponding bend bars. The latter includes photomicrographs of the fracture initiating defect, and, where appropriate, a photograph of the display of the energy dispersive microprobe. Space considerations prohibit a complete listing of all of the individual C-scans and photomicrographs; however, the data shown are representative of the remainder.

The photomicrographs are oriented such that the thickness direction of the bend bar corresponds to the vertical direction of the page. Unless indicated otherwise, the fractures were made at toom temperature. The C-scans were made from both the front and back sides of the bars. In addition to the two dimensional displays of the defect positions (in plane of paper), the depth (in direction perpendicular to plane of paper) of the defects are tabulated, as determined by the method of detection. Depths are measured relative to the back surface of the bar. The four place identification code for the bars is explained in Table 4. The following abbreviations are used in the C-scans:

F	-	Front surface view
B	-	Back surface view
DN	-	Defect number
USD	-	Depth of defect as determined by ultrasonics distance measured from back surface (B) in inches.
XRD	-	Depth of defect as determined by radiography, distance measured from back surface (B) in inches.
H	-	Defect density higher than that of matrix.
L	-	Defect density lower than that of matrix.

In the listing of the defects below a C-scan figure, an arrow indicates the defect which was sought as the fracture origin (target defect). Multiple defects were present upon occasion at the same depth within the sample.

Examples of each of the seeded defect types in HPSN are shown in Figures A-1 - A-4. The tungsten carbide defect of Figure A-4 is also shown at lower magnification in Figure 27. Each defect type chemically reacts with the matrix material so that the microprobe detects silicon within each defect type. Iron inclusions (Figure A-2) and tungsten carbide inclusions (Figure A-4) are readily identified by the probe. Silicon and carbon inclusions usually emit only a silicon probe signal, as illustrated in

Figure A-6. For silicon particles, this result is due to the nature of the particle, whereas for carbon particles, the probe is not sensitive to elements of low atomic number. Larger particles of these types may be identified by their characteristic morphology: silicon particles exhibit conchoidal fracture while the lamellar structure of graphite is easily recognized. Carbon inclusions are futher identified by the presence of a surrounding shell of silicon carbide.

Figure A-5 contains C-scans of NC-435 SiC bars previously discussed in the text. The C-scan of Specimen 2-Si-C-3 is an extreme example of the ultrasonic reflections frequently observed in the silicon carbide samples. A polished cross-section of this bar appears in Figure 26. The fracture origin of specimen 1-Fe-C-2 appears in Figure 28. Examples of the two seeded inclusion types, carbon and silicon, found in the silicon carbide bars are shown in Figures A-6 and A-7, respectively.

Figure A-8 shows an iron inclusion at the fracture origin of a HPSN bar that was broken at 1093°C. A similar inclusion initiated the 1371°C HPSN failure in Figure A-9. The corrugated fracture surface between the inclusion and the tensile face in Figure A-9 is characteristic of slow crack growth. Although HPSN becomes much more plastic over the temperature interval between 1093 and 1371°C, Figure A-9 shows that inclusions can still influence strength at the higher temperature. The inclusion was partially molten at the higher test temperature, which was above the eutectic temperature in the Fe-Si system.

Another instance of an inclusion causing fracture at 1371°C is shown in Figure A-10. In this case, the material is NC-435 SiC and the inclusion is carbon. The interior of the inclusion was strongly oxidized after exposure, but the silicon carbide shell remained intact.

A small iron inclusion is shown in Figure A-11. Iron inclusions of this size are present in NC-132 HPSN even without seeding and it is believed this defect was not seeded. Defects of this size were not detected by the nondestructive methods that were used.

Figure A-12 shows an unseeded type of defect which frequently functioned as a fracture origin in the HPSN samples. This type of defect is believed to have been introduced unintentionally into the billets during the seeding operation and is the cause of many of the additional ultrasonic defect indications. This type of defect is porous and not detected by radiography. Although this type of defect frequently contains more tungsten than the matrix, the tungsten concentration is much less than that of a tungsten carbide inclusion as may be seen by comparing the probe displays of Figures A-12 and A-4

The inclusion in Figure A-13 is unusual on several counts. The defect is of the porous type and magnesium, tin and potassium, elements not usually detected in HPSN, were found with the defect. The long axis of the defect is oriented uncharacteristically at a large angle to the hot pressing plane, which may be a contributing reason why this defect caused fracture even though it was located outside the inner bend span.

The fracture origin of the NC-435 SiC specimen shown in Figure A-14 contains a large well-faceted inclusion which was not intentionally seeded. Because of its shape and the detection of only a silicon signal with the probe, the inclusion is believed to be a large grit of silicon carbide which was present as unwanted contamination in the original material mix.

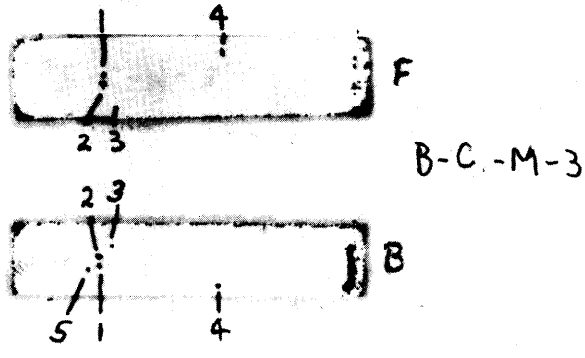

DN	USD	XRD
1	0.110	
2	0.110	
3	0.110	
→ 4	0.119	
5	0.146	

Figure A-1A. C-scan of specimen B-C-M-3

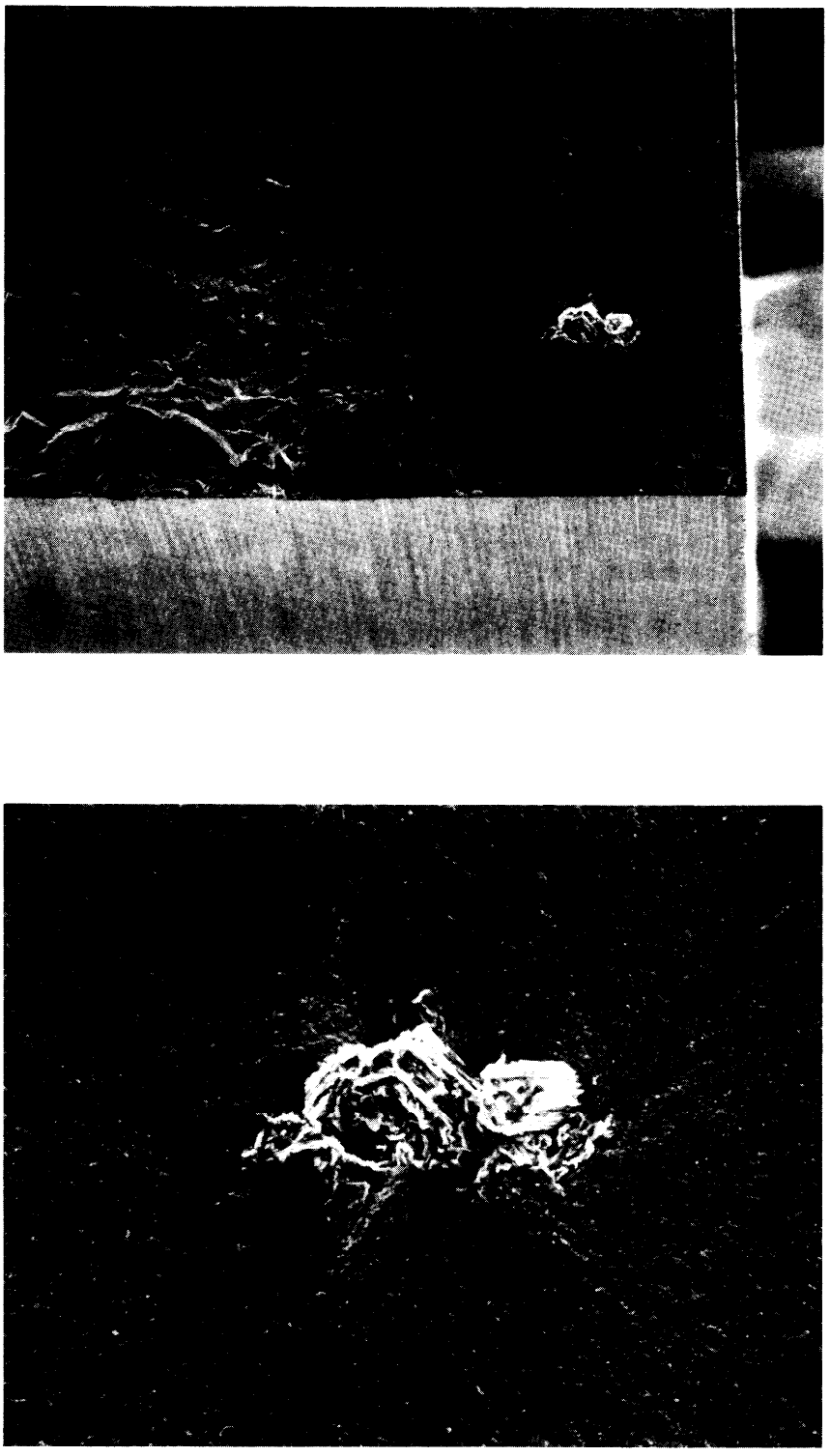

Figure A-1B. Fracture origin (carbon inclusion) in specimen B-C-M-3 at 50X (above) and 200X (below)

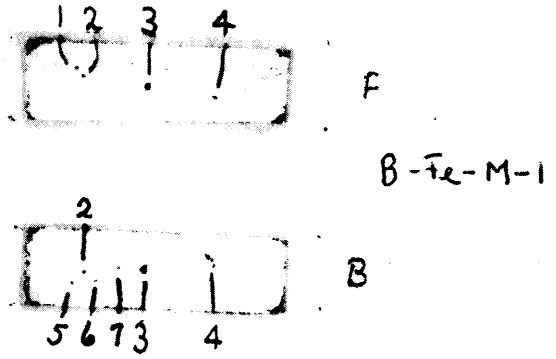

DN	USD	XRD
1	0.109	
2	0.109	
→ 3	0.109	0.105 H
4	0.109	
5	0.127	
6	0.145	
7	0.145	

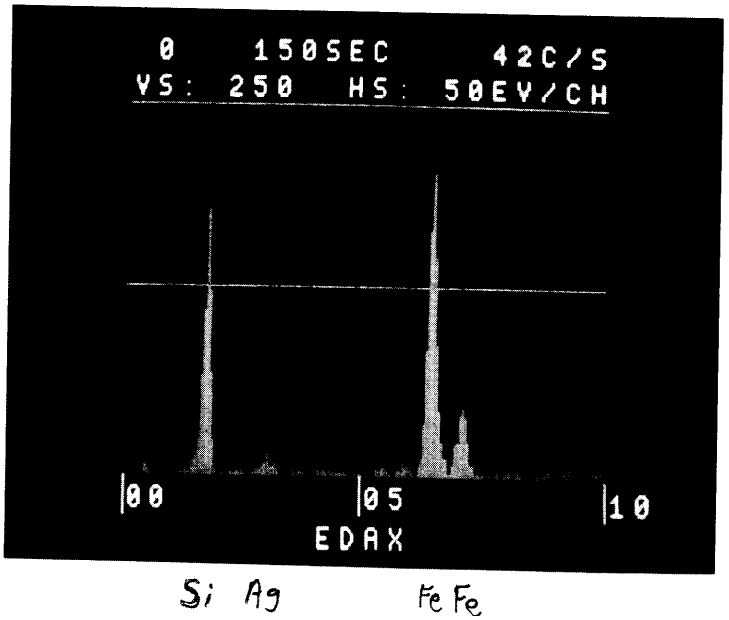

Figure A-2A. C-scan (above) and microprobe display (below) of specimen B-Fe-M-1

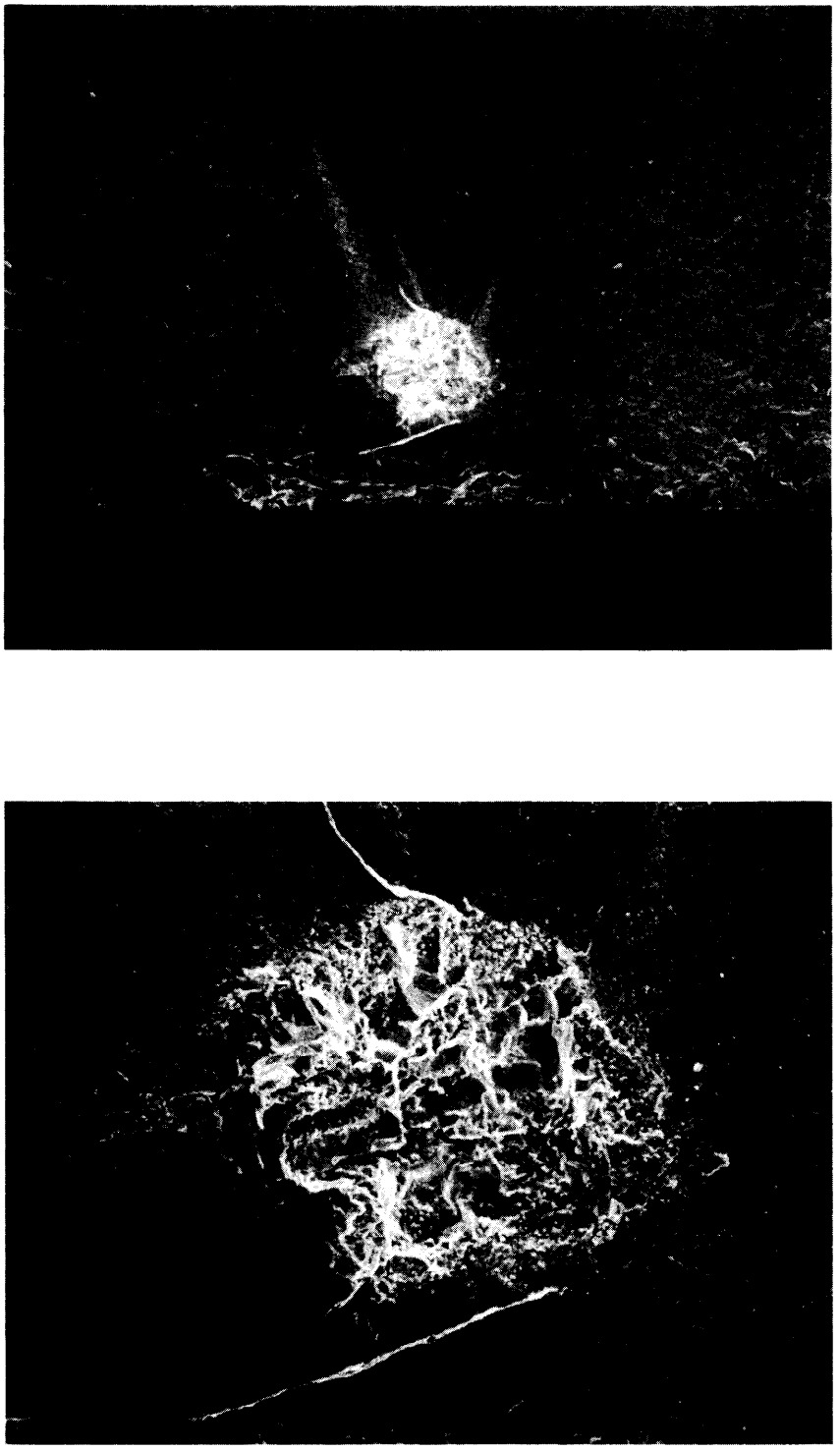

Figure A-2B. Fracture origin (iron inclusion) in specimen B-Fe-M-1 at 50X (above) and 200X (below).

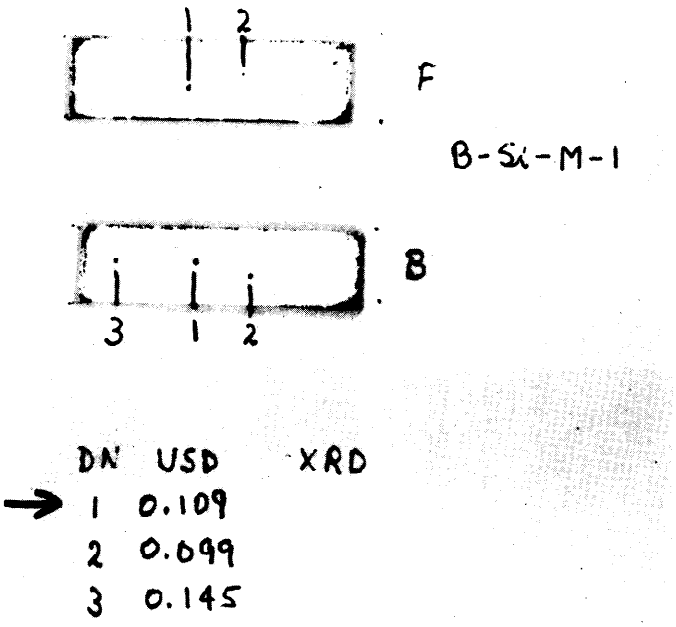

Figure A-3A C-scan of specimen B-Si-M-1

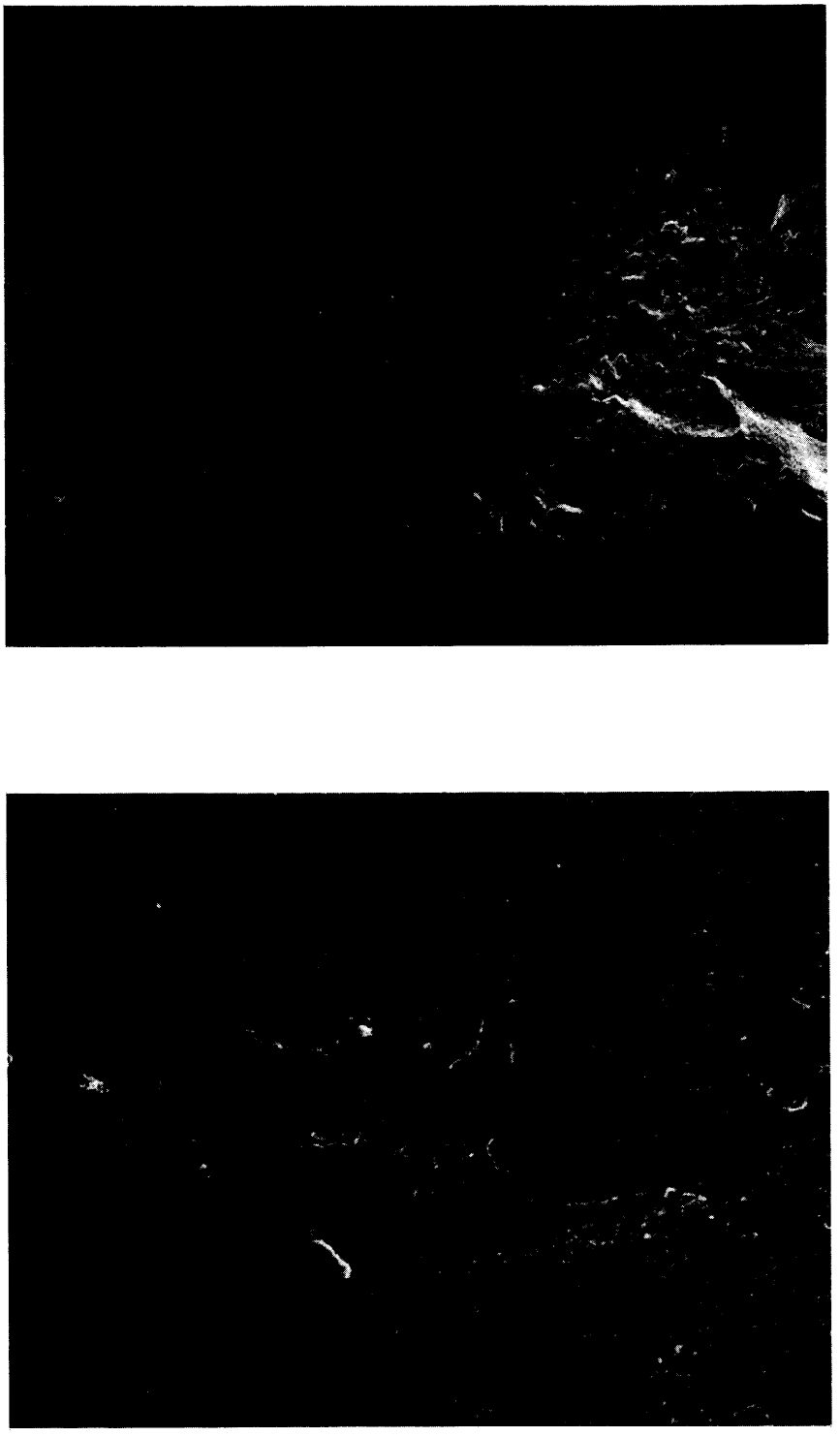

Figure A-3B. Fracture origin (silicon inclusion) in specimen B-Si-M-1 at 50X (above) and 200X (below).

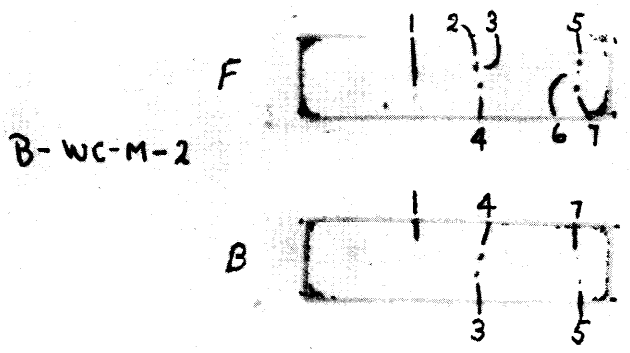

DN	USD	XRD
1	0.099	
2	0.109	
3	0.109	
→ 4	0.109	0.105 H
5	0.109	
6	0.109	
7	0.109	

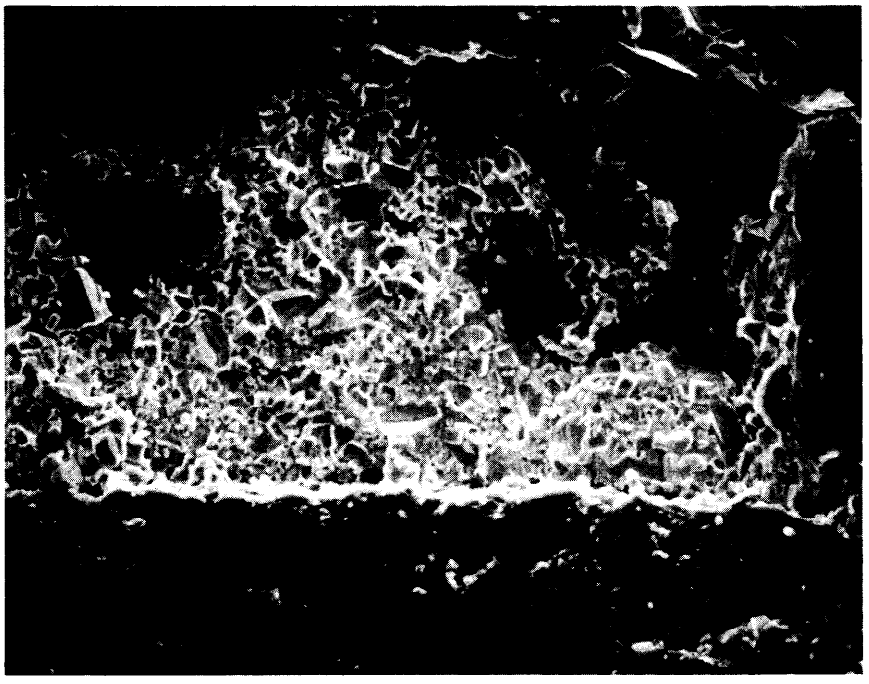

Figure A-4. C-scan (above) and fracture origin of WC inclusion (below) of 1000X of Specimen B-WC-M-2

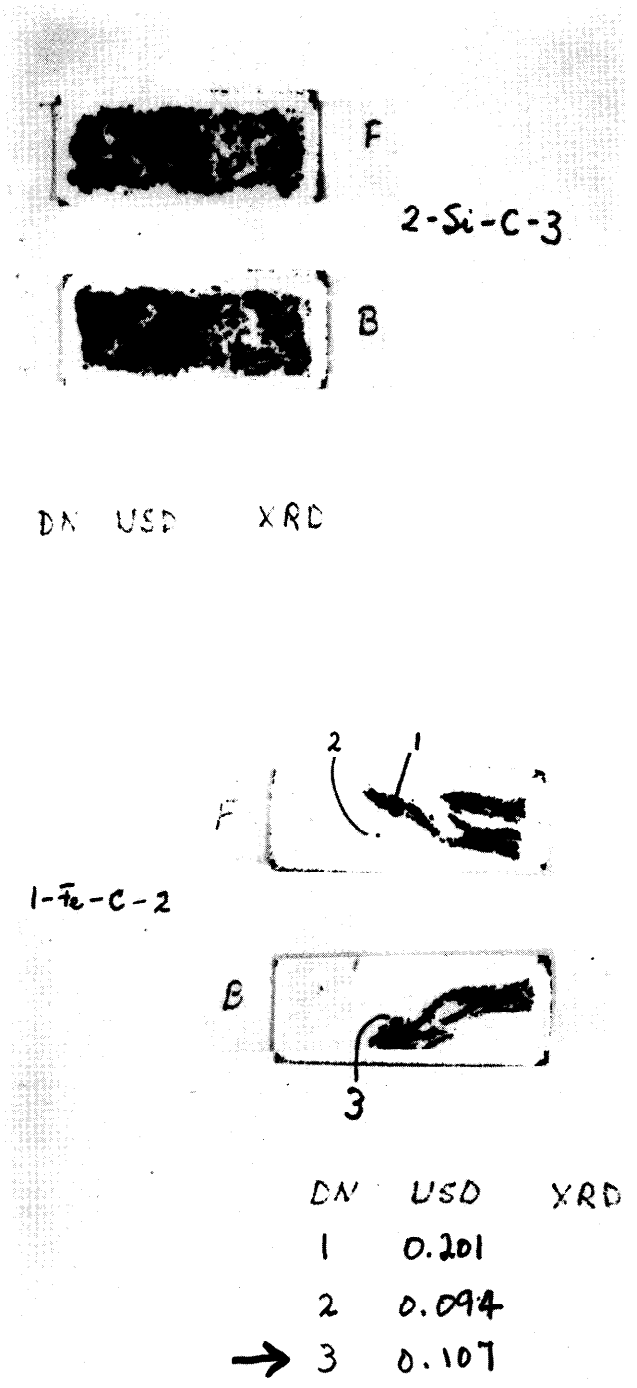

Figure A-5. C-scan of specimens 2-Si-C-3 and 1-Fe-C-2. Former shows extreme example of wide area ultrasonic reflections. Fracture origin of latter shown in Figure 28.

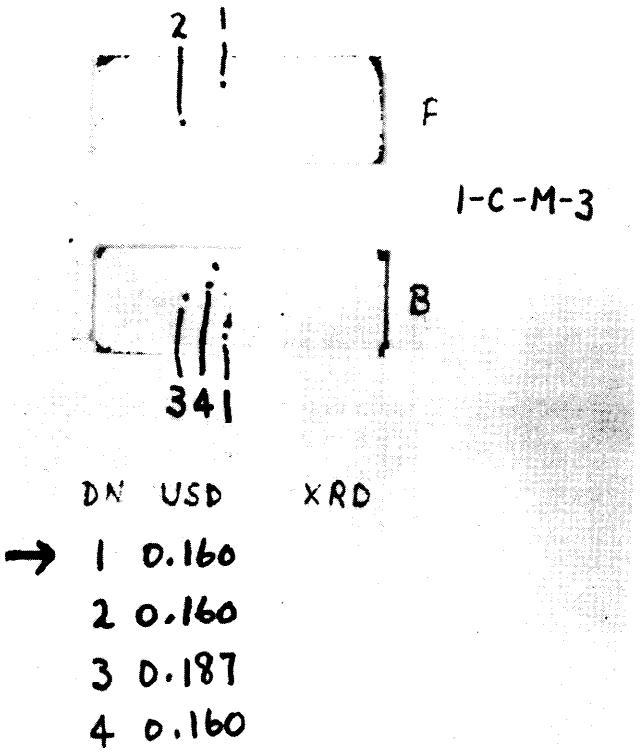

Figure A-6A. C-scan of specimen 1-C-M-3.

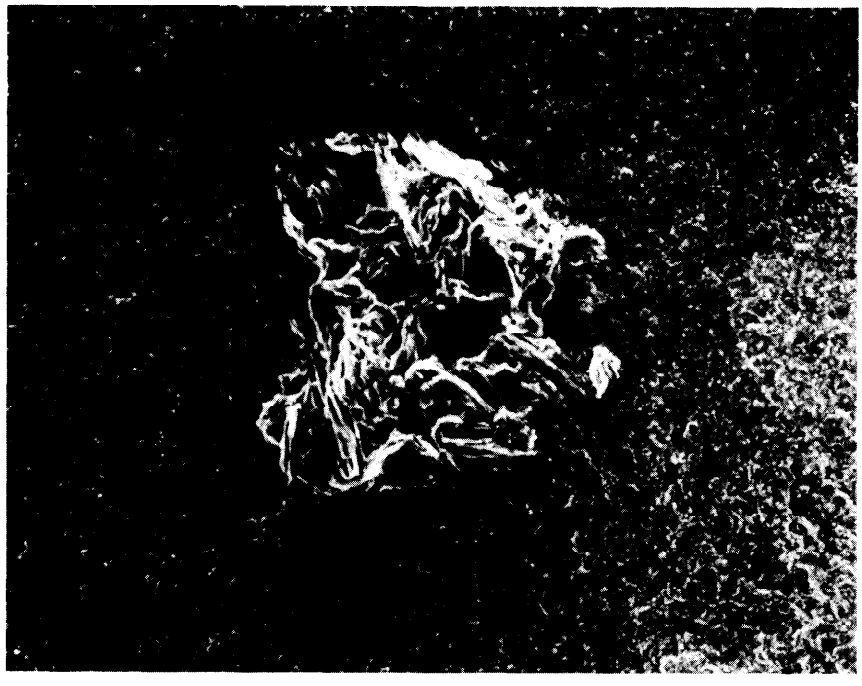

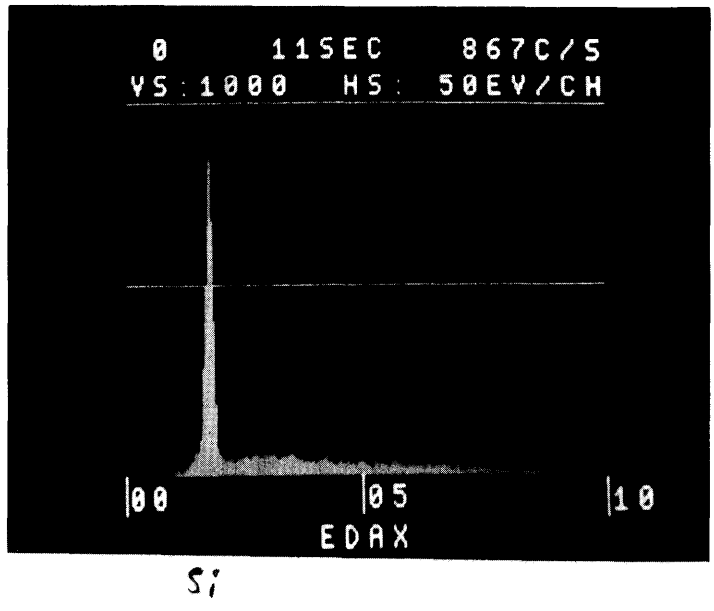

Figure A-6B. Fracture origin (carbon inclusion) in specimen 1-C-M-3 at 200X (above) and microprobe display of inclusion (below).

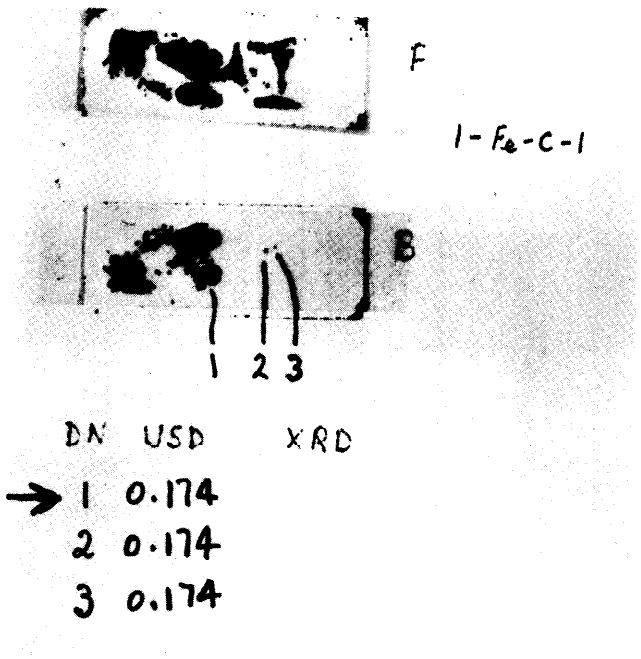

Figure A-7A. C-scan of specimen 1-Fe-C-1

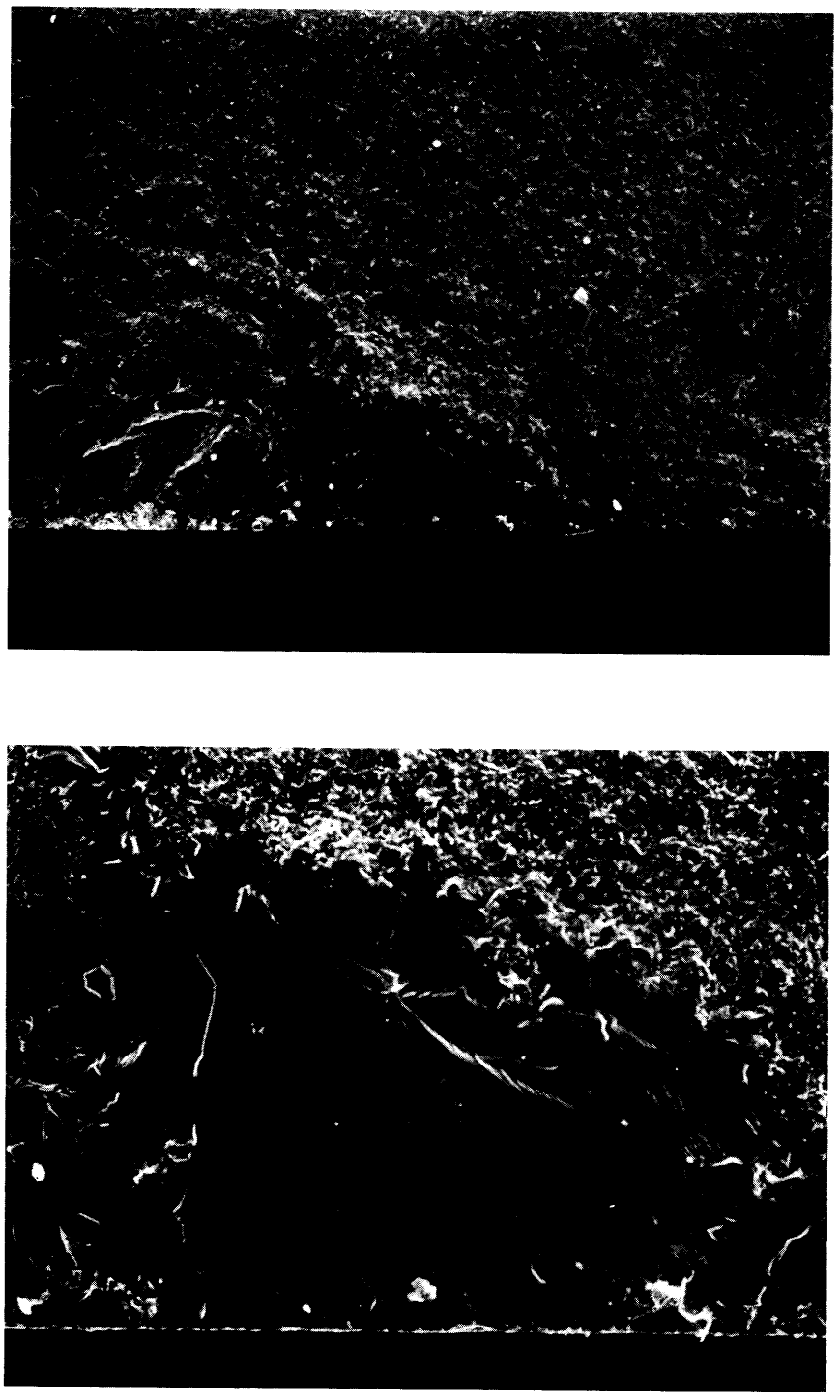

Figure A-7B. Fracture origin (silicon inclusion) in specimen 1-Fe-C-1 at 50X (above) and 200X (below).

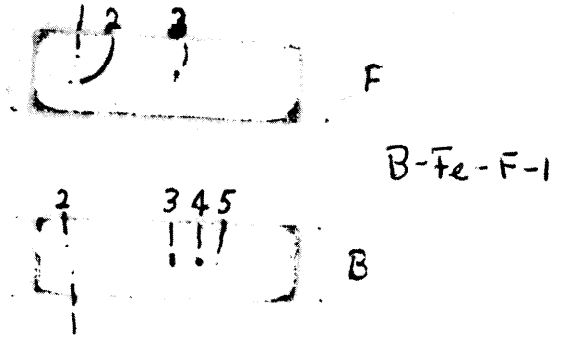

	DA	USD	XRD
	1	0.109	
	2	0.109	
→	3	0.109	0.105 H
	4	0.118	
	5	0.109	

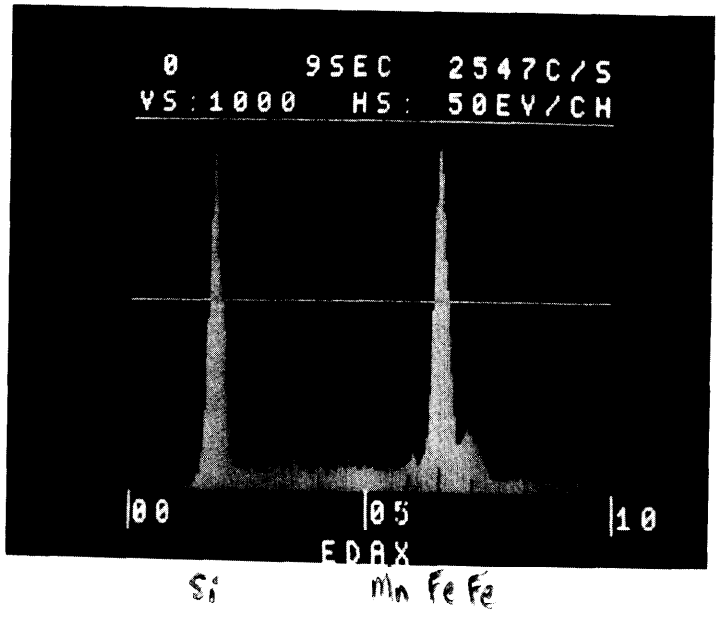

Figure A-8A. C-scan (above) and microprobe display (below) of specimen B-Fe-F-1

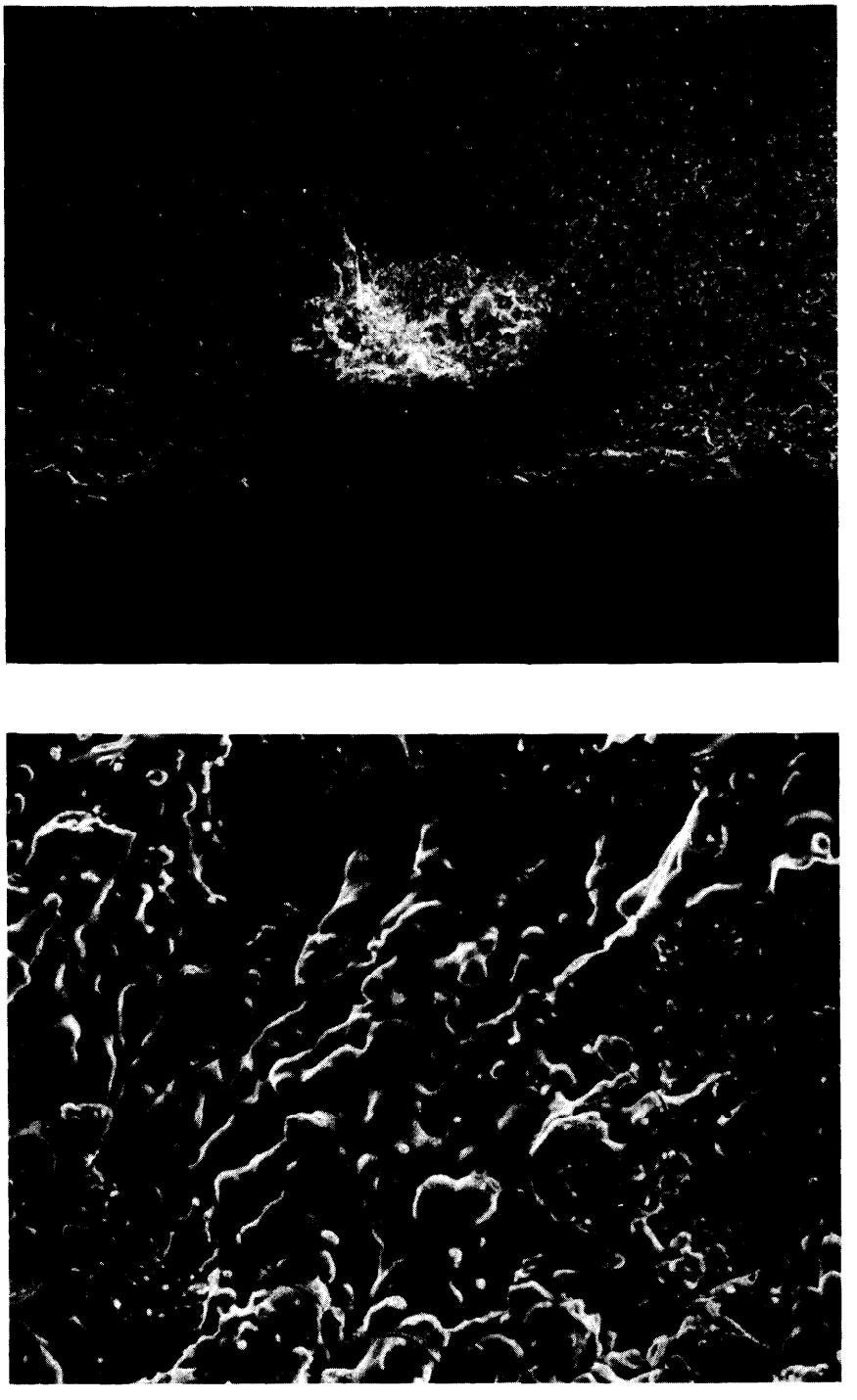

Figure A-8B. Fracture origin (iron inclusion) in specimen B-Fe-F-1 at 50X (above) and 1000X (below). Test temperature was 1093°C.

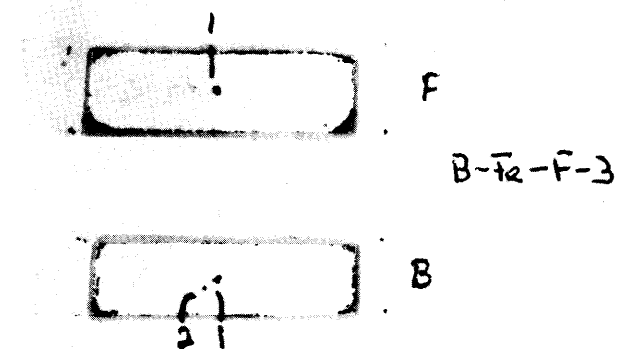

	DN	USD	XRD
→	1	0.109	0.110 H
	2	0.109	

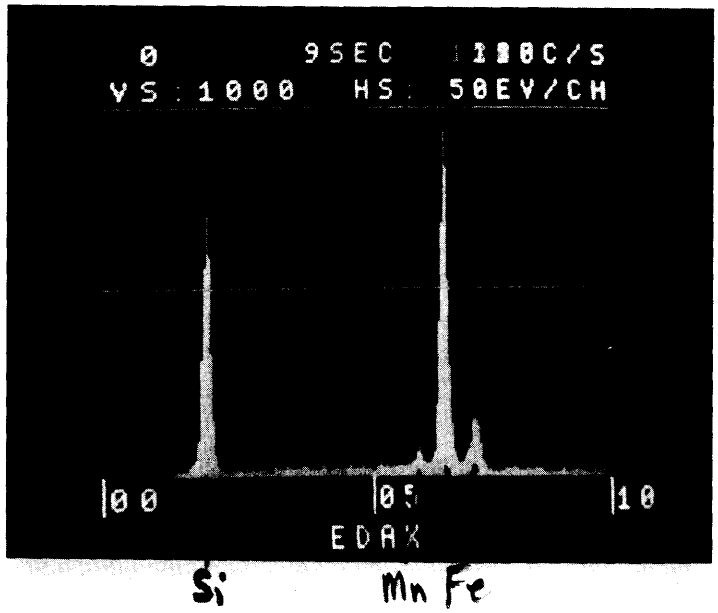

Figure A-9A. C-scan (above) and microprobe display (below) of specimen B-Fe-F-3.

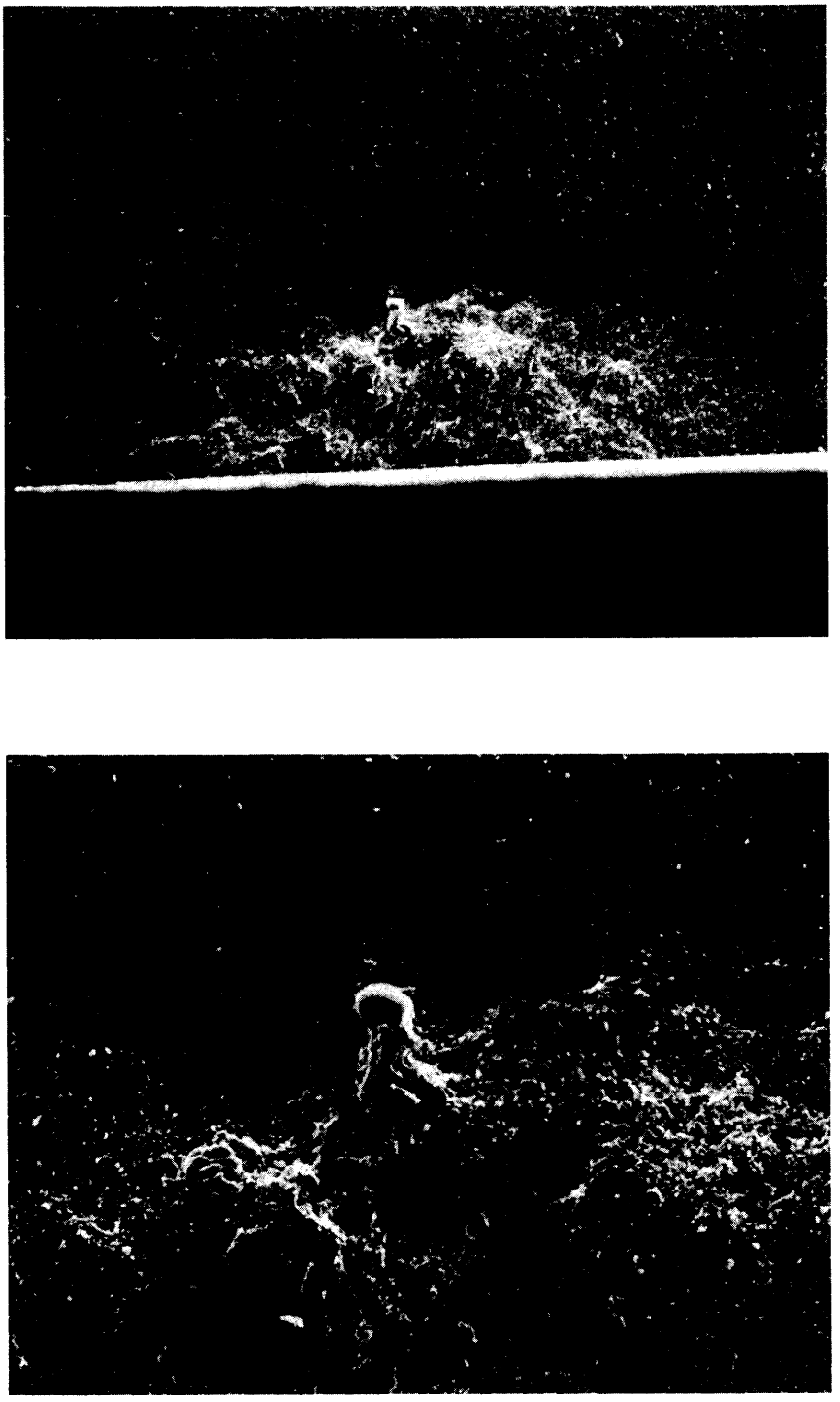

Figure A-9B. Fracture origin (iron inclusion) in specimen B-Fe-F-3 at 50X (above) and 200X (below). Note presence of slow crack growth and liquid formation.

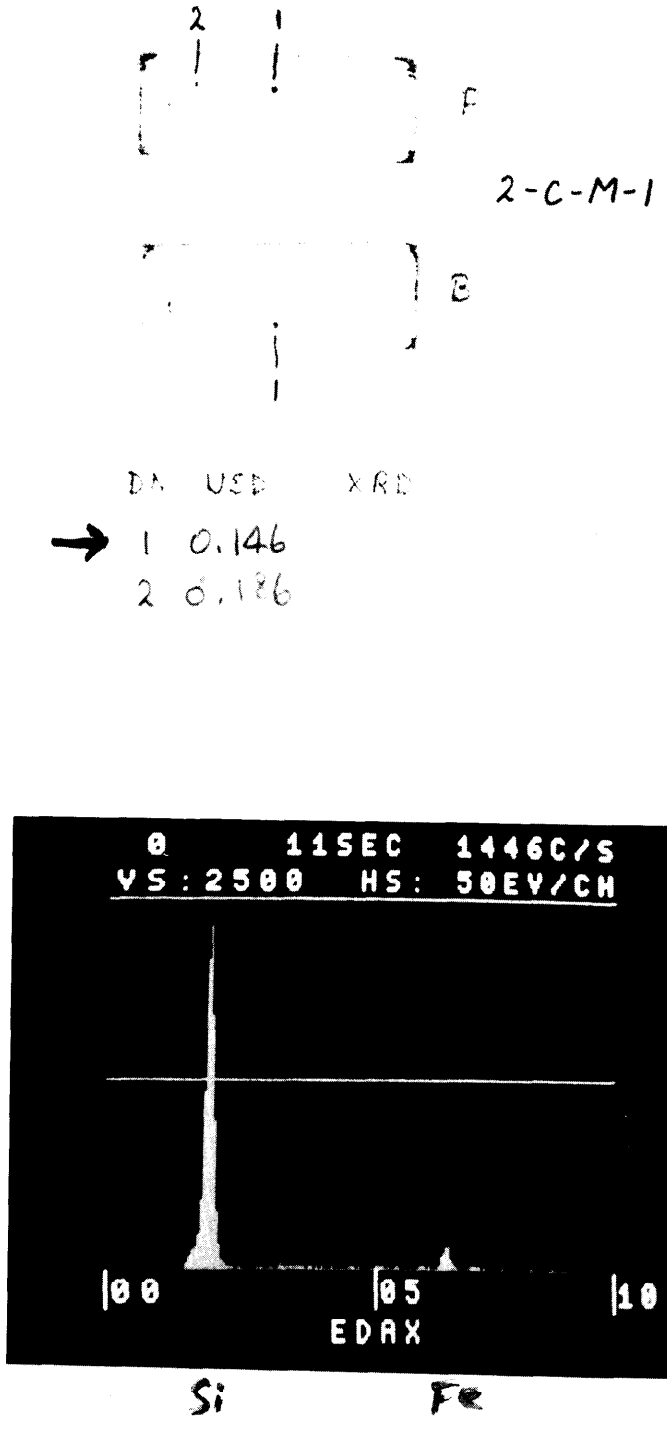

Figure A-10A. C-scan (above) and microprobe display (below) of specimen 2-C-M-1.

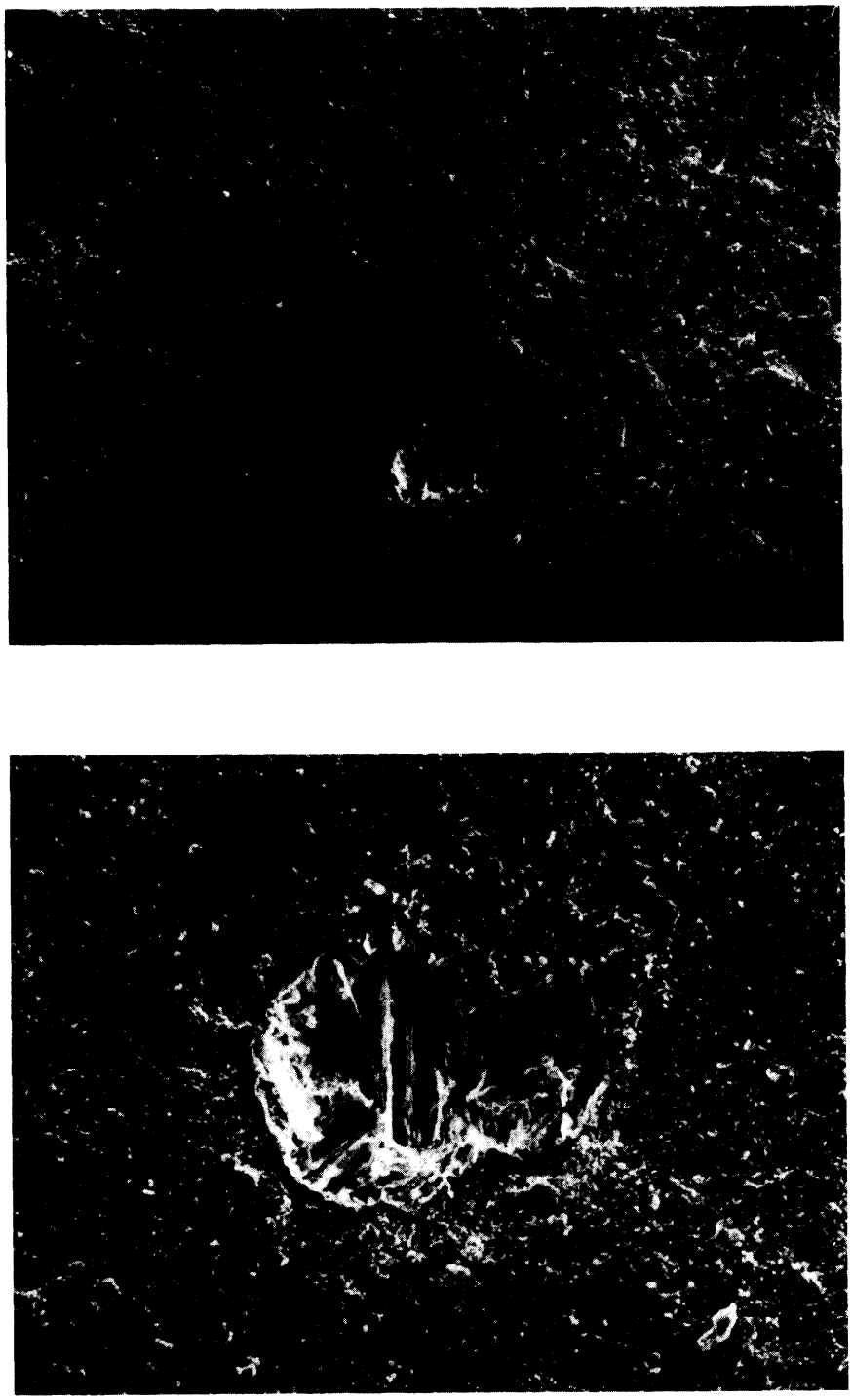

Figure A-10B Fracture origin (carbon inclusion) of specimen 2-C-M-1 at 50X (above) and 200 X (below). Test temperature was 1371°C.

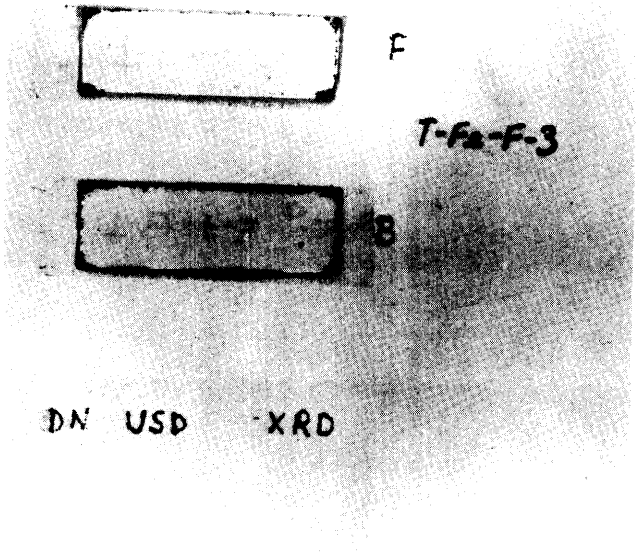

Figure A-11A. C-scan of specimen T-Fe-F-3. No defects detected.

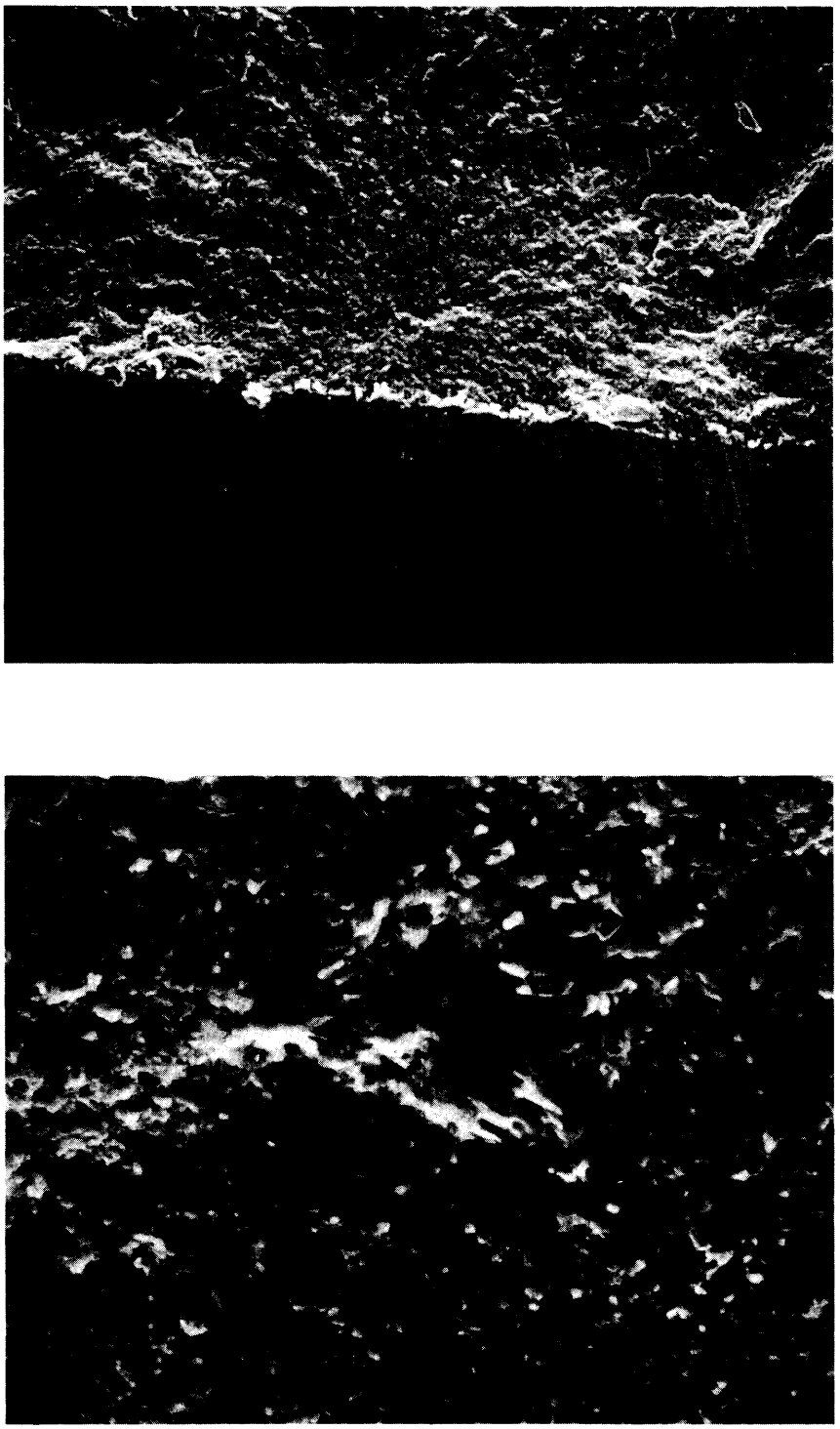

Figure A-11B. Fracture origin in specimen T-Fe-F-3 at 200X (above) and 2000X (below) of small iron inclusion.

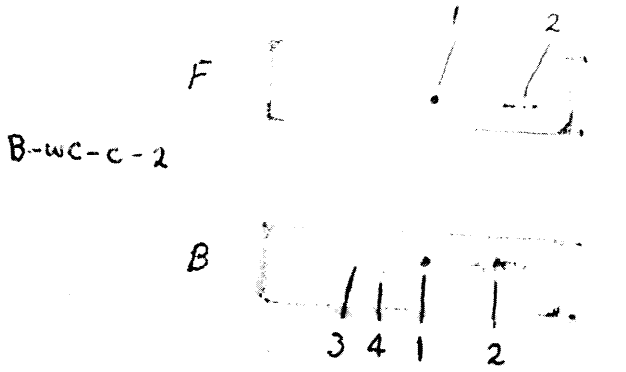

	DN	USD	XRD
→	1	0.111	0.095 H
	2	0.111	
	3	0.111	
	4	0.138	

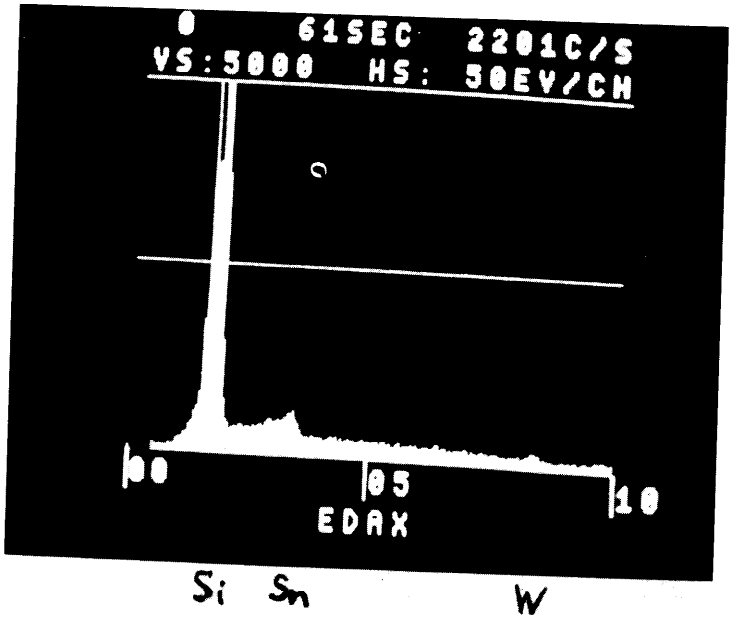

Figure A-12A. C-scan (above) and microprobe display (below) of specimen B-WC-C-2.

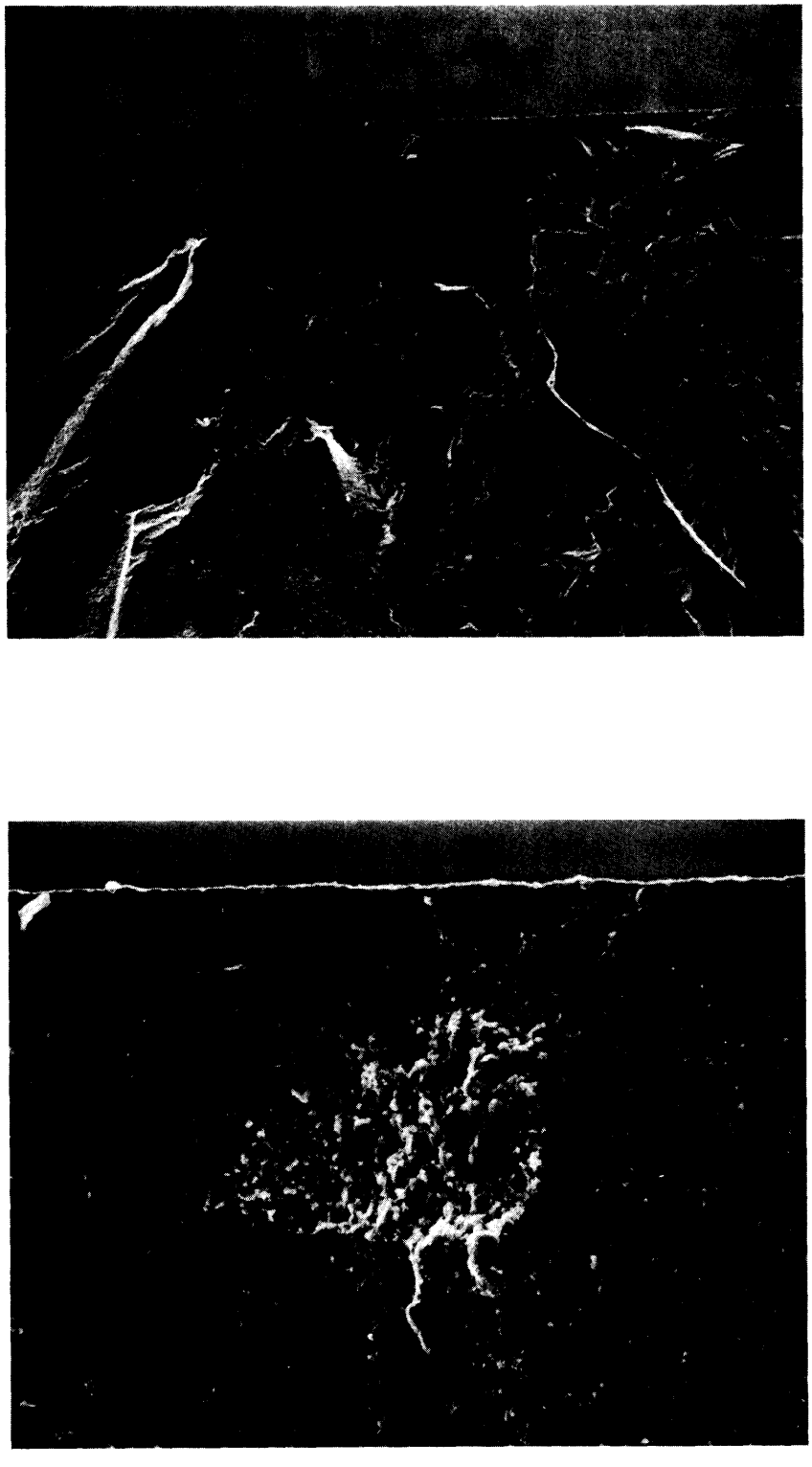

Figure A-12B. Fracture origin of specimen B-WC-C-2 at 50X (above) and 500X (below). Inclusion is of porous, unintentional type.

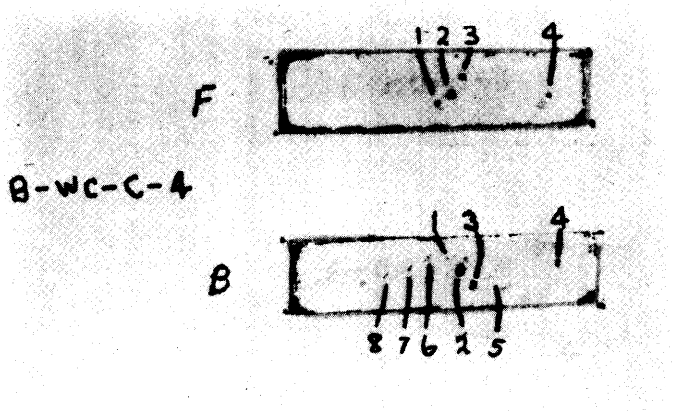

	DN	USD	XRD
	1	0.065	
→	2	0.111	0.090 H
	3	0.111	
	4	0.111	
	5	0.148	
	6	0.111	
	7	0.111	
	8	0.148	

Figure A-13A. C-scan of specimen B-WC-C-4

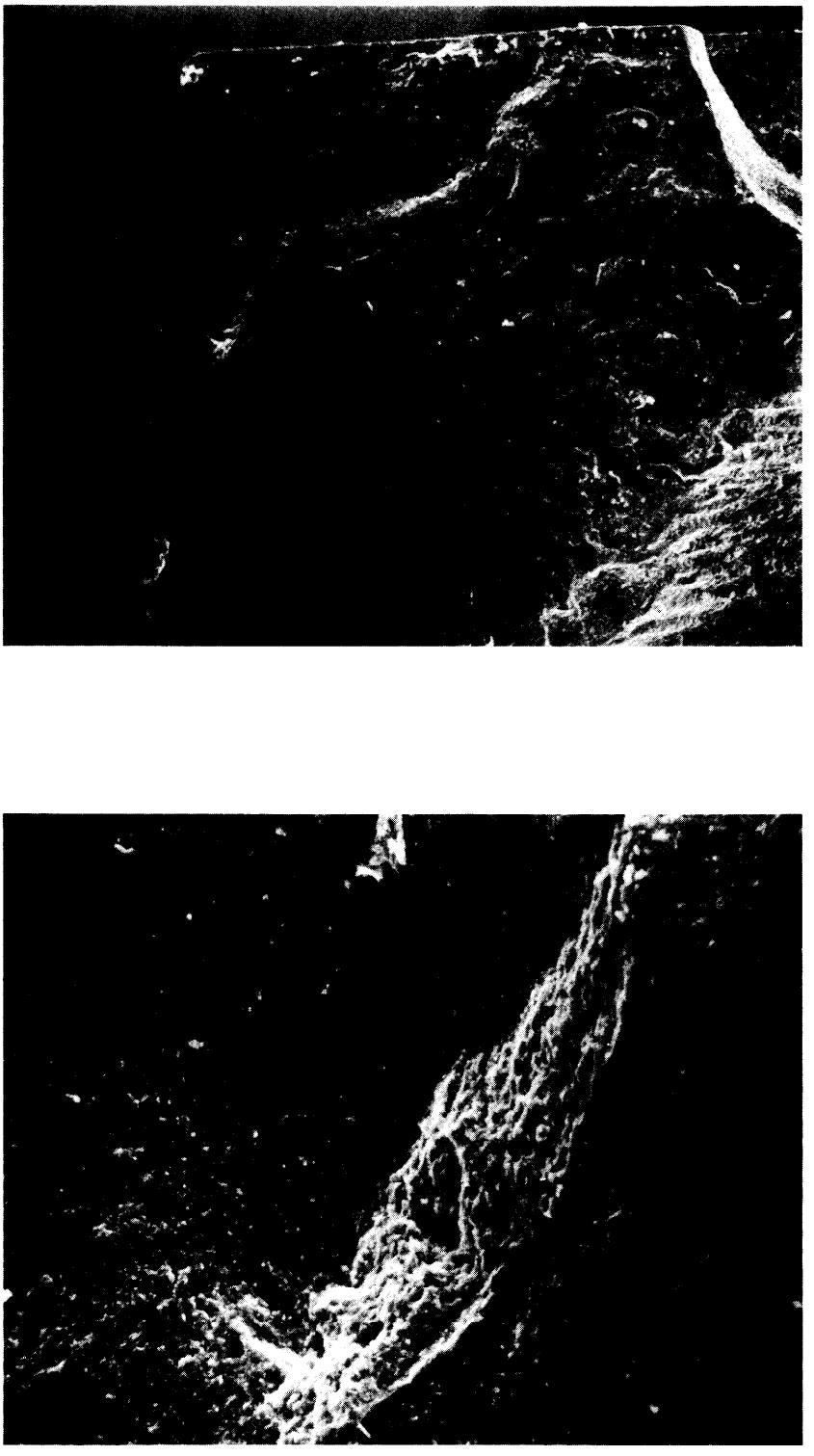

Figure A-13B. Fracture origin of specimen B-WC-C-4 at 100X (above) and 500X (below).

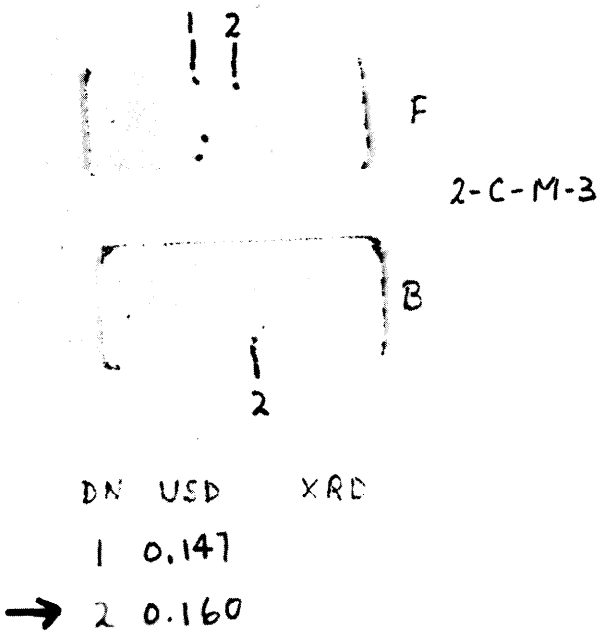

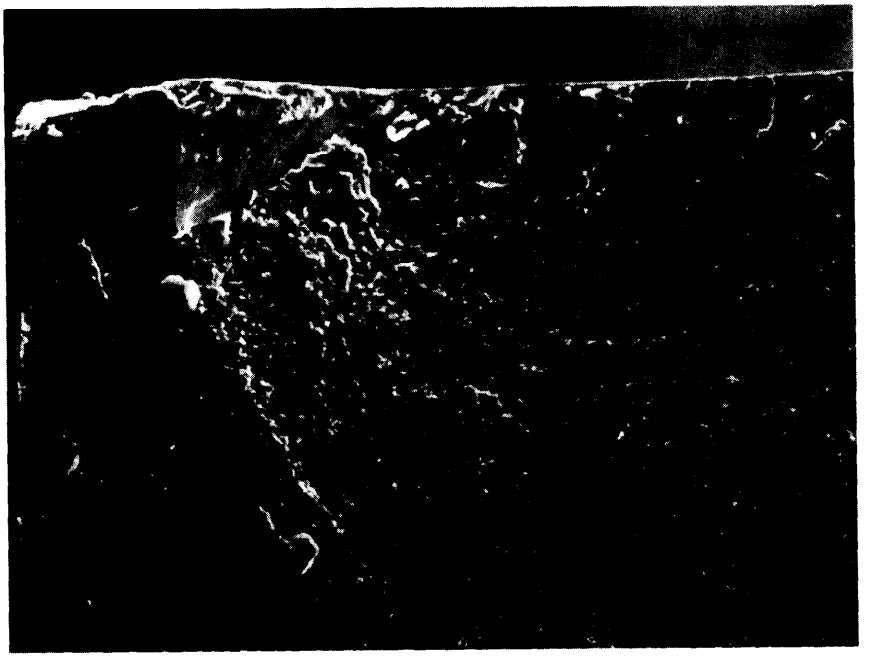

Figure A-14. C-scan and fracture origin (200X) of specimen 2-C-M-3.

Army Materials and Mechanics Research Center,
Watertown, Massachusetts 02172
DEVELOPMENT OF NONDESTRUCTIVE TESTING TECHNIQUES
FOR HIGH PERFORMANCE CERAMICS
H. R. Baumgartner and P. M. Hanson, Norton Company
Worcester, MA 01606 and R. H. Brockelman, AMMRC,
Watertown, MA 02172

Technical Report AMMRC TR 78-11, January 1978, 98 pp -
illus - tables, Contract DAAG46-76-C-0022
D/A Project M756350, AMCMS Code 53970M6350
Final Report, October 20, 1975 - October 20, 1977

AD_____

UNCLASSIFIED
UNLIMITED DISTRIBUTION

Key Words

Silicon nitride
Silicon carbide
Nondestructive testing
Mechanical strength
Inclusions
Ceramics

Two ceramic materials, a hot-pressed silicon nitride and a siliconized silicon carbide were manufactured with seeded particulates to evaluate the effectiveness of existing nondestructive test practices for defect detection in ceramics and to evaluate the effect of inclusions upon material strength. The types of seeded defects were of greater and lower density relative to the matrix materials and ranged in size from approximately 0.1 mm to 0.6 mm. The nondestructive methods used in the investigation were ultrasonics, radiography, eddy current and penetrant. Bend bar specimens were cut from the seeded regions of the billets and tested at 25°C, 1093°C and 1371°C. Fracture origins were examined by optical and electron microscopy and by microprobe to correlate the nature of the fracture initiating defects with the nondestructively detected defects. This permitted a ranking of defect detection sensitivity and defect effect upon strength.

Army Materials and Mechanics Research Center,
Watertown, Massachusetts 02172
DEVELOPMENT OF NONDESTRUCTIVE TESTING TECHNIQUES
FOR HIGH PERFORMANCE CERAMICS
H. R. Baumgartner and P. M. Hanson, Norton Company
Worcester, MA 01606 and R. H. Brockelman, AMMRC,
Watertown, MA 02172

Technical Report AMMRC TR 78-11, January 1978, 98 pp -
illus - tables, Contract DAAG46-76-C-0022
D/A Project M756350, AMCMS Code 53970M6350
Final Report, October 20, 1975 - October 20, 1977

AD_____

UNCLASSIFIED
UNLIMITED DISTRIBUTION

Key Words

Silicon nitride
Silicon carbide
Nondestructive testing
Mechanical strength
Inclusions
Ceramics

Two ceramic materials, a hot-pressed silicon nitride and a siliconized silicon carbide were manufactured with seeded particulates to evaluate the effectiveness of existing nondestructive test practices for defect detection in ceramics and to evaluate the effect of inclusions upon material strength. The types of seeded defects were of greater and lower density relative to the matrix materials and ranged in size from approximately 0.1 mm to 0.6 mm. The nondestructive methods used in the investigation were ultrasonics, radiography, eddy current and penetrant. Bend bar specimens were cut from the seeded regions of the billets and tested at 25°C, 1093°C and 1371°C. Fracture origins were examined by optical and electron microscopy and by microprobe to correlate the nature of the fracture initiating defects with the nondestructively detected defects. This permitted a ranking of defect detection sensitivity and defect effect upon strength.

Army Materials and Mechanics Research Center,
Watertown, Massachusetts 02172
DEVELOPMENT OF NONDESTRUCTIVE TESTING TECHNIQUES
FOR HIGH PERFORMANCE CERAMICS
H. R. Baumgartner and P. M. Hanson, Norton Company
Worcester, MA 01606 and R. H. Brockelman, AMMRC,
Watertown, MA 02172

Technical Report AMMRC TR 78-11, January 1978, 98 pp -
illus - tables, Contract DAAG46-76-C-0022
D/A Project M756350, AMCMS Code 53970M6350
Final Report, October 20, 1975 - October 20, 1977

AD_____

UNCLASSIFIED
UNLIMITED DISTRIBUTION

Key Words

Silicon nitride
Silicon carbide
Nondestructive testing
Mechanical strength
Inclusions
Ceramics

Two ceramic materials, a hot-pressed silicon nitride and a siliconized silicon carbide were manufactured with seeded particulates to evaluate the effectiveness of existing nondestructive test practices for defect detection in ceramics and to evaluate the effect of inclusions upon material strength. The types of seeded defects were of greater and lower density relative to the matrix materials and ranged in size from approximately 0.1 mm to 0.6 mm. The nondestructive methods used in the investigation were ultrasonics, radiography, eddy current and penetrant. Bend bar specimens were cut from the seeded regions of the billets and tested at 25°C, 1093°C and 1371°C. Fracture origins were examined by optical and electron microscopy and by microprobe to correlate the nature of the fracture initiating defects with the nondestructively detected defects. This permitted a ranking of defect detection sensitivity and defect effect upon strength.

Army Materials and Mechanics Research Center,
Watertown, Massachusetts 02172
DEVELOPMENT OF NONDESTRUCTIVE TESTING TECHNIQUES
FOR HIGH PERFORMANCE CERAMICS
H. R. Baumgartner and P. M. Hanson, Norton Company
Worcester, MA 01606 and R. H. Brockelman, AMMRC,
Watertown, MA 02172

Technical Report AMMRC TR 78-11, January 1978, 98 pp -
illus - tables, Contract DAAG46-76-C-0022
D/A Project M756350, AMCMS Code 53970M6350
Final Report, October 20, 1975 - October 20, 1977

AD_____

UNCLASSIFIED
UNLIMITED DISTRIBUTION

Key Words

Silicon nitride
Silicon carbide
Nondestructive testing
Mechanical strength
Inclusions
Ceramics

Two ceramic materials, a hot-pressed silicon nitride and a siliconized silicon carbide were manufactured with seeded particulates to evaluate the effectiveness of existing nondestructive test practices for defect detection in ceramics and to evaluate the effect of inclusions upon material strength. The types of seeded defects were of greater and lower density relative to the matrix materials and ranged in size from approximately 0.1 mm to 0.6 mm. The nondestructive methods used in the investigation were ultrasonics, radiography, eddy current and penetrant. Bend bar specimens were cut from the seeded regions of the billets and tested at 25°C, 1093°C and 1371°C. Fracture origins were examined by optical and electron microscopy and by microprobe to correlate the nature of the fracture initiating defects with the nondestructively detected defects. This permitted a ranking of defect detection sensitivity and defect effect upon strength.

Army Materials and Mechanics Research Center,
Watertown, Massachusetts 02172
DEVELOPMENT OF NONDESTRUCTIVE TESTING TECHNIQUES FOR HIGH PERFORMANCE CERAMICS
H. R. Baumgartner and P. M. Hanson, Norton Company
Worcester, MA 01606 and R. H. Brockelman, AMMRC,
Watertown, MA 02172

Technical Report AMMRC TR 78-11, January 1978, 98 pp -
illus - tables, Contract DAAG46-76-C-0022
D/A Project M756350, AMCMS Code 53970M6350
Final Report, October 20, 1975 - October 20, 1977

AD_____

UNCLASSIFIED
UNLIMITED DISTRIBUTION

Key Words

Silicon nitride
Silicon carbide
Nondestructive testing
Mechanical strength
Inclusions
Ceramics

Two ceramic materials, a hot-pressed silicon nitride and a siliconized silicon carbide were manufactured with seeded particulates to evaluate the effectiveness of existing nondestructive test practices for defect detection in ceramics and to evaluate the effect of inclusions upon material strength. The types of seeded defects were of greater and lower density relative to the matrix materials and ranged in size from approximately 0.1 mm to 0.6 mm. The nondestructive methods used in the investigation were ultrasonics, radiography, eddy current and penetrant. Bend bar specimens were cut from the seeded regions of the billets and tested at 25°C, 1093°C and 1371°C. Fracture origins were examined by optical and electron microscopy and by microprobe to correlate the nature of the fracture initiating defects with the nondestructively detected defects. This permitted a ranking of defect detection sensitivity and defect effect upon strength.

Army Materials and Mechanics Research Center,
Watertown, Massachusetts 02172
DEVELOPMENT OF NONDESTRUCTIVE TESTING TECHNIQUES FOR HIGH PERFORMANCE CERAMICS
H. R. Baumgartner and P. M. Hanson, Norton Company
Worcester, MA 01606 and R. H. Brockelman, AMMRC,
Watertown, MA 02172

Technical Report AMMRC TR 78-11, January 1978, 98 pp -
illus - tables, Contract DAAG46-76-C-0022
D/A Project M756350, AMCMS Code 53970M6350
Final Report, October 20, 1975 - October 20, 1977

AD_____

UNCLASSIFIED
UNLIMITED DISTRIBUTION

Key Words

Silicon nitride
Silicon carbide
Nondestructive testing
Mechanical strength
Inclusions
Ceramics

Two ceramic materials, a hot-pressed silicon nitride and a siliconized silicon carbide were manufactured with seeded particulates to evaluate the effectiveness of existing nondestructive test practices for defect detection in ceramics and to evaluate the effect of inclusions upon material strength. The types of seeded defects were of greater and lower density relative to the matrix materials and ranged in size from approximately 0.1 mm to 0.6 mm. The nondestructive methods used in the investigation were ultrasonics, radiography, eddy current and penetrant. Bend bar specimens were cut from the seeded regions of the billets and tested at 25°C, 1093°C and 1371°C. Fracture origins were examined by optical and electron microscopy and by microprobe to correlate the nature of the fracture initiating defects with the nondestructively detected defects. This permitted a ranking of defect detection sensitivity and defect effect upon strength.

Army Materials and Mechanics Research Center,
Watertown, Massachusetts 02172
DEVELOPMENT OF NONDESTRUCTIVE TESTING TECHNIQUES FOR HIGH PERFORMANCE CERAMICS
H. R. Baumgartner and P. M. Hanson, Norton Company
Worcester, MA 01606 and R. H. Brockelman, AMMRC,
Watertown, MA 02172

Technical Report AMMRC TR 78-11, January 1978, 98 pp -
illus - tables, Contract DAAG46-76-C-0022
D/A Project M756350, AMCMS Code 53970M6350
Final Report, October 20, 1975 - October 20, 1977

AD_____

UNCLASSIFIED
UNLIMITED DISTRIBUTION

Key Words

Silicon nitride
Silicon carbide
Nondestructive testing
Mechanical strength
Inclusions
Ceramics

Two ceramic materials, a hot-pressed silicon nitride and a siliconized silicon carbide were manufactured with seeded particulates to evaluate the effectiveness of existing nondestructive test practices for defect detection in ceramics and to evaluate the effect of inclusions upon material strength. The types of seeded defects were of greater and lower density relative to the matrix materials and ranged in size from approximately 0.1 mm to 0.6 mm. The nondestructive methods used in the investigation were ultrasonics, radiography, eddy current and penetrant. Bend bar specimens were cut from the seeded regions of the billets and tested at 25°C, 1093°C and 1371°C. Fracture origins were examined by optical and electron microscopy and by microprobe to correlate the nature of the fracture initiating defects with the nondestructively detected defects. This permitted a ranking of defect detection sensitivity and defect effect upon strength.

Army Materials and Mechanics Research Center,
Watertown, Massachusetts 02172
DEVELOPMENT OF NONDESTRUCTIVE TESTING TECHNIQUES FOR HIGH PERFORMANCE CERAMICS
H. R. Baumgartner and P. M. Hanson, Norton Company
Worcester, MA 01606 and R. H. Brockelman, AMMRC,
Watertown, MA 02172

Technical Report AMMRC TR 78-11, January 1978, 98 pp -
illus - tables, Contract DAAG46-76-C-0022
D/A Project M756350, AMCMS Code 53970M6350
Final Report, October 20, 1975 - October 20, 1977

AD_____

UNCLASSIFIED
UNLIMITED DISTRIBUTION

Key Words

Silicon nitride
Silicon carbide
Nondestructive testing
Mechanical strength
Inclusions
Ceramics

Two ceramic materials, a hot-pressed silicon nitride and a siliconized silicon carbide were manufactured with seeded particulates to evaluate the effectiveness of existing nondestructive test practices for defect detection in ceramics and to evaluate the effect of inclusions upon material strength. The types of seeded defects were of greater and lower density relative to the matrix materials and ranged in size from approximately 0.1 mm to 0.6 mm. The nondestructive methods used in the investigation were ultrasonics, radiography, eddy current and penetrant. Bend bar specimens were cut from the seeded regions of the billets and tested at 25°C, 1093°C and 1371°C. Fracture origins were examined by optical and electron microscopy and by microprobe to correlate the nature of the fracture initiating defects with the nondestructively detected defects. This permitted a ranking of defect detection sensitivity and defect effect upon strength.

DISTRIBUTION LIST

No. of Copies	To
	Metals and Ceramics Information Center, 505 King Avenue, Columbus, Ohio 43201
1	ATTN: Mr. Harold Mindlin, Director
1	Mr. James Lynch, Assistant Director
12	Commander, Defense Documentation Center, Cameron Station, Building 5, 5010 Duke Street, Alexandria, Virginia 22314
	Office of the Deputy Chief of Staff for Research, Development, and Acquisition, Washington, D.C. 20310
1	ATTN: DAMA-ARZ-E
1	DAMA-CSS
	Commander, Army Research Office, P.O. Box 12211, Research Triangle Park, North Carolina 27709
1	ATTN: Dr. George Mayer
1	Mr. J. J. Murray
	Commander, U.S. Army Materiel Development and Readiness Command, 5001 Eisenhower Avenue, Alexandria, Virginia 22333
1	ATTN: DRCQA-E
1	DRCQA-P
1	DRCDE-D
1	DRCDMD-FT
1	DRCLDC
1	DRCMT
1	DRCMM-M
	Commander, U.S. Army Missile Research and Development Command, Redstone Arsenal, Alabama 35809
2	ATTN: DRDMI-TB, Redstone Scientific Information Center
1	DRDMI-TK, Mr. J. Alley
1	DRDMI-M
1	DRDMI-ET, Mr. Robert O. Black
1	DRDMI-QS, Mr. George L. Stewart, Jr.
1	DRDMI-EAT, Mr. R. Talley
1	DRDMI-QP
	Commander, U.S. Army Troop Support and Aviation Materiel Readiness Command, 4300 Goodfellow Boulevard, St. Louis, Missouri 63120
1	ATTN: DRSTS-PLE, Mr. J. Corwin
1	DRSTS-Q
1	DRSTS-M

No. of Copies	To
	Commander, U.S. Army Mobility Equipment Research and Development Command, Fort Belvoir, Virginia 22060
1	ATTN: DRDME-D
1	DRDME-E
1	DRDME-G
1	DRDME-H
1	DRDME-M
1	DRDME-T
1	DRDME-TQ
1	DRDME-V
1	DRDME-ZE
1	DRDME-N
	Commander, U.S. Army Tank-Automotive Materiel Readiness Command, Warren, Michigan 48090
2	ATTN: DRSTA-Q
	Commander, U.S. Army Armament Research and Development Command, Dover, New Jersey 07801
1	ATTN: DRDAR-LC, Mr. E. Kelly
1	DRDAR-LCA, Dr. Sharkoff
1	DRDAR-LCE, Dr. Walker
5	DRDAR-QAS, Mr. F. Fitzsimmons
1	DRDAR-SCM, Mr. J. D. Corrie
1	DRDAR-TSP, Mr. B. Stephans
2	DRDAR-TSS, (STINFO)
	Commander, Watervliet Arsenal, Watervliet, New York 12189
1	ATTN: DRDAR-LCB, Mr. T. Moraczewski
	Commander, U.S. Army Aviation Research and Development Command, St. Louis, Missouri 63166
1	ATTN: DRDAV-EXT
1	DRDAV-QR
1	DRDAV-QP
1	DRDAV-QE
	Commander, U.S. Army Tank-Automotive Research and Development Command, Warren, Michigan 48090
1	ATTN: DRDTA-RKA, Mr. D. Matichuk
1	DRDTA-RKA, Mr. R. Dunec
1	DRDTA-JA, Mr. C. Kedzior
1	DRDTA-UL, Tech Library
	Director, U.S. Army Industrial Base Engineering Activity, Rock Island, Illinois 61201
1	ATTN: DRXIB-MT, Dr. W. T. Yang

No. of Copies	To
	Commander, Harry Diamond Laboratories, 2800 Powder Mill Road, Adelphi, Maryland 20783
1	ATTN: DRXDO-EDE, Mr. B. F. Willis
	Commander, Aberdeen Proving Ground, Maryland 21005
1	ATTN: STEAP-MT
1	STEAP-TL
1	STEAP-MT-M, Mr. J. A. Feroli
1	STEAP-MT-G, Mr. R. L. Huddleston
	Naval Research Laboratory, Washington, D.C. 20375
1	ATTN: Dr. J. M. Krafft, Code 8430
1	Library, Code 2620
	Air Force Materials Laboratory, Wright-Patterson Air Force Base, Ohio 45433
1	ATTN: AFML-DO, Library
1	AFML-LTM, Mr. E. Wheeler
1	AFML-LLP, Mr. R. Rowand
1	R. W. McClung, Metals and Ceramics Division, Oak Ridge National Laboratory, P.O. Box X, Oak Ridge, Tennessee 37803
	Hughes Aircraft Company, Electron Dynamics Division, 3100 West Lomita Blvd., Torrance, California 90509
1	ATTN: Dr. Charles A. Escoffery
1	Chief, Materials Engineering Department, Dept. 93-03M, AiResearch Manufacturing Company of Arizona, 402 South 36th Street, P.O. Box 5217, Phoenix, Arizona 85010
	Director, Army Materials and Mechanics Research Center, Watertown, Massachusetts 02172
2	ATTN: DRXMR-PL
1	DRXMR-P
2	DRXMR-M
1	DRXMR-MQ
1	DRXMR-MI, Mr. Darcy
1	DRXMR-L, Dr. Chait
1	DRXMR-AP
8	DRXMR-MI, Mr. Hastings